Diss. ETH No. 16058

Absolute Positions of Solar X-ray and Gamma-ray Sources

A dissertation submitted to the
SWISS FEDERAL INSTITUTE OF TECHNOLOGY
ZÜRICH

for the degree of
Doctor of Natural Sciences

presented by

MARTIN D. FIVIAN
Dipl. Phys. ETH Zürich

born August 16, 1963
citizen of Koeniz BE

accepted on the recommendation of
Prof. Dr. Arnold O. Benz, examiner
Dr. Alex Zehnder, co-examiner
Prof. Dr. Ralph Eichler, co-examiner

2005

the sun,
with all those planets
revolving around it and dependent on it,
can still ripen a bunch of grapes
as if it had nothing else
in the universe to do.

Galileo Galilei, 1564-1642

Contents

Abstract

Solar flares have first been discovered over 150 years ago and a rich and complex set of observations have been acquired since. A flare can be understood as a sudden brightening from white light to X-rays and Gamma-rays including phenoma of longer wavelength of up to 10 km. Within minutes, a huge amount of energy of up to 10^{33} ergs is released and electrons are accelerated to hundreds of MeV. Yet, it is unclear how this amount of energy, which is believed to be stored in the magnetic field of the solar corona, can be released within such a short period of time and why a significant fraction of this energy appears to result in accelerated particles. The Reuven Ramaty High Energy Solar Spectroscopic Imager (RHESSI) is imaging X-ray and Gamma-ray sources with an unprecedented spatial and energy resolution providing a new access to understand particle acceleration and explosive energy release.

Solar hard X-ray bremsstrahlung from energetic electrons accelerated in the impulsive phase of a flare is observed to be primarily from the footpoints of magnetic loops. Standard magnetic reconnection models predict increasing separation of the footpoints during the flare as longer and larger loops are produced. If the reconnection process results in accelerated electrons, the hard X-ray footpoints should show this motion. The motion is only apparent; it is due to the hard X-ray emission shifting to footpoints of neighboring newly reconnected field lines. The velocity of footpoint separation reflects the rate of magnetic reconnection and should be roughly proportional to the energy deposition rate in the footpoints; and therefore, the separation of the footpoints should be roughly proportional to the total deposited energy for a given time interval.

Unlike for soft X-rays and longer wavelength emissions, focusing optics are not (yet) feasible at hard X-rays and Gamma-rays. For RHESSI, a Fourier-transform imaging technique has been implemented using nine bi-grid collimators combined with Germanium detectors mounted on a rotating spacecraft. In order to have a spatial resolution of 2.3 arc seconds (for the finest grid) and to precisely correlate with observations at other wavelengths, two precise aspect systems are implemented; the Solar Aspect System (SAS) and the Roll Angle System (RAS).

The SAS yields sub-arc second knowledge of the radial pointing with respect to the sun center and the RAS provides precise knowledge on the roll angle of the rotating spacecraft. The combined SAS/RAS aspect system provides a knowledge of the absolute pointing with an accuracy of 1 arc second.

This thesis describes the design, calibration, and performance of the aspect system of RHESSI. The reconstruction of the aspect solution is presented and the measured positions of hard X-ray and gamma-ray sources are justified. For two X-class flares, the positions of the footpoints is measured as a function of time and is correlated with the total deposited energy. The implications of this correlation on the dimensional measures of the reconnection region is discussed.

Zusammenfassung

Sonnenflares wurden bereits vor 150 Jahren entdeckt und eine reiche Fülle von Beobachtungen von grosser Komplexität wurden seither gesammelt. Ein Flare kann heute verstanden werden als eine plötzliche Intensivierung von optischem Licht bis Röntgenstrahlung und Gammastrahlung, wobei auch Phänomene von grösseren Wellenlängen von bis zu 10 km zu beobachten sind. Eine riesige Menge von Energie von bis zu 10^{33} ergs wird innerhalb Minuten freigesetzt und Elektronen werden auf hunderte von MeV beschleunigt. Es ist bis heute unklar wie diese Menge von Energie, die vermutlich im magnetischen Feld gespeichert ist, innerhalb eines so kurzen Zeitraumes freigesetzt werden kann und warum ein signifikanter Teil dieser Energie in beschleunigte Teilchen umgewandelt wird. Der "Reuven Ramaty High Energy Solar Spectroscopic Imager" (RHESSI) bildet Röntgen- und Gammaquellen mit einer beispiellosen räumlichen und energetischen Auflösung ab. Dies ermöglicht einen neuen Zugang, um die Beschleunigung von Teilchen und die explosionsartige Freisetzung von Energie zu verstehen.

Solare Bremsstrahlung im Röntgenbereich, die durch beschleunigte Teilchen während der impulsiven Phase eines Flares erzeugt wird, wird hauptsächlich in den Fusspunkten von magnetischen Loops (Bögen) beobachtet. Standard Modelle von magnetischer Reconnection (eine Umkonfigurierung der magnetischen Feldlinien) sagen eine zunehmende Distanz zwischen den Fusspunkten voraus. Falls dieser Prozess der magnetischen Reconnection Teilchen beschleunigt, dann sollte eine Bewegung der Fusspunkte im Röngtenbereich beobachtet werden können. Diese Bewegung ist aber nur scheinbar. Sie rührt daher, dass sich die Röntgenemission zu benachbarten, neu verbundenen Feldlinien verschiebt. Die Geschwindigkeit der zunehmenden Distanz der Fusspunkte spiegelt die Rate der magnetischen Reconnection wider und sollte daher mehr oder weniger proportional zur Energierate sein, welche in den Fusspunkten deponiert wird. Die Distanz zwischen den Fusspunkten sollte daher eine Proportionalität zur totalen Energie zeigen, welche während eines gegebenen Zeitintervals deponiert wird.

Im Gegensatz zur weichen Röntgenstrahlung und Strahlung von grösseren Wellenlängen können harte Röntgen- und Gammastrahlung (noch) nicht mit fokussierender Optik abgebildet werden. RHESSI benutzt eine Methode der räumlichen Fouriertransformation. Neun Kollimatoren mit Doppelgittern sind gepaart mit Germanium-Detektoren und sind auf einem rotierenden Satellit installiert. Um eine räumliche Auflösung von 2.3 Bogensekunden (für den Kollimator mit der kleinsten Gitterkonstanten) zu errreichen und um mit Beobachtungen von anderen Wellenlängen genau korrelieren zu können, sind zwei präzise Aspektsysteme implementiert worden; zum einen das "Solar Aspect System" (SAS, solares Aspektsystem) und zum anderen das "Roll Angle System" (RAS, Rollwinkelsystem). Das SAS misst die Ausrichtung des Teleskopes relativ zum Sonnenzentrum mit einer Genauigkeit im sub-Bogensekundenbereich und das RAS liefert genaue Kenntnis des Rollwinkels des Satelliten. Das kombinierte SAS/RAS-Aspektsystem liefert Kenntnis der absoluten Ausrichtung des Teleskopes mit einer Genauigkeit von einer Bogensekunde.

In dieser Doktorarbeit wird das Design, die Kalibration und die Genauigkeit des Aspektsystems von RHESSI beschrieben. Die Rekonstruktion der momentanen Lage und Orientierung des Teleskopes (aspect solution) ist präsentiert und die Messung der Position der harten Röntgen- und Gammastrahlungsquellen wird gerechtfertigt. Für zwei Flares der X-Klasse werden die Positionen der Fusspunkte als Funktion der Zeit gemessen, und diese werden mit der totalen deponierten Energie korreliert. Die Implikationen dieser Korrelation auf die räumlichen Ausmasse des Reconnections-Gebietes wird diskutiert.

Chapter 1

Introduction

This thesis contains two main parts; an instrumental and an astrophysical/observational part. Both are introduced in this chapter. The astrophysical part is introduced first in section 1.1, followed by the introduction of the instrumentation in section 1.2, whereas chapter 2 describes the instrumentation first, followed by chapter 3 describing astrophysical observations. A more detailed outline is given in section 1.3.

1.1 Solar Physics with RHESSI

1.1.1 A Historical Line Toward Solar Physics

Asking N epistomologists about the driver of human beings for their great effort into science would probably lead to more than $N + 1$ approaches to an answer. One approach goes certainly along the line of primal questions such as, “Where do we come from?”, “What is the nature of the world we are living in?”, and “What are the laws of nature?”. Since ancient time, humans were looking up to the sky trying to understand and interpret the phenomena they discovered, hence making astromony one of the original scientific fields of interest. Discerning the Sun as an essential source for living on the Earth and, later on, as the by far closest star make it a prime object of interest.

As the Sun is a complex object and a wide variety of research fields have been established, let’s focus on a few events leading to today’s research with RHESSI. Several early observers claim the discovery of sunspots. The ancient Chinese recorded dark features on the Sun seen with the naked eye in 28 B.C. Then in 1610, Galileo Galilei risked blindness by looking at the Sun through a *telescope* descovering spots on the Sun. Trying to detect unkown planets, by 1843 H. Schwabe (Dessau, Germany) suspects regular variations after collecting data for 17 years. Later, A. von Humboldt continues Schwabe's data collection and publishes it in 1851; henceforth, establishes interest in *11-year sunspot cycle*[1]. Influenced by Schwabe's discovery, R. C. Carrington was observing a prominent group of sunspots on Sept 1, 1859, when suddenly "two patches of intensely bright and white light broke out". Carrington discovered a *flare* - the rare variety that is visible in white light. R. C. Carrington and R. Hodgson independently observed a solar flare in the white light of the photoshere. By observing the Zeeman splitting of spectral lines, G. E. Hale concludes in 1908 that sunspots were *intensely magnetic*; and a few decades later, in 1944, R. S. Richardson proposes the term *solar flare* for sudden, bright, rapid, and localized variations detected in Hα line of the chromospere. First detection of *Soft X-rays* from the Sun has been reported in 1949 by T. R. Burnight, studying a flare on August 6, 1948 with a rocket experiment performed by the U.S. Naval Resarch Laboratory. In 1963, K. de Jager and M. R. Kundu explain the similarity in the time profiles of centimeter wavelength, impulsive radio bursts, and Hard X-ray (HXR) radiation in terms of the same *energetic electrons* producing the radio and HXR.

1.1.2 Solar Flares

With the study of the chromospheric Hα line, the reports of flares became much more frequent, and also increasingly complex. Although the term *solar flare* has originally been defined to coincide with Hα observations, it has been proven too narrow. In fact, a wide range of rather complex phenomena has been observed. Today, a flare can be understood as a sudden brightening from white light to X-rays and Gamma-rays. Within tens of minutes, an enormous amount of energy is released ranging from less than 10^{24} ergs (current detection limit) up to 10^{33} ergs, corresponding to billions of megatons of TNT. The time scale varies from events of a few minutes to events with a decay phase of a few hours. In X-rays, the flux can increase by four or more orders of magnitude within minutes. Flares occur near sunspots, usually along a magnetic neutral line.

Observations show various "faces" dependent on the wave length of the electromagnetic spectrum. Most explanations of observations of solar flares involve a scenario of reconnection of magnetic field lines. In the following, an overview of the general scenario is given by focusing on mechanisms and observations which are relevant to this work. This scenario is illustrated by Fig. 1.1.

---

[1] R. Wolf, who was initially in Bern and later in Zürich, Switzerland, devised the "Zürich sunspot number" in 1848.

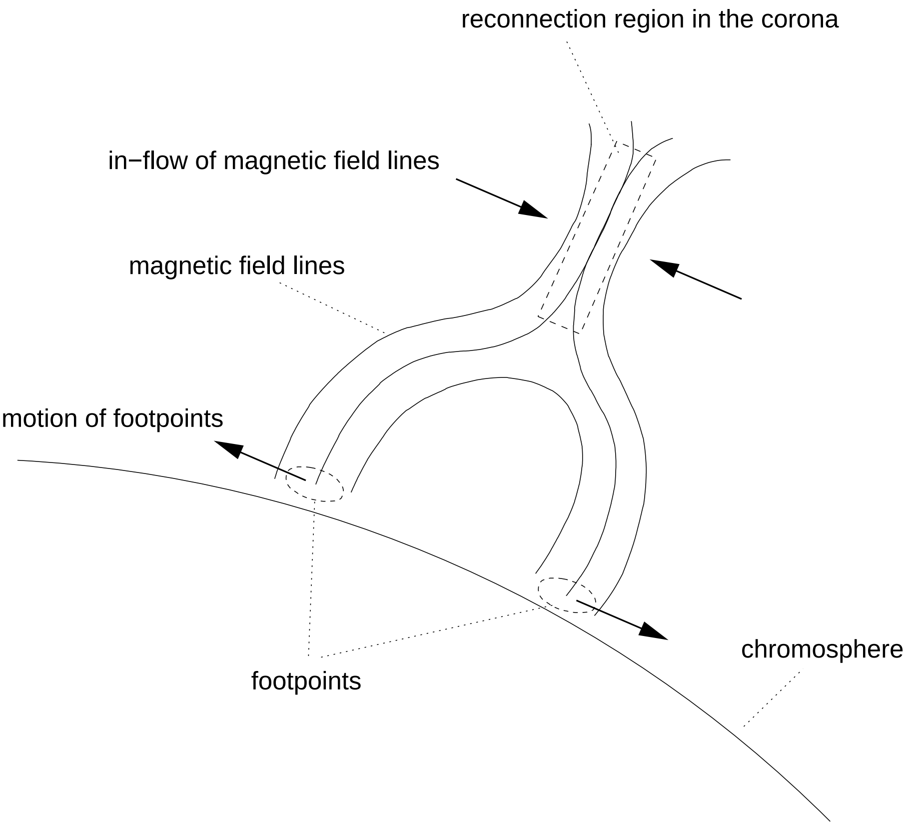

Figure 1.1: General scenario of magnetic reconnection. While more and more magnetic field lines are flowing into the reconnection region, particles are accelerated and, trapped in the magnetic field, producing Bremsstrahlung (X-rays) at the footpoints in the chromosphere.

Excess magnetic energy might be produced in the corona when plasma motion at or below the photosphere shear and twist magnetic field lines. Magnetic field lines of opposite polarity can approach and a change of field topology can lead to a lower energy state, releasing magnetic energy (magnetic reconnection). Electrons and protons which are accelerated in the reconnection region are trapped in the magnetic field and travel along the field lines out into the higher corona and along the magnetic loop towards the chromosphere. As the electrons encounter plasma of higher density at the chromosphere, they lose all their energy primarily through Coulomb collisions and therefore, producing Bremsstrahlung (hard X-rays) at the footpoints of the loop.

As more and more magnetic field lines are reconnected, larger and larger loops are formed. While the footpoints represent the magnetic field tubes in which the accelerated electrons are injected, the footpoints move to field lines which are currently reconnected. Therefore, the footpoints at the chromosphere show an apparent motion while field lines are reconnected in the corona.

Figure 1.1 shows a two dimensional model of reconnection. In three dimensions, processes can be more complex and the two dimensional model doesn't always hold.

1.1.3 Primary Objectives of RHESSI

The Reuven Ramaty High Energy Solar Spectroscopic Imager RHESSI is a Small Explorer mission that was launched by NASA on 5 February 2002. An introductory overview of the instrument is given in section 1.2. In this section, the RHESSI mission is scientifically motivated.

The primary scientific objective of RHESSI is to understand particle acceleration and explosive energy relase in solar flares. Yet, it isn't understood how the Sun releases the huge amount of energy (up to 10^{33} ergs), which is believed to be stored in the magnetic field of the corona, and how it rapidly and efficiently accelerates particles (electrons and ions) to high energies.

As the process of particle acceleration can't be observed directly, the hard X-ray and gamma-ray emissions are its most direct signature. Figure 1.2 shows a composite spectrum from 1 keV to 100 Mev of a large flare. At the lower end of the spectrum, emissions up to ≈ 10 to 30 keV are dominated by very hot thermal flare plasma emission with temperature up to $\approx\ 5 \times 10^7$ K. Up to tens of MeV, bremsstrahlung emission from energetic electrons produces the X-ray/gamma-ray continuum (straight lines, powerlaw spectrums). Nuclear interactions of energetic ions can dominate the spectrum between ≈ 1 to 7 MeV by broad and narrow gamma-ray lines. And finally, photons produced by the decay of pions dominate the spectrum above a few tens of MeV.

In order to resolve the spectrum which is shown in Fig. 1.2 a high energy resolution is required over four orders of magnitude. In particular, this allows determining the relative contribution between thermal and non-thermal emission to the hard X-ray spectrum. By inverting the solar flare hard X-ray spectrum a detailed spectrum of the X-ray-producing electrons is obtained.

High spatial resolution, combined with a high energy and time resolution, provides an unprecedented capability of imaging spectroscopy. The accurate localization of sources together with a good estimate of their dimensions allows the study of the energetics of flares such as determining the thermal energy content and the energy in accelerated particles.

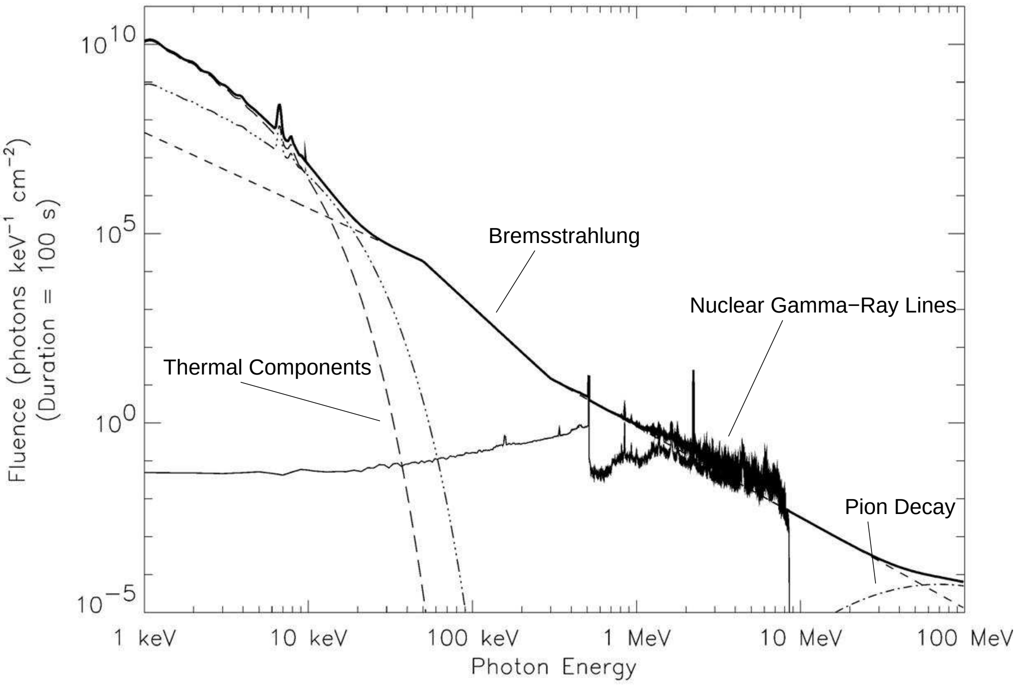

Figure 1.2: Composite X-ray/gamma-ray spectrum from 1 keV to 100 MeV for a large flare. For a describtion see text.

1.2 Overview of the RHESSI Instrument

The RHESSI scientific objectives are achieved with a single instrument providing high-resolution imaging spectroscopy observations from soft X-rays to gamma-rays. The instrument is mounted on a rotating spacecraft (15 RPM) and consists of an Imaging System, a Spectrometer, and the instrument electronics (Instrument Data Processing Unit, IDPU). Fig. 1.3 shows an overview of the instrument.

The imaging capability of RHESSI is based on a Fourier-transformation technique using nine Rotating Modulation Collimators (RMC), each consisting of a pair of widely separated grids. As the spacecraft rotates, the transmission through a grid pair is modulated (see section 1.2.1).

The Spectrometer has nine segmented germanium detectors, one behind each RMC, to detect photons from 3 keV to 17 keV. Since the spatial information is encoded in the systematic modulation of the photon count rates through each pair of grids (modulation profiles), the detectors don't need any spatial resolution, and thus can be optimized for energy resolution. Cooling the detectors to about

80 K by a mechanical cryocooler results in an energy resolution of about 1 K at 3 keV and up to about 5 K at 10 MeV.

The pointing and roll information is provided by the Solar Aspect System (SAS) and the Roll Angle System (RAS). For both subsystem, an overview is given in section 1.2.2 and they are discussed in detail in chapter 2.

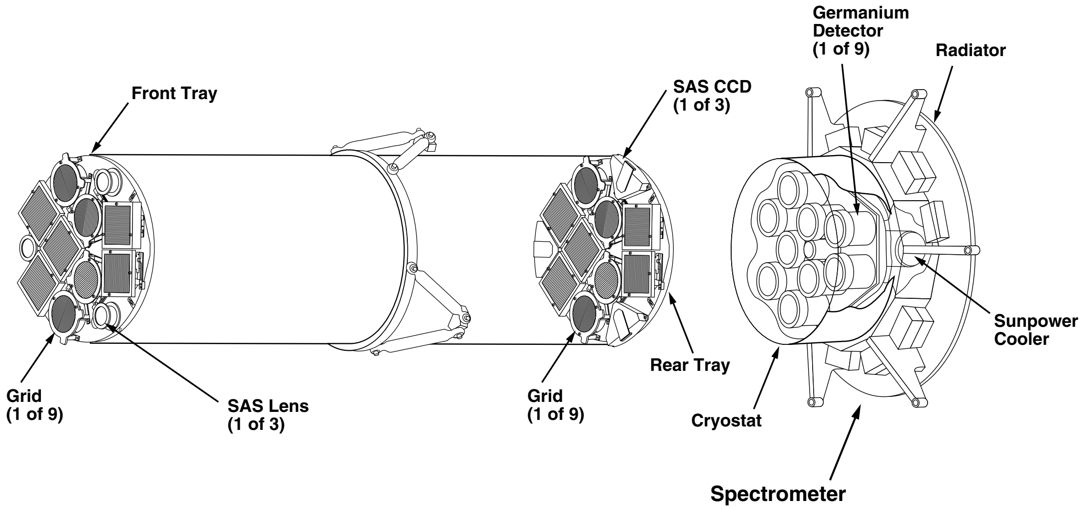

Figure 1.3: The graphics shows the main components of the RHESSI instrument. Nine grids are mounted on the front tray of the telescope, matching the nine grids on the rear tray. Behind the imager is the spectrometer including the nine cooled germanium detectors. Also shown are the three SAS lenses mounted on the front tray focusing a solar image onto the SAS CCDs on the rear tray.

The Reuven Ramaty High Energy Solar Spectroscopic Imager RHESSI is a Small Explorer mission that was launched by NASA on Feb. 5, 2002 into a circular orbit (600 km altitude, 38 degrees inclination).

1.2.1 Imaging System

The RHESSI imaging technique is described in detail by Hurford et al (2002). Nevertheless, an overview of the system is given in this section and an overview of the most widely used image reconstruction algorithms is given in section 1.2.3.

Unlike for soft X-rays and longer wavelength emissions, focusing optics are not (yet) feasible at hard X-ray and gamma-ray energies. Within the constraints of a Small Explorer mission, Fourier-transform imaging is the only realizable

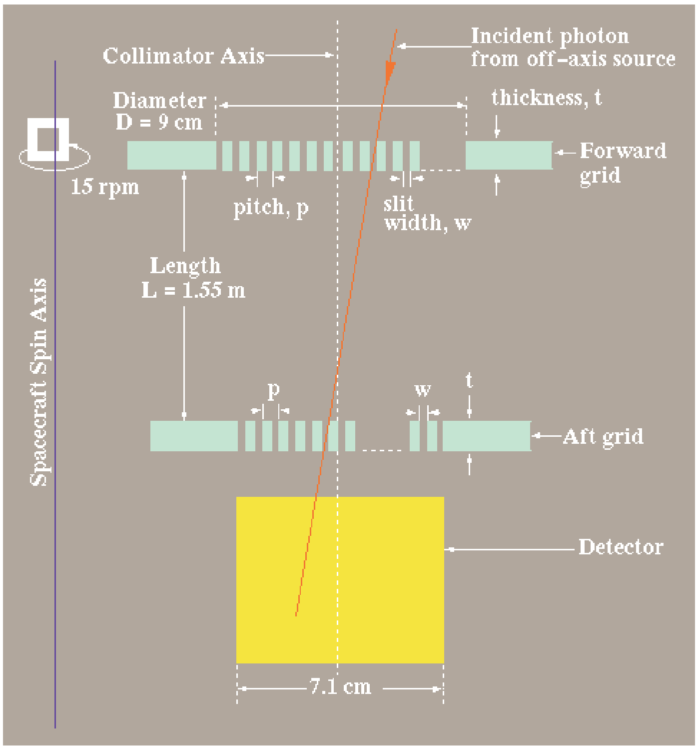

Figure 1.4:
Schematic showing the parameters that define the imaging capability.

technique to obtain arcsecond-class images in hard X-rays and gamma-rays. The used technique is in analogy to the Yohkoh Hard X-ray Telescope (HXT) (Kosugi et al., 1991).

RHESSI uses nine collimators, each consisting of a pair of widely separated grids. Each grid is a planar array of X-ray opaque slits and X-ray transparent slats (see Fig. 1.4). Within a pair of grids, the pitch p is identical and, in ideal circumstances, the orientation of the slits and slats are perfectly aligned. Whereas the transmission probability of a photon passing a single grid is 50 %, the transmission probability through such a pair of grids depends on the incident angle of the photon with respect to the collimator axis. For slits and slats of equal width, the transmission is modulated from zero to 50 % and back for a change in incident angle of the source of p/L, where L is the separation between the grids. Therefore, the angular resolution is defined as p/(2L).

For RHESSI, the separation between the grids in each RMC is $L = 1.55\,\mathrm{m}$

and grid pitches range from 34 μm to 2.75 mm in steps of $\sqrt{3}$. This results in angular resolutions that are spaced logarithmically from 2.3 arc seconds to about 3 arc minutes, allowing sources to be imaged over a wide range of angular scales.

As the spacecraft rotates, the transmission probability for a photon from a particular source is modulated. By recording the arrival time and energy, together with the aspect information, of every photon in each of the nine detectors, the photon count rates represent characteristic modulation profiles containing the spatial Fourier-components of the source.

The efficiency of the modulation for each of the 9 collimators depends critically on the alignment of the corresponding grid pair. In particular, the finest grids with a pitch of 34 μm must always be aligned within 20 arcsec in twist ($r_{Grid} \times \Delta\Phi \ll p/2$, with twist $\Delta\Phi$ and r_{Grid} radius of grid). Another necessary ingredient for image reconstruction with a resolution as high as 2.3 arcsec is the accuracy of the measurement of the pointing with respect to the collimators. Therefore, a structure had to be found which guaranteed the stability of the collimators and the aspect systems throughout the integration procedure, the launch and the thermal stress over the orbit (Zehnder et al., 2003; Thomsen et al., 2000). In addition, the definition of the coordinates for measuring the pointing has to be chosen in such a way that the axis of the collimators can always be measured with respect to sun center fulfilling the requirements in accuracy.

1.2.2 Aspect System

Since the transmission probability for a photon through the collimators depends on the incident angle with respect to the telescope axis (Hurford et al., 2002), and because the spacecraft can only be controlled on an arc minute level, the spatial resolution depends critically on a precise knowledge of the instantaneous pointing direction and roll angle. In order to have a spatial resolution of 2.3 arc seconds (for the finest grid) and to precisely correlate with observations at other wavelengths (absolute positions of sources!), two precise aspect systems are implemented, the Solar Aspect System (SAS) and the Roll Angle System (RAS). The SAS yields sub-arc second knowledge of the radial pointing with respect to Sun center and the RAS provides precise knowledge on the roll angle of the rotating spacecraft (about 15 RPM). The combined SAS/RAS aspect system provides a knowledge of the absolute pointing with an accuracy of 1 arc second.

Both subsystems, SAS and RAS, are discussed in detail in chapter 2.

1.2.3 Image Reconstruction

RHESSI provides no direct imaging. For every incoming photon, the arrival time together with its energy is stored. Binning the photon-list in time leads to the characteristic modulation profiles discussed above. The images, or maps, have to be reconstructed from these modulation profiles together with the associated reconstructed aspect solution. In the following, an overview of the three most widely used image reconstruction methods is given. A more comprehensive overview is given by Hurford et al. (2002).

Back Projection

Back projection is the most basic and straightforward method of reconstructing an image, and it is equivalent to a inverse Fourier transform.

Conceptually, a photon is projected back through the bi-grid collimator producing a stripe-like pattern of probabilities for the source of the photons. For this projection, the instantaneous pointing and roll angle of the telescope has to be taken into account. By binning the photon counts in time and associating the correspondent aspect solution (pointing and roll angle), the summation of the stripe-like probability patterns builds up high values at the location of the real source. In order to consider all possible roll angles, the summation has to span at least one half-rotation of the spacecraft (2 seconds).

Back projection is a linear process; and therefore, maps for arbitrary time intervals and energy ranges can be added and subtracted. A back projection map is the so-called “dirty map” (in analogy to radio interferometry); it can be improved by applying e.g. a CLEAN algorithm.

CLEAN

A back projection map of a point source is proportional to a zero order Bessel function (Hurford et al., 2002), i.e. the point spread function. Therefore, any back projection (“dirty”) map shows side lobes. It can be improved with non-linear algorithms like CLEAN.

CLEAN is based on the assumption that an image can be well represented by a superposition of point sources. Knowing the instrument’s Point Spread Function (PSF), the “dirty” map can hence be approximated by a superposition of the convolution of a point sources with the PSF. The algorithm is iterative and keeps track of a “residual map” and a table of “clean component”. The initial residual map is the backprojection map and PSF’s with a gain factor at the position of clean components are subsequently subtracted from the residual map, until one of the stop criterion is met (number of iterations, negative peak in residual map exceeds the largest positive peak, or observed modulation profile agrees well with the predicted from the clean components).

For the final clean map, the clean components are convolved with a Clean PSF, which is a gaussian with the FWHM reflecting the effective resolution of the collimator used for the dirty map. To provide a visual estimate of the noise, the final residual map is added to the clean map for display.

Forward-Fitting

The Forward-Fitting method uses a different approach. It is based on the assumption that the observed modulation profiles, and therefore the map (or image), can be approximated by a relatively small number of elemental sources, and each of those can be characterized by just a few parameters.

The maps of multiple elemental sources (circular, elliptical, or curved elliptical Gaussians) are created, and a model modulation profile is calculated. By iteratively adjusting the parameters of the model, the model modulation profile is fitted to the observed modulation profile. Hence, the “pixelized” map of the elemental sources iteratively converges into the best-fit image, which yields well-quantified parameters such as source locations.

The implemented Forward-Fitting method is described in detail by Aschwanden et al. (2002).

1.3 Outline

After an introduction and motivation for an aspect of todays research in the physics of solar flares has been given in section 1.1 an overview and introduction to the RHESSI instrument has been presented in section 1.2. In the following a more detailed outline of the thesis is given.

Chapter 2 describes the intrumental part of this thesis. As the RHESSI instrument has been introduced above, two precise aspect system are required in order to reconstruct and locate hard X-ray and gamma-ray images. The design and the calibration is discussed in detail.

First, the Solar Aspect System (SAS) is discussed in section 2.1. The SAS provides accurate knowledge of the pointing of the telescope axis with respect to the center of the solar disk. By doing so, it measures the solar radius with a high frequency and a hugh database of measurements ($\approx 6 \times 10^9$) has been aquired in the first years of operation. In section 2.1.7, an overview of first results of analysis of those measurements is presented.

The Roll Angle System (RAS) of the RHESSI instruments is discussed in section 2.2. The RAS provides accurate knowledge of the roll angle of the rotating spacecraft. As such an instrument has never been built before, its design, calibration and data processing is discussed in detail.

In section 2.3, an overview of the Aspect Data Processor (ADP) is given. The ADP is the in-flight processor for the SAS and the RAS data providing the formatted aspect data to the spacecraft. The data are in a raw format and have to be analysed by the on-ground software.

The reconstruction of the aspect solution is discussed in section 2.4. The instrumental part is concluded with an estimate of errors of the aspect solution given in section 2.4.3.

Most of the work in chapter 2 has been published in a series of papers and presentations (Fivian et al., 2004, 2003b,a; Zehnder et al., 2003; Fivian et al., 2002; Thomsen et al., 2000; Fivian et al., 2000; Henneck et al., 1999a,b).

Chapter 3 contains the astrophysically observational part of this thesis. Footpoint motions and spectra of the footpoints of two large flares (GOES X-class) are observed. According to the reconnection model which is introduced in section 1.1.2, the motion should be correlated to the deposited energy. Using the unprecedented spatial, spectral and temporal resolution of RHESSI, a quantification of this correlation allows conclusions on the geometry of the reconnection region of the flare. While prelimiary results has been presented at astrophysical meetings (Fivian et al., 2003c), this work is to be published (Astrophysical Journal).

Chapter 2

The RHESSI Aspect System

The Reuven Ramaty High Energy Solar Spectroscopic Imager RHESSI is a Small Explorer mission that was launched by NASA on Feb. 5, 2002 into a circular orbit (600 km altitude, 38 degrees inclination). The primary scientific aim of the mission is to investigate the physics of particle acceleration and energy release in solar flares. RHESSI observes the full Sun with an unprecedented combination of spatial resolution (as fine as 2.3 arcsec) and energy resolution (1 keV to 5 keV) in the energy range from 3 keV to 17 MeV. The single instrument on a spin stabilized spacecraft utilizes Fourier-transform imaging with 9 bi-grid rotating modulation collimators spaced at 1.55 m and 9 cooled germanium detectors (Lin et al., 2002).

Since the transmission probability for a photon through the collimators depends on the incident angle with respect to the telescope axis (Hurford et al., 2002), and because the spacecraft can only be controlled on an arc-minute level, the spatial resolution depends critically on a precise knowledge of the instantaneous pointing direction and roll angle. In order to have a spatial resolution of 2.3 arcsec (for the finest grid) and to precisely correlate with observations at other wavelengths, two precise aspect systems are implemented; the Solar Aspect System (SAS) and the Roll Angle System (RAS). The SAS yields sub-arcsec knowledge of the radial pointing with respect to sun center and the RAS provides precise knowledge on the roll angle of the rotating spacecraft (about 15 RPM). The combined SAS/RAS aspect system provides a knowledge of the absolute pointing with an accuracy of 1 arcsec. Fig. 2.1 shows an overview of the imager including the SAS lens, the SAS sensor and the RAS.

The description of the aspect system is organized in four sections. In the first two sections the two systems, the SAS and the RAS, are described. Then an overview of the aspect data processor (ADP) is given and finally, the reconstruction of the aspect solution is discussed.

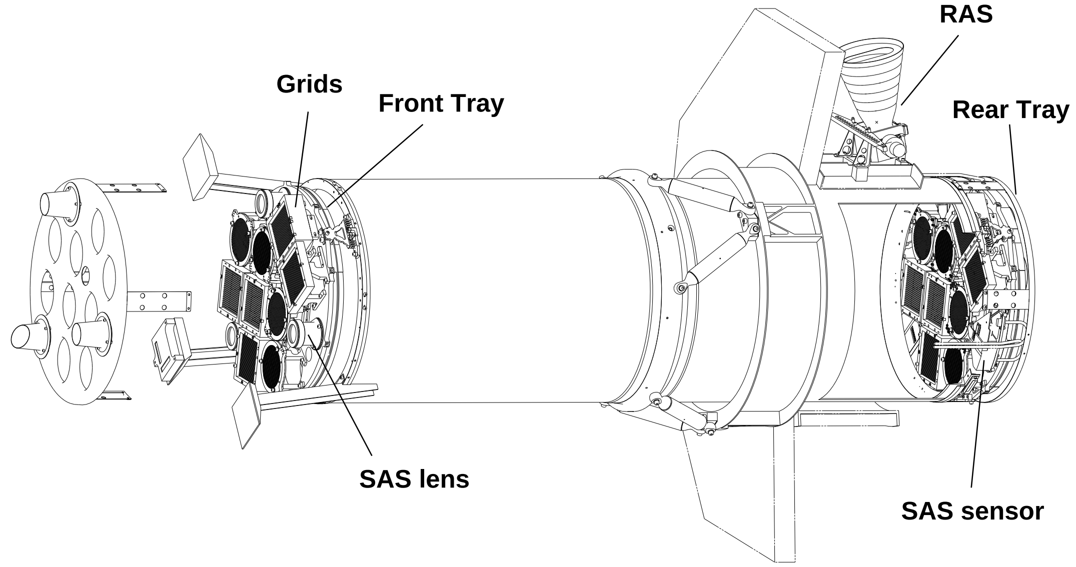

Figure 2.1: The drawing shows an overview of the imager. The SAS lens are mounted on the front tray together with the front grids and the SAS sensors are mounted on the rear tray together with the rear grids. The RAS is pointing radially outwards with respect to the telescope axis.

2.1 Solar Aspect System (SAS)

2.1.1 System Overview

The purpose of the SAS is to measure the instantaneous pointing of the imager (the telescope) with respect to the center of the solar disk. The knowledge of the sun center in the rotating frame together with the roll angle of the spacecraft is a necessary ingredient to reconstruct X-ray images from the modulation patterns. After giving a brief overview of the SAS, its design is described in more detail (section 2.1.2), the CCD is characterized (section 2.1.3) and the modeling of the data is described (section 2.1.4). The ground and the flight calibration is discussed in the sections 2.1.5 and 2.1.6. The SAS-section is completed with an outlook of measuring the solar radius using the SAS (section 2.1.7).

The SAS consists of a set of 3 identical lens/sensor subsystems. Each subsystem consists of a 4 cm diameter lens located on the front grid tray of the imager tube. The lens focuses a solar optical image onto a 2048-element x $(13\mu\mathrm{m})^2$ linear CCD located on the rear grid tray. The orientation of the three linear CCDs are equally spaced at 120 degrees. The focal length, given by the length of the imager tube, is 1.55 m resulting in a plate scale of 1.73 arcsec/pixel. In order to reduce chromatic aberration a bandpass filter at 670 nm with 12 nm bandwidth (FWHM) is used. While each of the three CCDs are sampling solar profiles with 128 Hz using a programmable integration time between 0.02 and 2 ms, the digitized signal is sent to the aspect data processor (ADP) where a hardware programmed algorithm identifies (triggers) one or several pixels around the solar limb using an adjustable threshold. Typically 4 pixels for each of the 6 limbs are written to the telemetry packets using an 8 or 10 bit resolution.

The transmitted data of each of the 6 Solar limbs are processed off-line by the ground based analysis software, where the position for each limb on the CCDs is determined. For ideal circumstances and with exactly known positions (lens optical center, CCD pixel location), the mid-perpendicular of the three chords, i.e. the straight line between the two limbs on each CCD, would intersect in one point; the momentary position of the sun center. Fig. 2.2 illustrates this reconstruction of the sun center. Given the accuracy of our dimensional measurements and given thermal and mechanical instabilities, the mid-perpendiculars usually do not intersect in one point but form a residual triangle. The best guess for the sun center is then the center of gravity of the three intersects of the mid-perpendiculars. The reconstruction of the aspect solution, and in particular the pointing, is discussed in see section 2.4.1.

Measuring the location of six solar limbs over-defines the sun center. This

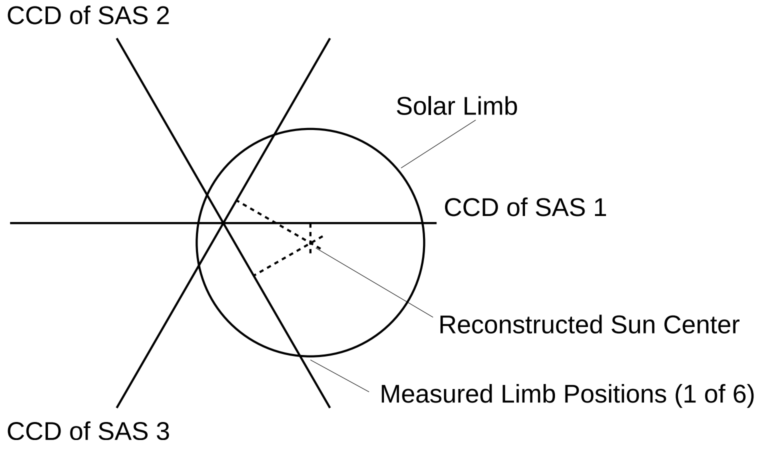

Figure 2.2: Reconstruction of the sun center. The circle indicates the limb of the solar image and the three lines indicate the three linear CCDs. The intersection of the solar limb with the CCDs defines six positions of the solar limb with respect to SAS which allows a reconstruction of the sun center.

redundancy in the data allows a in-flight self-calibration which is discussed in section 2.1.6. Mechanical instabilities, in particular a tray-to-tray twist, would lead to a change of the relative positions of lens and sensors and can therefore be monitored by the SAS throughout the mission.

It's shown in section 2.4.3 that the requirement of a relative pointing error of $\sigma \leq 0.4\,$arcsec can easily be achieved by the implemented system.

2.1.2 Design of Sensor System

In principle, the measured solar pointing is related to the SAS features only. In order to have the measurements immune to bending of the imager tube, a design has been chosen to have the lenses coplanar with the front grids and the CCDs coplanar with the rear grids.

The plano-convex lens with a focal length of 1.55 m are made of fused silica and are fixed in a special spring-loaded aluminum mount. The bandpass filter is made in two stages. The narrow bandpass filter is coated on the lens while a filter blocking the regions far away from the bandpass is coated on a glass-plate directly in front of the CCD. The glass-plate is tilted by 6 degrees in order to deflect the CCD reflected light away from the CCD. The CCD (Loral 145 EDC) is glued to an Al standoff, which is bolted to the rear grid tray to guarantee stable positioning. The standoff reaches through a rectangular hole in the PC-board;

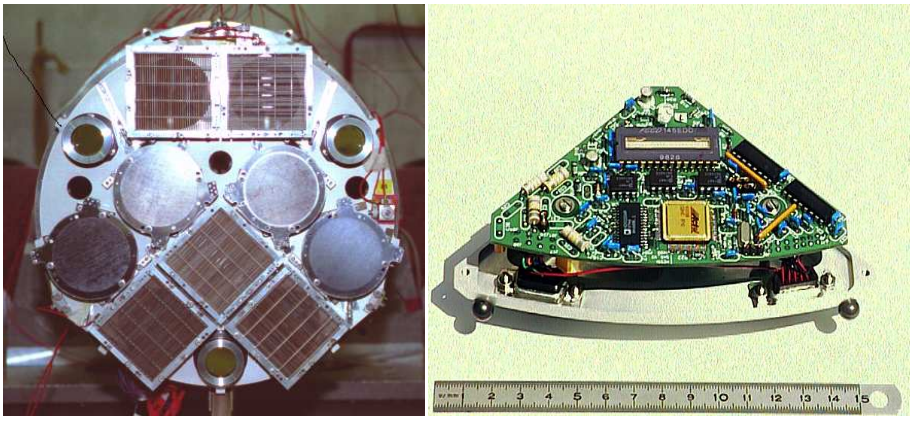

Figure 2.3: The left picture shows the front tray with the three SAS lenses and the right picture shows the SAS front-end electronics with the CCD.

therefore the position of the CCD is defined by the standoff rather than by the PC-board. Fig. 2.3 shows pictures of the front tray and the front-end electronics of the sensor box including the CCD.

Each of the three CCDs are sampling solar profiles with a high rate of 128 Hz, which anticipates possible fast deviations in pointing. The stability of the sensitivity of the systems was not known prior to launch. Therefore, the integration time is programmable between 0.02 and 2 ms with a nominal integration time of about 500 μs. The digitized signal is sent to the Aspect Data Processor (ADP) where a hardware-programmed algorithm triggers one or several pixels around the solar limb using an adjustable threshold. The amplitudes of typically 4 pixels for each of the 6 limbs are written to the telemetry packets using 8 or 10 bits precision. Modeling of the data (section 2.1.4) showed that the requirement of measuring the pointing better than 0.4 arcsec (rms) at all times are met and in section 2.4.3 an estimate of the accuracy of in-flight data is discussed.

Each SAS sensor is running with a constant cycle timing at 128 Hz. Within every cycle of $\approx$8 msec, the sunlight is integrated on the pixels of the CCD. The accumulated charge is shifted out with a frequency of 1 MHz and sampled twice, once at the offset level and once at the signal level. The subsequent digitization at the 12 bit ADC (analog digital converter) provides a resolution of 0.5 mV/channel (2V/2^{12} channels $\approx$ 0.5 mV/channel). To remove the charge of the continuously incident sunlight, the readout of the CCD follows a pre-readout that removes most of the charge accumulated during off-integration time. The front-end electronics incorporates a Field Programmable Gate Array (FPGA; Actel RH1020) to provide basic control of the sensor. In the normal operational mode, the difference of the two samples is calculated and bits 1-10 are sent to the ADP via a synchronous serial link with a speed of $0.1\,\mu$sec/bit or $1\,\mu$sec/pixel. By using the difference of the two samples, the reset noise of the CCD is essentially eliminated. In order to have the full resolution on the 10 bit range of the digital system, the integration time is currently programmed to be $\approx 700\,\mu$sec as described by Fivian et al. (2002). Beside the normal operational mode, several test and diagnostic modes (first-level modes) are implemented in the front-end FPGA (see appendix B).

On the ADP, the SAS data are processed first by a hardware program in the second-level FPGA (SAS/RAS FPGA) and then by the software running on the Data Signal Processor (DSP). For every SAS cycle (i.e. every 8 msec), the three measured solar profiles are stored in the SAS/RAS memory on the ADP. At the same time, while the data are flowing through the FPGA logic, the addresses of all trigger level transitions are stored. The trigger levels are programmable and are stored in a FPGA register. In order to minimize the data rate consistent with the required pointing accuracy, a cadency divider is implemented which produces SAS interrupts to the DSP program with 128, 64, 32, 16 or 8 Hz. The nominal operational cadency of 32 Hz results in an additional pointing error of the order of 0.05 arcsec for linear interpolation between the measured points. However, the limited telemetry rate and a photon count rate that is higher than expected prior to launch required a reduction of the cadency to 16 Hz. The potentially increased interpolation error can be compensated by using a quadratic interpolation for pointing values between measured data points. An overview of the ADP is given in section 2.3.

2.1.3 CCD characterization

The precision of the measurement of the solar pointing depends essentially on the determination of the position of the solar limb on the CCD and therefore on the performance of the CCD itself. In order to optimize the accuracy of the limb determination and at the same time keeping the data rate acceptable, the front-end electronics has been tuned to have a low and constant (over pixel range and time) noise ($\leq$ 1 mV), a stable dark signal, and a stable, pixel-independent gain. Since the sun center is determined from the average of the two limb positions on each CCD, effects due to a potential non-linearity of the signal response cancel in first order.

Most lab tests have been performed using a simulated sun image (a Xenon arc lamp followed by a condenser and a 670 nm bandpass filter at room temperature (Henneck et al., 1999a). The sensitivity has been checked by illuminating the

CCD with an attenuated lab sun, which has been calibrated by using a calibrated photo-diode. The result is compatible with the CCD specification to within 30%. Moreover, the measured sensitivity of the whole SAS system including lenses and filters agreed with expectation on a level of about 20% (see below).

Dark signal

The dark signal is the output signal in the absence of light and originates mainly from integrated dark leakage current and thermodynamic noise. Its amplitude can be influenced by the photo-gate voltage which, however, also affects the odd-even effect (see below) and thus was adjusted for a reasonable compromise. Fig. 2.4a shows the dark signal for SAS 2 at a typical operating temperature of about 20 degreeC for the electronic box. The pixel averaged dark signal was $\leq$ 2.5 mV for all CCDs measured and was found to depend very little on temperature; i.e. the maximum variation observed was 2 mV over the range from 0 to 55 degreeC. This clearly deviates from the usual dark signal dependence which states that the dark signal doubles for every 7 degreeC increase in temperature. The most surprising feature is the pixel-to-pixel non-uniformity within certain pixel regions. However, one can easily correct for this behavior since the dark signal characteristics is very stable.

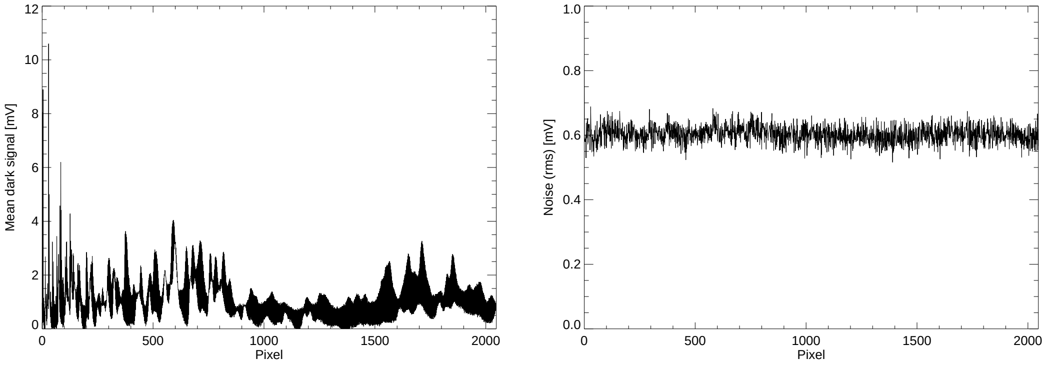

Figure 2.4: The left plot shows the mean dark signal for SAS 2. Although the dark signal is not uniform over the pixel range, it is stable in position and time. The right plot shows the noise (rms) of SAS 2. The results for SAS 1 and 3 are similar.

Noise

The full system noise for the dark signal is between 0.4 mV to 0.6 mV (rms) and represents the average of the individual pixel rms values as a function of time (see Fig. 2.4b). This is below the ADC resolution to be used ($\geq$ 1 mV/ch) and will therefore only have a negligible influence on the SAS performance. The measured noise values are roughly consistent with the value of 1 mV given by CCD manufacturer Loral for the peak-to-peak temporal noise, if one bears in mind that our ADC resolution is 0.5 mV/ch. It corresponds to roughly 370 electrons using a typical voltage-to-charge conversion factor of 1.2 μV/e- given by the output node capacity.

Hot and cold pixels

A hot (cold) pixel is a pixel the response of which is permanently above (below) a certain, critical high (low) threshold. To test for these pixels, the entire CCD areas has been illuminated with moderate intensity (around 100 mV, about 10 % of the dynamic range). Using a high (low) threshold of about 1000 (50) mV no such pixels were found for all four flight CCDs.

Odd-even effect

'Odd-even' or 'register imbalance' describes the fact that odd and even pixels may have a different gain factor and respond in a typical staggering pattern to a uniform light input. Its cause is usually related to the fact that although the charges for the odd and even pixel are converted to voltages in the same pre-amplifier they are shifted out via separate shift registers on either side of the central photo-site line. Here, two effects must be considered separately: a 'global' pixel-independent odd-even effect and a 'local', pixel-dependent one.

The global odd-even effect varied considerably from CCD to CCD (by up to a factor 10) and was observed to be as large as $\Delta_{norm} = 2\cdot(<\text{odd}> - <\text{even}>) / (<\text{odd}> + <\text{even}>) \leq 0.05$ after implementation of the pre-integration scheme (Zehnder et al., 2003). This value is consistent with the specifications. It was also found that the odd-even effect could be minimized to some extent by selecting the photogate voltage which however also determined the amplitude of the dark signal amplitude. If always the same pixel regions were illuminated the odd-even differences $\Delta = <\text{odd}> - <\text{even}>$ were found to be a linear function of the mean amplitude $(<\text{odd}> + <\text{even}>)/2$, however with finite offsets at amplitude zero.

Therefore, a correction should be applicable (see also Seige and Ress, 1986, 1987) if it were not for the presence of the local odd-even effect. The latter means that illuminating certain regions of the CCD affects the gain of either all the even or all the odd pixels. For instance, illuminating the pixel area around pixel 1850 raises the amplitude of all even pixels by about 0.8%. The effect depends critically on the illumination geometry and is enhanced by using light with more infrared components. This is caused presumably by illuminating certain areas of the transfer gates and of the odd or even shift registers lying on opposite sides of the central photo-diode line which are not deeply enough embedded so that light can penetrate and create additional charges in the odd or even shift register. Thus, the wavelength dependence of the local odd/even effect becomes plausible when bearing in mind that the absorption length of Si in the visible/IR region increases with increasing wavelength. Similar findings have been reported in the literature (Yates et al., 1987). With the pre-integration scheme implemented, the local odd-even effects could be reduced to $\Delta_{norm} \leq 0.01$ at maximum and typically $\Delta_{norm} \leq 0.005$. At low temperature (below 20 degreeC, far away from the specified range 10 degreeC to 30 degreeC), the local odd-even effect was found to increase dramatically (up to $\Delta \approx 100$ mV).

Gain homogeneity

Gain differences at the locations of the two limbs would produce a distorted solar profile which combined with a common threshold value for both limbs would yield an incorrect determination of the center. In principle, the effect can be measured and the data can be corrected for. In the lab the issue was studied by moving the CCD in front of the light source which was spatially limited to illuminate only about 400 pixels and analyzing the average gain as a function of position. In this way the illumination geometry remained approximately constant for the different measurements. The resulting gain vs. position distributions are dominated by random effects and show only a very weak correlation which is consistent with a maximum linear gain variation of $\leq 6\%$ over the full pixel range.

Linearity

The linearity of the light response has been measured over the full dynamic range using the lab sun and varying the integration time between 0.2 ms and 2 ms. The average dark signal collected over the non-illuminated pixels has been subtracted for the analysis of the illuminated pixels. The system showed no significant non-linearities.

2.1.4 Modeling

The resulting error of the reconstructed pointing can be traced back to the following three different sources.

- uncertainties in the measurement on a single CCD
- uncertainties in the co-alignment of all the SAS features
- uncertainties in the co-alignment of the SAS with respect to the grids

The co-alignment of the SAS features is discussed in section 2.1.5 and 2.1.6, respectively. The co-alignment of the SAS features with respect to the grids can be taken as a calibration of the grids only as it's pointed out in section 2.4.3. The CCD driven errors have been simulated and are presented here.

Simulating the CCD response according to a solar profile for the given optics, all the uncertainties due to the given CCD characteristics (sections 2.1.3) have to be applied. Introducing any random error in the measured solar profile will result in a displacement of the limb position. The observed profile of the limb (the limb darkening function convoluted with the point spread function of the SAS optics) is constantly sampled in flight and therefore, will be sufficiently well known. Thus, a perfect limb profile has been assumed for the simulations.

The solar profile, or the solar limb darkening, can be approximated by

$$I_\lambda(\theta)/I_\lambda(0) \;=\; 1 - u_1 + u_1 \cos\theta \,, \tag{2.1}$$

where $I_\lambda(\theta)$ is the solar continuum at the angle θ from the center of the solar disk and θ is the angle between the Sun's radius vector and the line of sight. $I_\lambda(0)$ is therefore the continuum intensity at the center of the disk (see Allen, 1973, Sec. 81). The parameter u_1 is wavelength dependent and $u_1 \approx 0.54$ at 670 nm, the center of the bandpass filter of the SAS. The point spread function (PSF) of the SAS optics has two main contributions, the diffraction on the 4 cm lens and the chromatic aberration. Prior to flight, the PSF has been estimated to have a FWHM of 4.5 arcsec (see also section 2.1.6). The simulated profile has qualitatively the same shape as the observed profile (see Fig. 2.5).

In order to estimate an upper limit for the error of the measured limb position, the following worst case values (rms) have been assumed: noise of 4 channels, an overall gain uncertainty of 3%, error in dark signal of 8 channels, odd-even effect of 3%. All simulations showed an error of the limb fit of the order of 0.1 arcsec with more or less comparable contributions from all of the four factors. Taking into account that the SAS is measuring six limbs with the geometry described above (see also Fig. 2.7), the expected relative pointing error due to the sensors is in the order of 0.05 arcsec and therefore negligible conferred the required performance of 0.4 arcsec (rms).

2.1.5 Ground Calibration

For on-ground calibration, the imager with the integrated SAS subsystem (the lenses on the front tray and the SAS electronic box on the rear tray) was operated with its ground support equipment and pointed directly at the Sun. Setting an initial pointing slightly ahead of the sun image motion, the drift of the Sun over the field of view ($\approx$ 1 degree) gives a well defined trajectory in the SAS image plane. Full CCD readouts (SAS images) were acquired with a cadency of up to 32 Hz. The solar profile shown in Fig. 2.5 is an example of a full CCD readout. SAS limbs (four or more pixels around the solar limb) could be stored with the highest cadency of 128 Hz (Fivian et al., 2000).

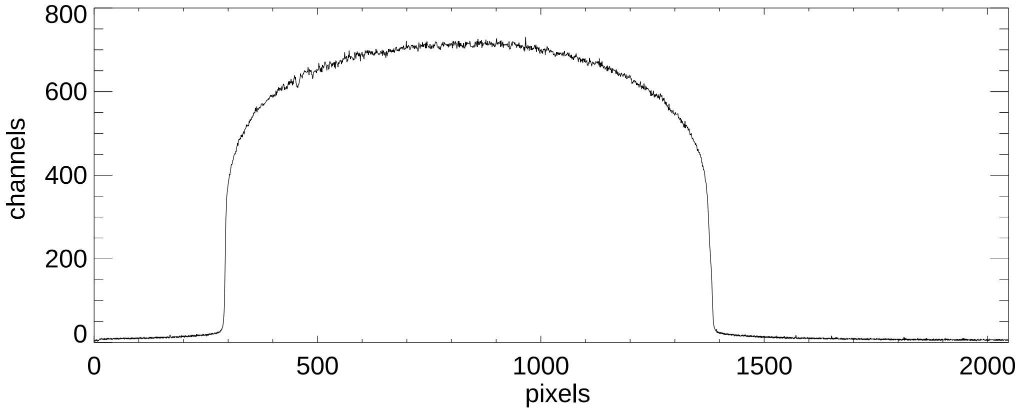

Figure 2.5: Measured sun profile, integration time $\approx 500\,\mu$s. One pixel corresponds to 1.73 arcsec.

Limb Fit and Broadening

The width of the true solar limb, i.e. the angle over which the intensity raises from zero to about 50% of the maximum intensity (for images taken at 670 nm), is in the order of 0.01 arcsec. Therefore, the measured width is dominated by diffraction, chromatic aberration, environmental and instrumental influences. Fitting the limbs with an error function adding a background which linearly increases across the limb gives a well defined width and position of the measured limb. The linear background has been added due to the wings in shown in the solar profile in Fig. 2.5. The expected width of the point spread function of the SAS optics is 1.9 arcsec (rms). On the ground, the typically measured width of the limbs of 2.5 arcsec leads therefore to a remaining broadening of 1.7 arcsec which is a realistic upper limit for the atmospheric 'seeing'. The point spread function is measured more precisely in flight (see section 2.1.6).

Geometrical Calibration

The measurement of the six limbs in the image plane of the SAS overdefines the center of the solar disk. This redundancy in the limb measurements can be used to calibrate the relative positions and orientation of the three subsystems. Good measures of the self-consistency of those geometrical parameters of calibration are the six measured solar radii, the length between the reconstructed center of the solar disk to the position of the limb and the residual triangle which is described in detail in section 2.1.6. Assuming a nominal geometry, the solar radii and the residual triangle show huge inconsistencies (see Fig. 2.6). Using the ground based measurements, the geometry of the SAS could be easily calibrated to an accuracy of 5 arcsec for the angles between the CCDs and 1.5 μm for the components of the CCD positions (see right column of Fig. 2.6). Therefore, the error of the relative pointing due to geometrical incertainties is less than 0.2 arcsec. This calibration procedure is discussed in detail in the next section. While the on-ground calibration of the geometry shows the feasibility of the self-calibration procedure, the calibration itself is discussed in the following section.

2.1.6 Flight Calibration

Measuring the alignment

Measuring the positions of the six limbs at any given time, the position of the sun center in the SAS image plane can be reconstructed. In general, the three mid-perpendiculars to the straight lines between the two limb positions do not intersect in one point but rather form a residual triangle. Fig. 2.7 illustrates the geometry of the SAS for perfectly aligned CCDs and with an arbitrary offset of one of the CCDs resulting in a residual triangle. The size and shape of the triangle depend sensitively on the relative position of lenses and CCDs. Therefore, the time series of the six measured radii and the residual triangle depend critically on the self-consistency of the calibration parameters, although the timing of the measurements is irrelevant. This can be used for the calibration of the relative

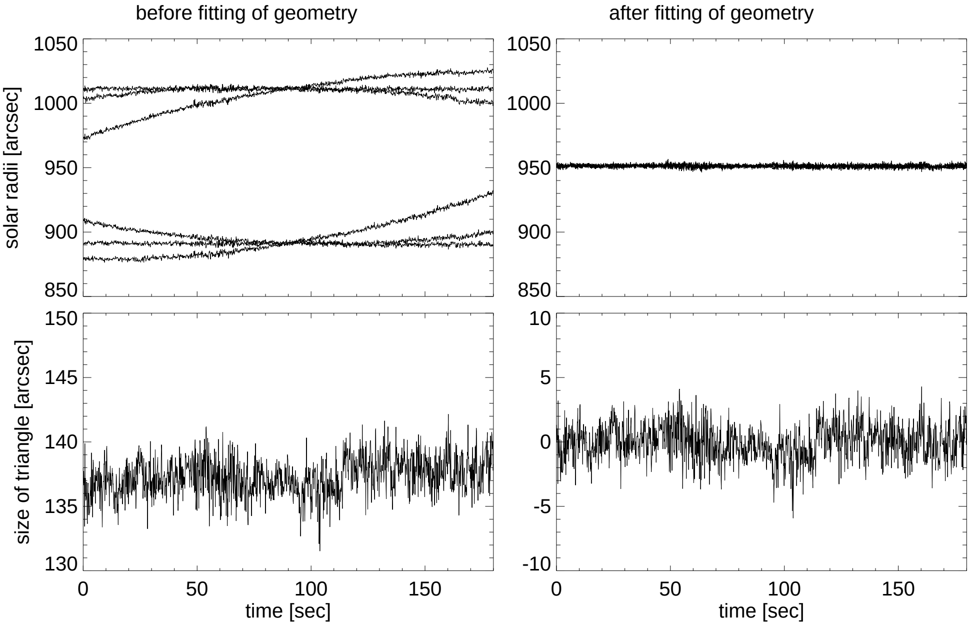

Figure 2.6: The left column of two plots show the 6 measured solar radii (upper plot) and the size of the residual triangle (lower plot), i.e. the square root of the area of the triangle, for the nominal geometry of the SAS lenses and CCDs. The plots in the right column show the same variables after fitting of the geometrical parameters of the SAS subsystems.

SAS pointing. The calibration algorithm, which has initially been published (Fivian et al., 2000), has been slightly modified to avoid any ambiguities when minimizing the size of the triangle and is summarized as follows:

1. Assume that lens/CCD no. 1 is in correct position.
2. Minimize the variance of the size of the residual triangle by varying the two undefined angles.
3. Rotate the system to make the average offset of the angles zero.
4. Minimize the size of the residual triangle by varying the position of three CCDs symmetrically in the direction of the CCDs.
5. Minimize the variance of the radii by varying the position of the three CCDs in the perpendicular direction.
6. Adjust the three plate scale to match the effective solar radius.

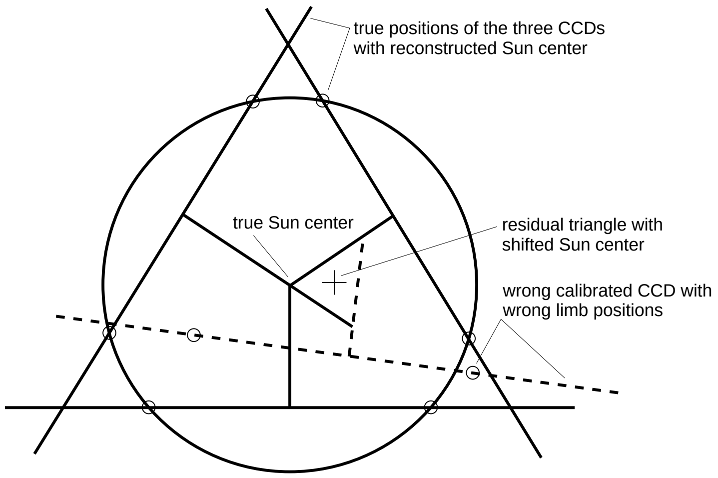

Figure 2.7: The circle indicates the solar limb and the solid lines are at the true positions of the CCDs with the corresponding reconstruction of the sun center. A wrong calibration of the position of a CCD, and therefore a wrong limb position, leads to a residual triangle in the reconstruction and hence a shifted, wrong reconstructed sun center as shown with the dashed lines.

The goal of the above calibration algorithm is a relative calibration of the SAS features (relative positions of the lenses and CCDs). The detailed prelaunch mechanical and optical measurements (Zehnder et al., 2003) are a good starting point for the optimization tasks which have to define corrections to the SAS feature in the imaging coordinate system. This coordinate system is defined using the nominal positions of the SAS features only. Since the lenses are mounted on the front tray on the same plane as the front grids and the SAS CCDs are fixed on the rear tray to be located in the same plane as the rear grids, any re-calibration of the SAS features does not effect the SAS/grid cross calibration (absolute SAS calibration) as long as the additional degree of freedom of the above algorithm is used to conserve the defined imaging coordinate system.

A scan of the parameter space showed that the minimization problems are absolutely non-ambiguous and the parameters can be fitted better than the required accuracy. The deviations from the ground based measurements are in the order of 10 μm or less for the relative positions between front and rear tray with one exception. One of the three CCDs seems to be shifted by two pixels (within 0.2 μm) which is most likely due to a glitch in the synchronization of the first pixel in one of the FPGA programs. After the calibration of all parameters, the size of the residual triangle is ≤ 0.2 arcsec (rms), which is the characteristic

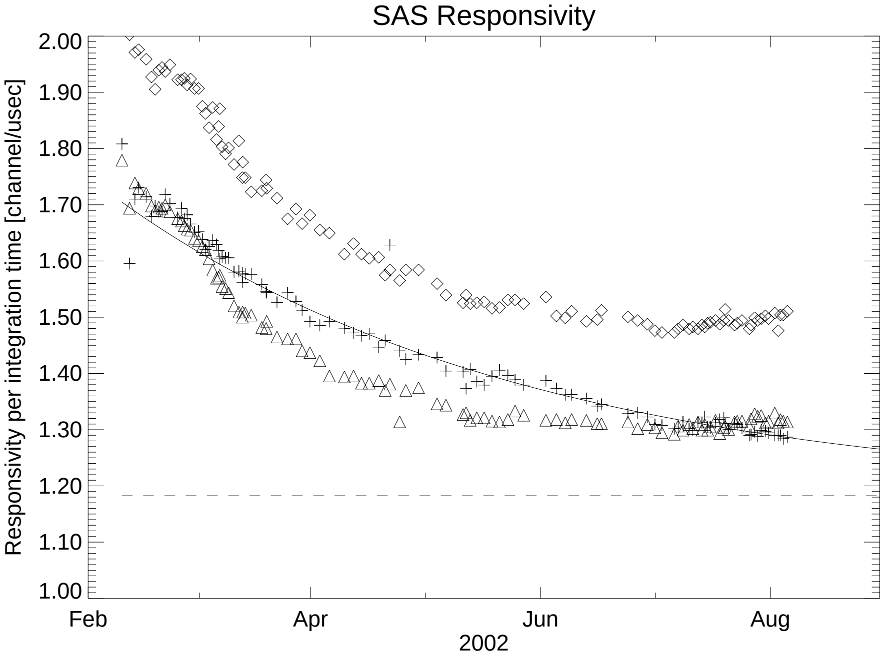

Figure 2.8: The responsivity as a function of time for each of the three SAS subsystems is measured in channels per μsec. The crosses indicate the measurements for SAS 1, the triangle for SAS 2 and the diamonds stand for SAS 3. The fitted curve for SAS 1 is an exponential with its asymptotic limit at ≈ 1.18 channels/μsec (dashed line).

length for the error of the relative pointing. The six measured radii are stable and self-consistent with a typical error of the order of 0.5 arcsec with the biggest contribution being a systematic error in the fit of the limb position on the CCD. Systematic errors in the limb-fit cancel in first order for the reconstruction of the pointing direction. Moreover, it has been shown that the structure of the imager is stable.

Sensitivity

The SAS lenses and filters (Zehnder et al., 2003) have been designed to have a peak transmission of 1.5% of the intensity at 670 nm with a band width of 12 nm FWHM. The transmissivity has been checked during the ground calibration process to have a maximum response at channel ≈ 900 on the 10 bit ADC using the nominal integration time of 500 μs. For a given time, the telescope axis can point off the sun center by as much as 14 arcmin. Therefore, the position of a limb on a particular CCD can be different by several arcsec between two consecutive integration samples using the fixed cadency of the sensors of 128 Hz. The nominal integration time has been chosen to be small enough in order to prevent additional smearing of the limbs during integration.

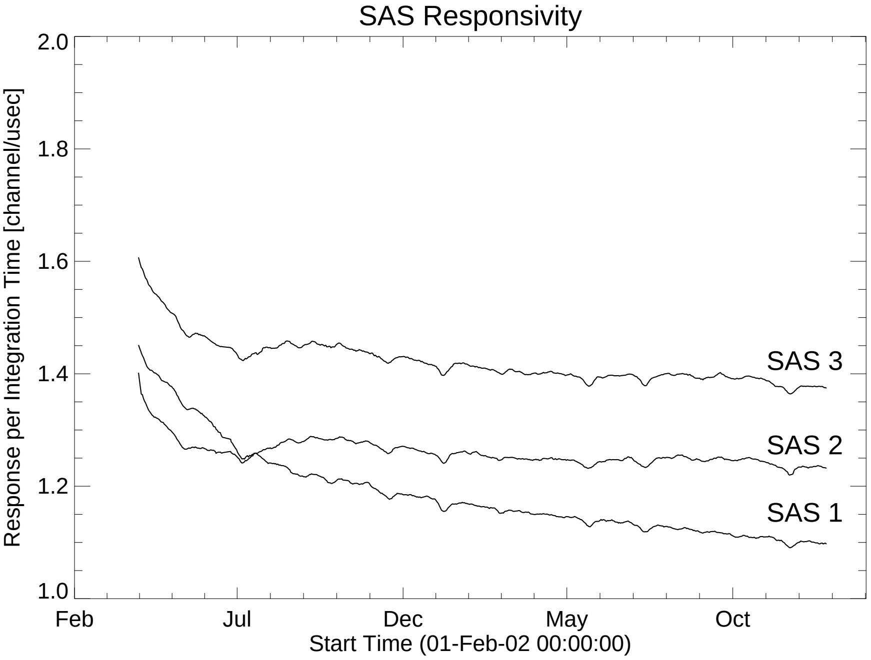

Figure 2.9: The responsivity for each of the three SAS subsystems is measured in channels per μsec. By fitting the data to a model, rejecting statistical outliers and smoothing, a smooth, accurate responsivity is measured for the three subsystems. Besides the overall decay in responsivity, a short term variation on the time scale of weeks is observed. The latter is correlated to the temperature of the sensor. (Note: two of the responsivity curves cross over at the July 2002 mark.)

Fig. 2.8 shows the measured in-flight variations of the responsivity for each of the three SAS subsystems in channels per μsec integration time. For instance, with a responsivity of 1.5 channels/μs an integration time of 600 μs is needed in order to get a response of 900 channels. It can be clearly seen that the responsivity for all three SAS's decayed about 25% in the first five month of the mission. It is believed to be due to contamination issues. Furthermore, the outgassing of the whole volume of the imager tube flew through the chimneys[1] in front of the SAS lenses which were completely uncovered since launch (Zehnder et al., 2003).

Fig. 2.8 shows approximate measurements for the early mission. For SAS 2 and 3, the degrading of the optics has stabilized within the first five months of the mission, whereas the responsivity for SAS 1 is still degrading. The data for SAS 1 is shown with an exponential fit excluding the data for the first month. The dashed line shows its asymptotic value as the current best guess for the lowest level to be reached, which is by far in the acceptable range in order to maintain the accuracy of the system.

For a more accurate correction of the response of the sensor the responsivity is measured precisely throughout the mission (see Fig. 2.9). All image readouts with a solar profile cutting close enough through the sun center are considered. For each of these profiles, the maximum response is measured with a parabolic fit through the 400 pixels at the center. Ignoring data points with poor fits and applying a box car averaging over five days leads to a smooth and accurate enough measurement of the responsivity. The smaller changes in responsivity, on the time scale of weeks, is correlated with the varying duration of exposure to sun light. With the precession of the orbit of the spacecraft the duration of the eclipse varies. The subsequent small variation of the temperature of the sensor leads to those small variations in responsivity.

Point Spread Function

The point spread function (PSF) of the SAS is dominated by the diffraction of the light by the 4 cm lens. Two other effects to be considered are chromatic aberration and deviation of the CCD from the optimum focal distance. While the focal distance can be handled well mechanically and optically, the chromatic aberration is minimized by choosing a narrow bandwidth filter of 12 nm FWHM. Thus, the core of the PSF has been estimated to be ≈ 4.3 arcsec and has not been measured prior to flight.

Using in-flight data, there is no direct way of measuring the PSF. Nevertheless, it can be estimated. Accumulating and averaging a few thousand images of the limb profile leads to a smooth averaged system response of the solar limb profile. By doing so, the measured profiles have to be normalized and corrected for radial distance to sun center of each individual pixel. The solid, smooth line in Fig. 2.10 shows the measured limb profile which corresponds to the convolution of the solar limb profile at 670 nm with the overall PSF of the SAS.

---

[1] chimneys=light baffles

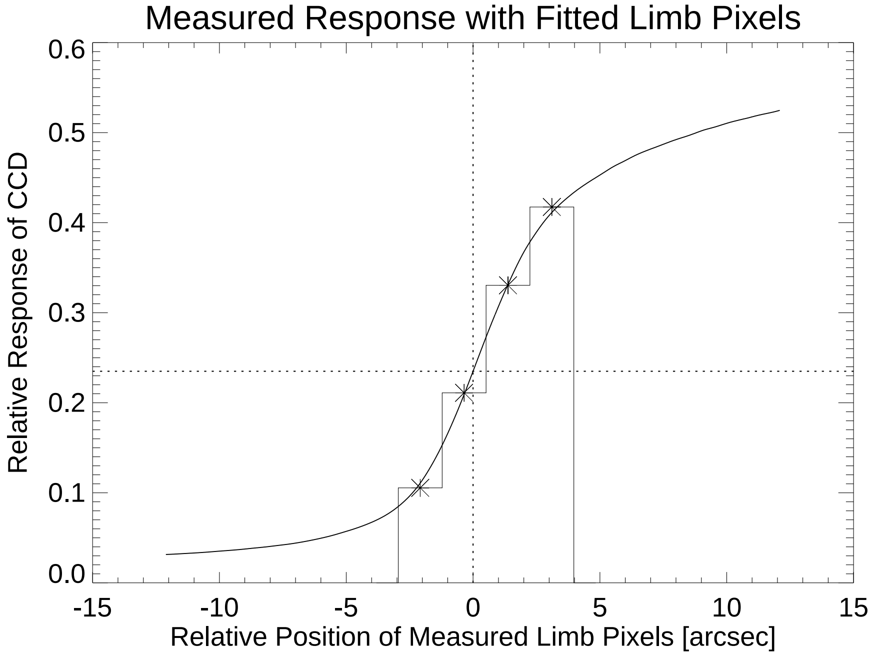

Figure 2.10: The solid line is the measured (averaged) solar limb profile, i.e. the convolution of all instrumental effects with the true solar limb at 670 nm. For every integration time, the four triggered pixels (asterisks) at each of the measured solar limb are fitted to the solar profile. This determines the limb position with an accuracy of ≈ 50 mas.

The true solar profile at the limb (or the limb darkening function) measured at 670 nm rises in essence instantaneously from zero to about 50 % of the maximum intensity at the sun center (see section 2.1.4). Furthermore, the PSF and the pixel resolution is much smaller the solar radius (≈ 950 arcsec). Approximating the solar profile by a square function with the value zero outside the solar disk and a constant value within the solar disk, the spatial derivative of the measured solar profile is a first estimate of the effective, integrated PSF and is shown in Fig. 2.11. The FWHM of ≈ 4.5 arcsec is reasonably close to the pre-flight estimate. The asymmetry in the wings of this estimate is caused by the fact that the real profile is not a constant but rather rolls off smoothly toward the sun center (see also Fig. 2.5).

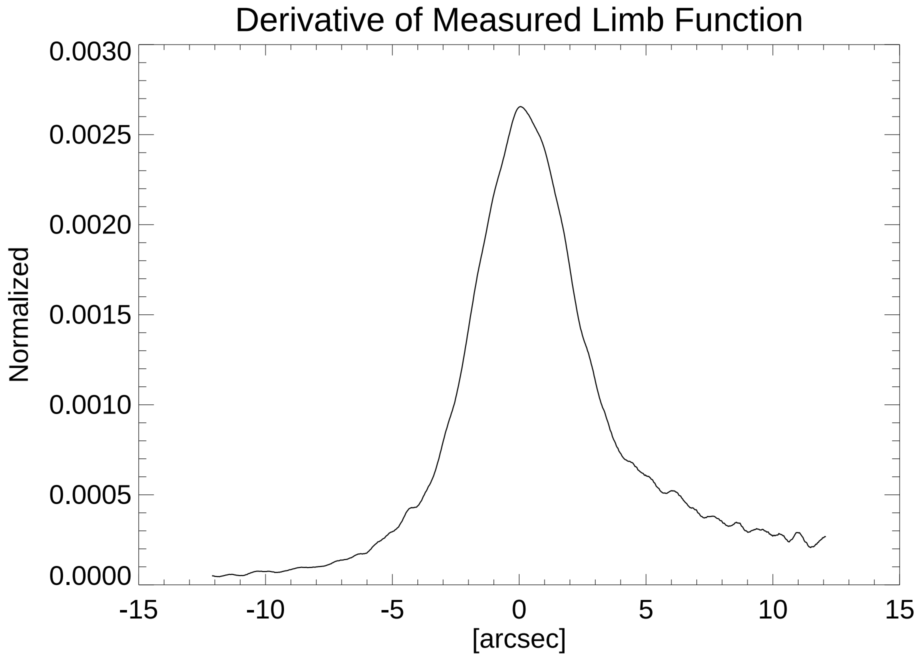

Figure 2.11: The core of the PSF of the three subsystems is estimated by taking the derivative of the measured (averaged) limb profile function (see text). The measured width of 4.5 arcsec (FWHM) is only slightly bigger than the estimated prior to flight.

2.1.7 Variations of Solar Radius

The SAS is constantly sampling the solar limb. For every sample, the limb position is fitted to each of the six measured limbs. Determining the center of the solar disk leads to six radius measurements along the circumference of the solar disk. As the spacecraft rotates with a spin period of approximately 4 seconds, the limb measurements are taken with 16 Hz and therefore, the measurements are equally distributed in position angles.

During the first three years of operation, approximately $6 \cdot 10^9$ limb measurements have been acquired. With current calibration presented in section 2.1.6, a single measurement has an accuracy of about 50 mas (milli arc seconds). Although some physical effects are orders of magnitude smaller than the precision of a single measurement, this is a huge statistics of measurements. Making use of the huge statistics of measurements together with the statistically high accuracy of single measurements, can provide results with high precision. However, the results presented in this section are preliminary and many systematical errors have not been corrected yet.

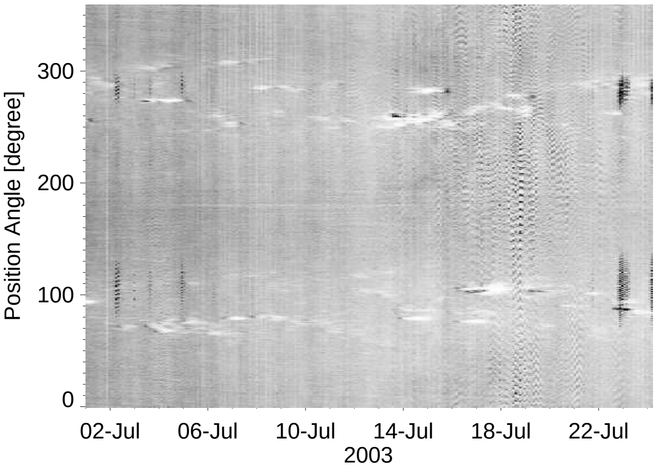

Figure 2.12: Synoptic view of limb shape data for the first half of July, 2003, with solar position angle 180 degree (South) at the middle. The faculae (larger effective radius, displayed as brightening) and sunspot (smaller effective radius, displayed as darkening) appear in the active latitudes and are brightness changes here rather than radius variations.

Averaging all radius measurements for one orbit in bins of 1 degree in position angle along the circumference of the solar disk leads to the synoptic view of the limb measurements shown in Fig. 2.12. The average radius is encoded in the gray scale whereas larger radii appear brighter and smaller radii appear darker. The active regions appear around the equator, i.e. at 90 degrees, and 270 degrees respectively. Although the plot shows artifacts like the apparent ripples around July 19, the synoptic view is a visualization of faculae[2] and sunspots as they appear on the solar limb.

Solar Oblateness

The solar disk has an oblateness of $\Delta r = r_{eq} - r_p \approx 8\,\mathrm{mas}$ (Sofia et al., 1994). The amplitude of this signal is therefore buried in the noise of the single radius measurements. However, averaging data with respect to position angles should make the solar oblateness apparent.

---

[2] Faculae are bright areas that are usually most easily seen near the limb of the solar disk.

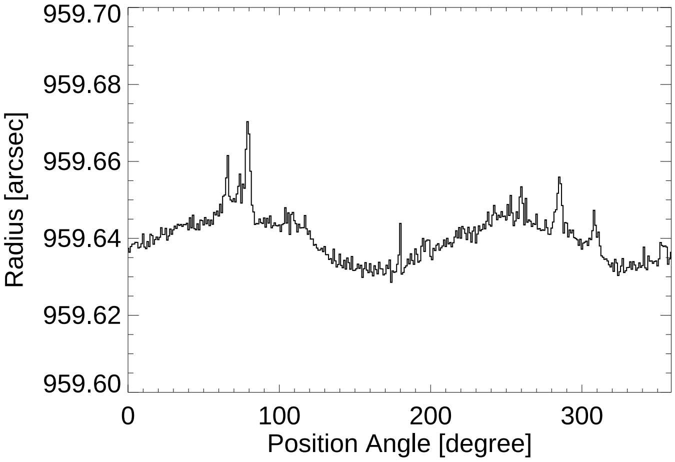

Figure 2.13: The binned radius measurements as function of position angle along the circumference of the solar disk show a modulation which is consistent with the solar oblateness. The excesses in the signal are mainly due to facular brightness.

Figure 2.13 shows a sum over 50 orbits of radius measurements. The measurements have been averaged in bins of 1 degree in position angle along the circumference of the solar disks. A modulation consistent with the solar oblateness can readily be seen, along with excesses due mainly to facular brightness. There are also artifacts present as well as noise at a level of about 2 mas (RMS) in the 1 degree bins.

Although the oblateness signal is of the order which has been observed earlier (Sofia et al., 1994), this result is preliminary and isn't correct for systematical errors.

Signal of Sunspot

As it has been demonstrated in Fig. 2.12, faculae and sunspots modulate the measurement of the solar radius as they turn around the solar limb. Whereas faculae appear in a temporary increase of the apparent radius, sunspots appear as a temporary depression of the apparent radius as they turn around the limb. This can be observed by averaging radius measurements around a position angle where a sunspot appears at the limb.

Figure 2.14 shows data of the east limb passage of NOAA active region 0397, observed at June 26, 2003, 00:30 UT. The top plot shows the averaged SAS radius measurements, while TRACE whitelight measurements are shown at the bottom. The map (bottom) shows limb latitudes from the equator to 20 degrees north, and the line plot (top) corresponds to 8 degrees north. The time resolution of the data is one RHESSI orbit, i.e. ≈ 96 minutes. The data essentially show excess brightness as apparent radius. There is plage and another smaller sunspot from AR 0399 following the appearance of the larger sunspot.

The limb positions are determined by fitting the position of the measured (averaged) apparent solar profile as described in section 2.1.6. To measure the radii as they are shown in Fig. 2.14 the same algorithm has been applied. Therefore, the sunspot appears as a relatively large depression in radius of about 0.8 arcsec. These photometric effects are convolved with the PSF (≈ 4.5 arcsec, FWHM). On the other hand, the "true" radius values are expected to be smaller (several tenths of arc seconds) due to the Wilson depression (Solanki, 2003, pp. 164). It

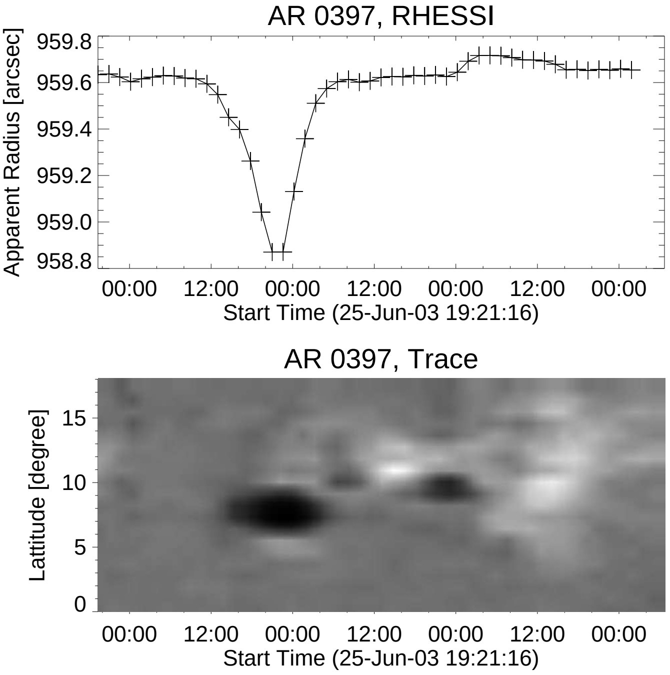

Figure 2.14: (Top) The averaged radius measurements at a position angle corresponding to 8 degrees latitude show a depression of the radius while a sunspot is turning around the east limb. (Bottom) For comparison, TRACE whitelight intensities are shown for 0 to 20 degrees latitudes at the east limb visualizing the sunspot turning onto the solar disk.

will be a challenge to distinguish photometric effects from true radius values.

2.2 Roll Angle System (RAS)

2.2.1 System Overview

The purpose of the RAS is to measure the instantaneous roll angle of the imager (the telescope) with respect to the telescope axis. Although the knowledge of the spin period together with the pointing information is sufficient for image reconstruction, knowledge of the absolute roll angle is necessary to determine the azimuthal position of the image. After giving a brief overview of the RAS, its design is described in more detail (section 2.2.2) and the statistics of the observed stars is discussed (section 2.2.3). The ground and the flight calibration is discussed in the sections 2.2.4 and 2.2.5. Finally, the off-line analysis of the RAS data is described in section 2.2.6.

The RAS is a star scanner pointing radially outwards with respect to the rotating spacecraft and observes stars within the field of view of 60 to 90 degrees in polar angle (the angle between the observed direction of a star and the telescope axis). Stars within the field of view are focused by a lens system. While the spacecraft is rotating, the images of the stars are traveling over a linear CCD array and are triggering one or several pixels. After identifying a star event with a cataloged star, its timing provides the momentary roll angle of the spacecraft. The plots in Fig. 2.15 illustrate the geometry in RHESSI-centric coordinate systems. Almost 2π of the sphere are covered by the Earth. At the moment the Earth is within the field of view of the RAS, the sensor can be as much as 1000 times saturated because of the earth albedo. The recovery from the bright earth albedo introduces an additional sensor dead time after rotating out of the earth albedo of up to 0.8 sec.

2.2.2 Design of Sensor System

While the spacecraft is rotating, stars within the field of view are focused through a commercial Leica Summilux lens system (f/1.4) with a focal length of 50 mm. The images of the stars travel over a linear CCD array (Dalsa IL-E1) and trigger one or several pixels. Even though the sensor is a TDI CCD (Time Delay and Integration CCD) with 2048×96 pixels with a pixel size of $13 \times 13\,\mu\mathrm{m}^2$, it is operated in a mode which makes it equivalent to a linear CCD with 2048 pixels with a size of $13 \times 1248\,\mu\mathrm{m}^2$ each. Thus, the field of view in roll angle is ≈ 1.4 degrees. Assuming a rotational speed of 15 rpm, the passage time of a star event is between 15.3 msec and 17.6 msec depending on the polar angle with respect to the rotation axis. The size of a pixel corresponds to 0.9 arcmin in polar angle.

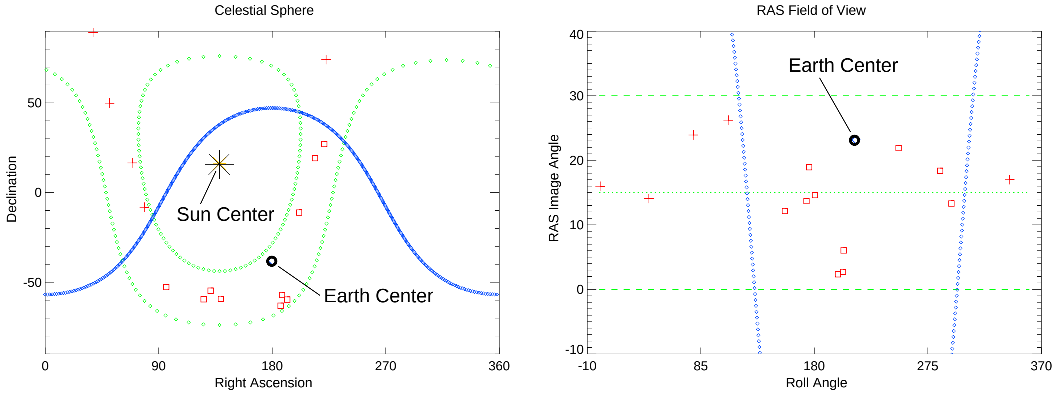

Figure 2.15: In the left plot, the celestial sphere seen from the spacecraft is shown at a particular time. The star indicates the position of the Sun and the circle indicates the position of the Earth. The concentric dotted lines 'around' the sun position mark the border of the FOV and the concentric line 'around' the Earth position marks the horizon. In the right plot, the same geometry is shown as seen by the RAS. Note that the Earth horizon corresponds to the almost vertically dotted lines. In both plots, the stars which are seen within a revolution are indicated by crosses and the stars which are in the FOV but hidden by the Earth are indicated by squares.

The combined system with the optics and the CCD has a spectral responsivity between 4000 Å and 10000 Å, with a maximum around 7000 Å. Thus, the sensitivity for a star detection depends strongly on its spectral type. The system is about twice as sensitive to M-class stars than to B-class stars. Although the integration time is programmable, the currently configured integration time is ≈ 8.8 msec corresponding to ≈ 47 arcmin in roll angle. For a star with visual magnitude m_V=3, this results in a response of 3.3 mV (≈ 7 channels) for a B0 star and 7.2 mV for a M0 star.

The performance of the RAS depends critically on its capability to trigger stars above a background level. Given the responsivity described above, the statistics of observing stars is described in section 2.2.3. In order to trigger enough stars, the sensor needs to have a stable dark level with low noise. This is achieved by shielding the optics from direct sunlight and the earth albedo and by cooling the CCD to a stable temperature between about -20 and -10 degreeC. The optical system is protected against direct sunlight by the satellite instrument deck and against earth albedo by an optical baffle for a viewing angle of

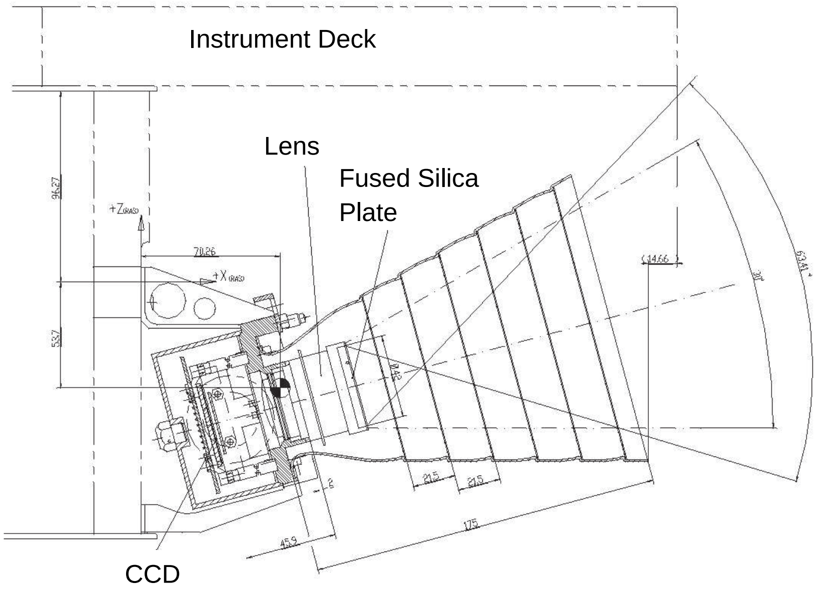

Figure 2.16: RAS schematics with baffle.

± 32 degrees in polar angle and ± 20 degrees in roll angle. The optimized baffle[3] shown in Fig. 2.16 suppresses light from off-axis angles to a required factor of about 5×10^{-7}. The front vane, the bottom third of the baffle cone, and the bottom RAS electronic box are covered by silver-coated Teflon foil to improve the radiative cooling in space, while a heater helps stabilizing the temperature (see also Zehnder et al., 2003; Henneck et al., 1999b).

The front-end electronics with the first-level FPGA are very similar to that of the SAS with the difference that the cycle time is the same as the integration time. This means that the CCD is always integrating light. The integrated charge is shifted out through the CCD shifter and digitized on a 12 bit ADC providing a resolution of 0.5 mV/channel. A double sampling and subsequent subtraction essentially eliminates the reset noise as described in section 2.1.2. The timing for

---

[3] A detailed ray tracing analysis and the optimization of the baffle design was performed by Retocon GmbH, Switzerland. The analysis showed that the knife-edge of the first vane is more critical than the reflectivity of the inside of the baffle. Consequently, the edges of the vanes has been sharpened to about 20 μm. On the other hand, a special absorptive coating of the baffle inside would have absorbed only about 30 % more than the used carbon-fibre structure, which showed a solar reflectivity of about 0.06.

Figure 2.17: The picture shows the RAS before integration with the spacecraft.

shifting the signals is the same as for the SAS. Besides the normal operational mode, several test and diagnostic modes (first-level modes) are implemented in the front-end FPGA.

As with the SAS subsystem, the RAS data are processed first by a hardware program in the second-level FPGA in the ADP and then by software running on the DSP processor. In Section 2.3 an overview of the ADP hardware and software is given. Nevertheless, the RAS relevant part of the second-level FPGA is described in the following two paragraphs.

At the same time as the data are flowing through the second-level FPGA logic, the addresses for all pixel values exceeding their individually programmable threshold values are stored. It has been shown by Fivian et al. (2003a), that a threshold of about 5 channels above the dark signal is marginal to trigger at least one star for every revolution of the spacecraft. Therefore, a pixel summation algorithm has been implemented in order to increase the signal to noise ratio. The FWHM of the point spread function is ≈ 2.6 pixels as pointed out by Zehnder et al. (2003) and Fivian et al. (2003a). Thus a summation of two adjacent pixels combined with an adjusted threshold level provides an increase of a signal to noise of almost $\sqrt{2}$. Another factor of almost $\sqrt{2}$ can be gained by summing two temporal consecutive values of the same pixel number since the passage time of an event is almost double the integration time.

The low altitude orbit of RHESSI implies that almost 2π of the celestial sphere is covered by the Earth. The signal induced by the Earth albedo can reach a level of 1000 times the saturation level of the RAS. Many CCD chips provide an anti-blooming feature, i.e. an internal chip capability to let the extra charge flow through an additional gate. However, the selected CCD in the RAS does not have that feature and therefore an extra mechanism had to be implemented. On the first-level FPGA, a programmable earth albedo threshold is set. If 64 pixels of a CCD readout are above this threshold value, the sensor is switched to maximum cadency of $\approx 2.2\,$msec per cycle and once the readout level is below the threshold again, the sensor is kept in this fast readout mode for a programmable additional time before being switched back to normal mode. This results in an additional blind time after rotating out of the Earth albedo of up to 0.8 sec. Nevertheless, the flight data shows a change of the dark signal of several channels for many configurations of the Earth albedo with respect to the spacecraft. This causes many false trigger events which can be removed with the analysis software (see section 2.2.6).

2.2.3 Star Observation Statistics

The accuracy required for the roll angle determination can only be achieved if a sufficient number of stars per revolution are observed. Therefore, extensive modeling of the star observation capability was done based on the Hipparcos input star catalogue. The model contains all necessary elements for the orbit (to be conservative: 38 inclination, 500 km altitude and a 50 km high opaque 'atmosphere', variable right ascension of the ascending node) and for all relevant celestial objects over the year 2001. The Earth occultation is calculated based on the detailed baffle geometry and a conservative afterglow dead time of 0.8 s has been assumed. The point spread function of a star image has been taken from our calibration measurements as $\approx 1\,$pixel (rms), independent of angle, while for lens vignetting the prediction from Leica has been used. The result of the calculation is expressed as fractional blind time, i.e. the number of RHESSI revolutions with no star detected divided by the total number of revolutions, as a function of the threshold. Only those parts of the full orbit were considered when RHESSI is in direct sun light. The curves shown in Fig. 2.18 represent an upper limit, since the envelope for all curves has been taken by varying the right ascension of the ascending node over 360 degrees. Although, the dependency of the fractional blind time from the momentary right ascension of the ascending node is fairly small, the effective value depends on launch time and the precession of the orbit. The calculations were done for the case with no spatial summation (dashed curve) and with spatial summation over 2 adjacent pixels (solid line), demonstrating the considerable improvement, which can be gained by spatial summation. Given the

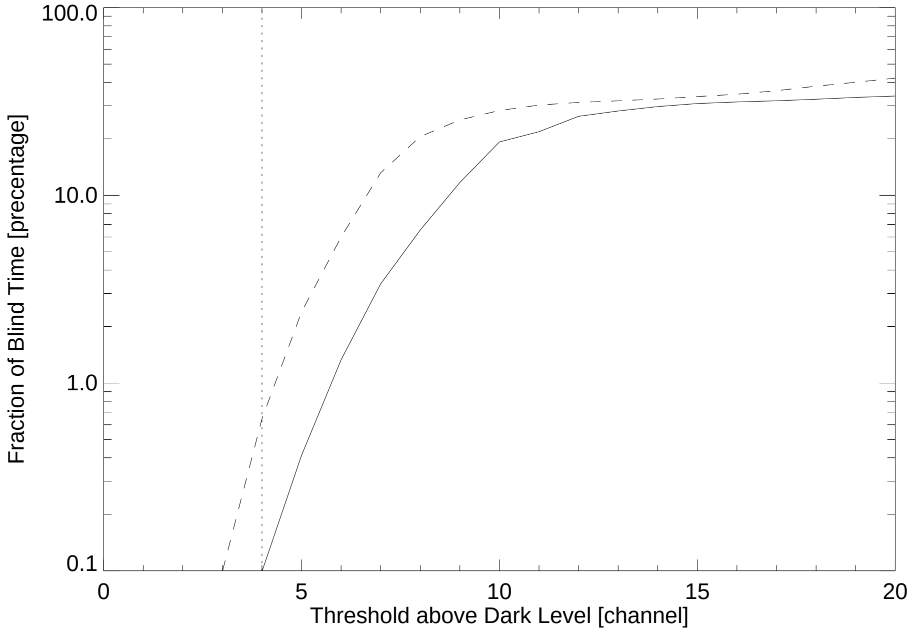

Figure 2.18: Fractional blind time versus threshold level for the year 2001. The dashed curve was obtained without spatial summation, the solid curve for spatial summation over 2 pixels. The vertical dotted line represents a reasonable threshold setting to be expected.

measured noise $\sigma_{rms} < 0.7$ ch and the requirement that the threshold be at least $5{\cdot}\sigma_{noise}$ above dark signal in order to limit the number of random noise events, a reasonable choice for the threshold is about 4 ch. This results in a fractional blind time of about 0.1% (solid line) or 0.7% (dashed curve). Summation over three adjacent pixels yielded a marginal improvement.

2.2.4 Ground calibration

For on-ground calibration, the fully assembled flight model of the RAS has been taken to Jungfraujoch, Switzerland, at an altitude of 3500 m above sea level. This location has the potential of better atmospheric conditions combined with the beneficial side effect of convenient cooling of the CCD. The RAS was mounted on a horizontally rotating support and could be set to scan the sky continuously over about 50 degrees between two end switches. The scanning speed was 30 to 90% of the nominal rotational speed due to mechanical limitations, resulting in a star passage at 35 degrees elevation between 21 ms and 65 ms. This corresponds to 4 to 9 time frames for an integration time of 8.8 ms. The elevation was adjusted manually and kept constant during a measurement. In order to get enough information for fitting of the point spread function, the number of pixels to the left and right of a triggered pixel was set to 10. To check on the stability of the dark signal, mixed event/image mode was implemented and the CCD temperature was constantly monitored and found to be stable between 0 and 5 degreeC.

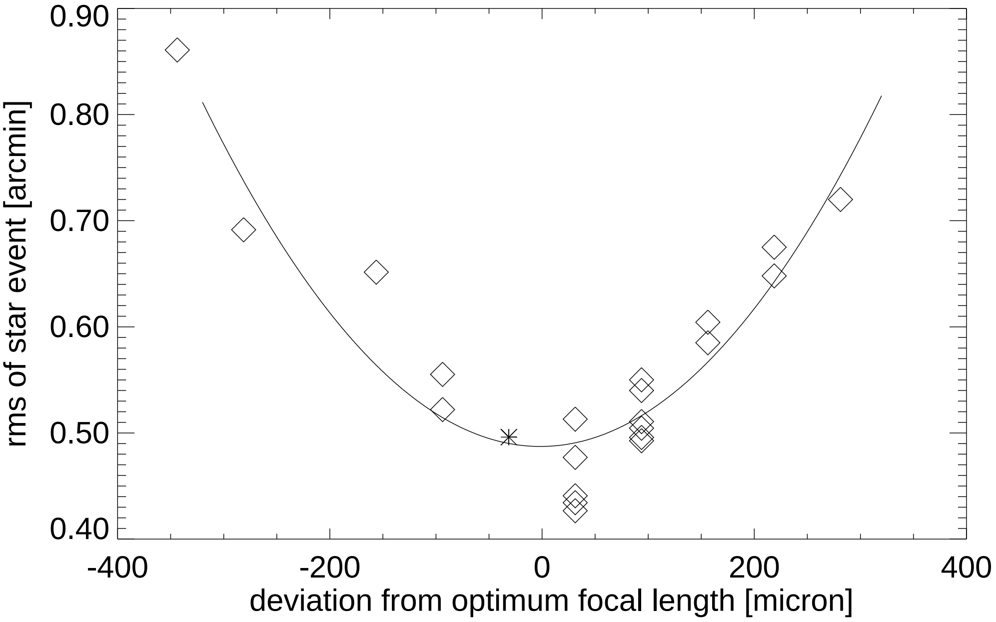

Figure 2.19: Fit for best focal length. The width of a star event has been measured for various distances of the CCD to the lens system. The quadratical fit of the data leads to the optimum focal length, at zero on the abscissa. The data point marked with an asterisk is a weighted mean for many data points which has been taken to estimate the dependency of the point spread on the off-axis angle.

In order to optimize the focus of the images, several stars with magnitude m_V ≈0 have been measured with various focal distances (distance between lens and CCD). Using an integration time of ≈9 ms, star events with at least three consecutive time bins have been taken only. After subtracting the previously measured background the dependency of the width of the star event on the focal length has been calculated (see Fig. 2.19). In order to have comparable results, each data point has been corrected for the appropriate off-axis angle using a guess for the dependency of the point spread on the yaw angle; the angle which corresponds to the position of a star event on the CCD. However, the fit for the best focal length shows very little dependency on this guess of the point spread. Optimizing the focal length, a point spread of ≈0.5 arcmin (rms) has been measured for an on-axis star event.

By calculating a theoretical response of the CCD, taking into account the spectral transmission of the optical system, the spectral response of the CCD and the spectral type and magnitude of the measured star, a response of star events of 75 to 100 % of the prediction has been observed.

It has been shown, that the focal length can be optimized for events along the optical axis to yield a point spread of < 1.2 arcmin (FWHM) but increasing to several arcmin for events at up to 15 degrees off-axis (Fivian et al., 2000). Nevertheless, the fully integrated flight model, which has a fixed focal length, showed a slightly different point spread function which has been found to be constant over the full field of view with a FWHM of 2.1 arcmin.

Star observations on the ground are hampered by atmospheric attenuation - loosely speaking clouds and haze - and by effects usually found in the literature under 'stellar scintillation' or 'twinkling'. The first effect produces a net reduction of the light intensity reaching the instrument while the latter may introduce an intensity spread as well as a wavelength re-distribution if one performs a series of independent measurements with short integration time (e.g. see Jakeman et al., 1978). Knowing the characteristics of all the elements of the RAS optics (Henneck et al., 1999b) and taking into account the spectral type of the different stars as well as the spectral responsivity of the CCD, the expected response for each star has been calculated. The measured response for many different objects with visual magnitudes between m_V=0 and m_V=3 agreed with the expectation and showed usually a signal of 75% to 100% of the expected value. An example of an especially low response of 60% is believed to be explained by clouds and haze, and an exception of a high response of 156% is believed to be explained due to an exceptionally big uncertainty in the fit of the response because of the very weak signal of the particular faint star with magnitude m_V=3.65. Thus, the critical sensitivity of the RAS has been confirmed.

2.2.5 Flight Calibration

The calibration of the RAS can be described using the following five calibration parameters:

1. orientation in polar angle

2. plate scale
3. slit orientation
4. responsivity
5. absolute roll orientation

The analysis of the flight data shows that the requirements for the accuracy of the roll solution can be achieved by using predicted responses of stars. Furthermore, the absolute roll orientation is discussed in section 2.4.3.

Since the purpose of the RAS is measuring the roll angle of the telescope, the reference coordinate system for the RAS is the same as for the SAS. A detailed definition of the reference coordinate system is given in Section 2.4.

In the following the calibration of the remaining three parameters is discussed.

Orientation in Polar Angle and Plate Scale

The polar angle of a star event is defined as the angle between the vector from the optical lens to the star and direction of the z-axis of the telescope-fixed imaging coordinate systems. The plate scale is the conversion factor between polar angle and pixel number on the CCD.

Every star event can be localized in pixel position on the CCD and any given calibration allows a calculation of the polar angle. Both calibration parameters, the orientation of the RAS in polar angle and the plate scale have a direct effect on this conversion. Thus, any time range with at least two stars with different polar angles can be used to solve a two dimensional minimization problem. In doing so, the square differences between the polar angle which is calculated from the cataloged star position and the measured polar angle are minimized.

Using calibrated parameters, the measured polar angles of star events show an excellent agreement with their prediction from the star catalog as demonstrated in Fig. 2.20. The standard deviation is typically of the order of 5-10 arcsec.

Slit Orientation

The slit orientation of the RAS is defined as the orientation of the CCD with respect to the optical axis of the lens system. A wrong calibration of the slit orientation results in a systematic offset in timing between stars of different polar angles. Therefore, minimizing the systematic offsets in timing leads to the correct calibration of the slit orientation.

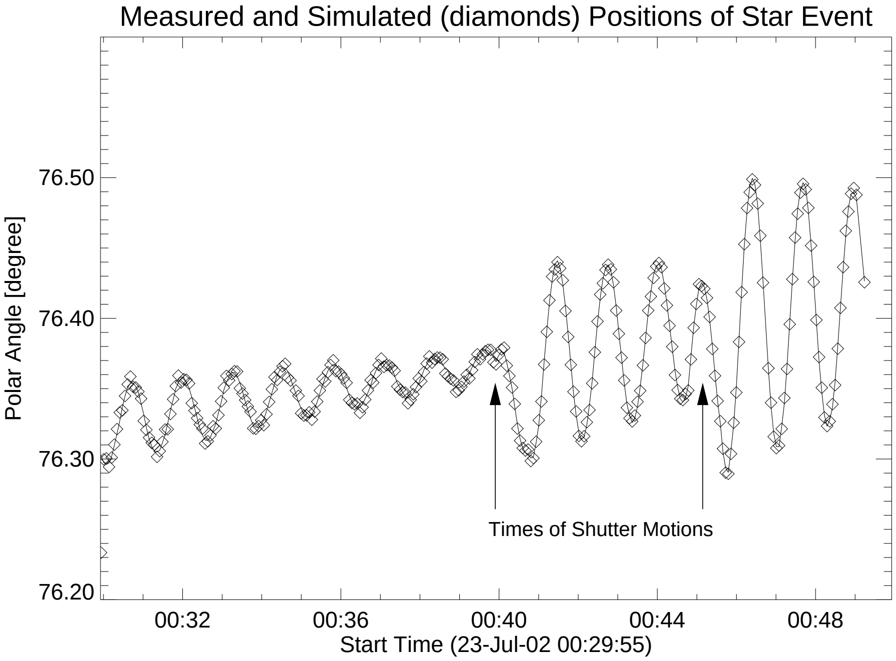

Figure 2.20: After calibration of the polar angle of the RAS, the plate scale, and the slit orientation, the measured polar angles of stars show an excellent agreement with their prediction according to the star catalog. Note: At the two indicated times, the shutter in front of the Ge-detectors changes its position resulting in a changed precession of the spacecraft.

The influence of the slit orientation on the measurement of the polar angle is only a cosine effect and can therefore be neglected.

2.2.6 Processing Flight Data

The flight data contain a much higher rate of randomly triggered false events than has been expected. Fig. 2.21 shows a maps of star events with raw data and with filtered (cleaned) data. This is a concern for two reasons. First, the aspect data processor needs extra CPU time to process those events and second, the on-ground data analysis requires a sophisticated filtering algorithm.

As has been pointed out in section 2.2.3, the triggering threshold for RAS events has to be at $\approx 5{\cdot}\sigma_{noise}$ in order to be sensitive enough. Setting the triggering threshold to a lower value would cause a significant increase of randomly triggered false events.

There are two more effects making the setup of the RAS instrument and the data analysis more difficult. The threshold level to trigger the earth albedo has to be set close to the dark signal in order to trigger all the various levels of earth albedo. On the other hand, the overall level of the dark signal seems to be raised by several channels for a considerably long time after the sensor recovers from the earth albedo and also before rotating into the earth albedo. Those effects together cause the much higher false trigger rate in the flight data than has been expected, and therefore a sophisticated cleaning algorithm is required. The cleaned events must satisfy the following criteria:

1. The passage time of a star image over the CCD is between 15.3 and 17.6 ms (at 15 RPM) whereas the sampling time is ≈ 8.8 ms. Therefore, a star event should trigger pixels at 2 or 3 time frames consecutive in time, but never at more than 3. (The expression *time frame* refers to a full CCD readout of one integration time.)
2. The time frame with the largest amplitude defines the response of the star. The star light for the full 8.8 ms integration time must illuminate the CCD, since the integration time is less than 1/2 of the passage time. This is made evident in section 2.4.2, and by Fig. 2.29 respectively.
3. Star events should have more than one pixel above threshold since the point spread function of the RAS is about 2 pixels (FWHM).
4. The amplitude of a star should match the calculated amplitude.
5. The star signal should be repetitive with the spin period of the spacecraft.
6. The phase and pixel position should correspond to a real star.

Filtering of the Data and Identifying Stars

In order to separate the real star events from the often quite numerous false triggers, the implementation of the following steps has proven to be sufficient:

1. The events are grouped according to the number of consecutive time frames, i.e. all events not preceded or followed by another time frame, all events with 2 consecutive time frames, and so on. Ideally the real star events have 2 and 3 time consecutive frames. However, faint stars producing weaker signals may trigger only one time frame.

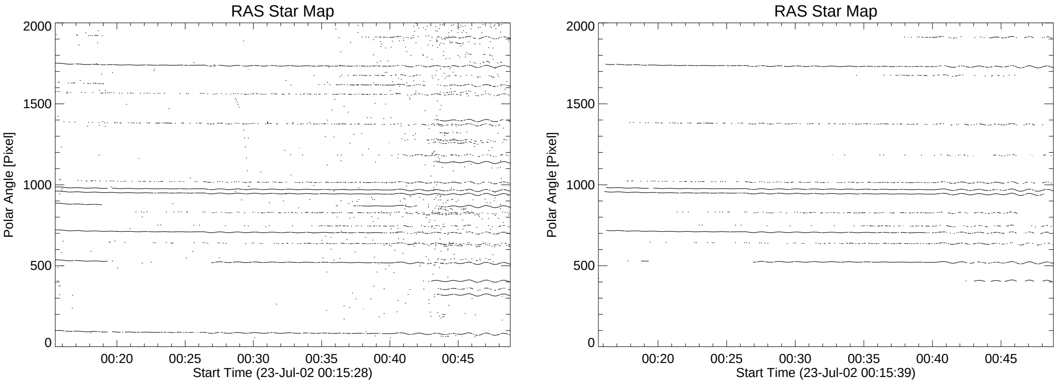

Figure 2.21: (Left) The raw, or un-cleaned, map of events shows fitted pixels positions of events vs. time. (Right) The map has been clean and only events satisfying the criteria for a star event remain.

2. For each star event and time frame, a Gaussian plus a constant is fitted to the pixel values. This determines the pixel position of the event, the amplitude, and the background level. The background level is mostly defined by the adjacent pixels below threshold which are also included in the data stream (currently 3 pixels on either side).

3. The maximum amplitude of a grouped star event (from 1, 2, or 3 time frames) is defined to be the amplitude of the group of star events.

4. The fraction of the RAS time of the events modulo the spin period of the spacecraft must be constant for a constant, unknown spin period. This fraction corresponds to the roll angle. The period is varied until the fraction is constant within a predefined time interval (order of minutes).

To illustrate the reconstruction of the roll angle, ≈ 30 minutes of data taken during the X-class flare on July 23, 2002, at 00:25:09UT has been analyzed. In a first step, the data has been reduced as explained above and Fig. 2.21 shows the cleaned map of star events. These stars have to match stars in the field of view of the RAS with a given response. In order to select the candidates from the catalog, it's assumed that the imaging axis of the telescope is pointing at the Sun, a possible occultation the by Earth is ignored, and the cataloged stars must have at least 80 % of the response of the faintest measured star. By minimizing the least square distance in polar angle, roll angle and response, the measured star events are identified with stars from the catalog as illustrated with Fig. 2.22.

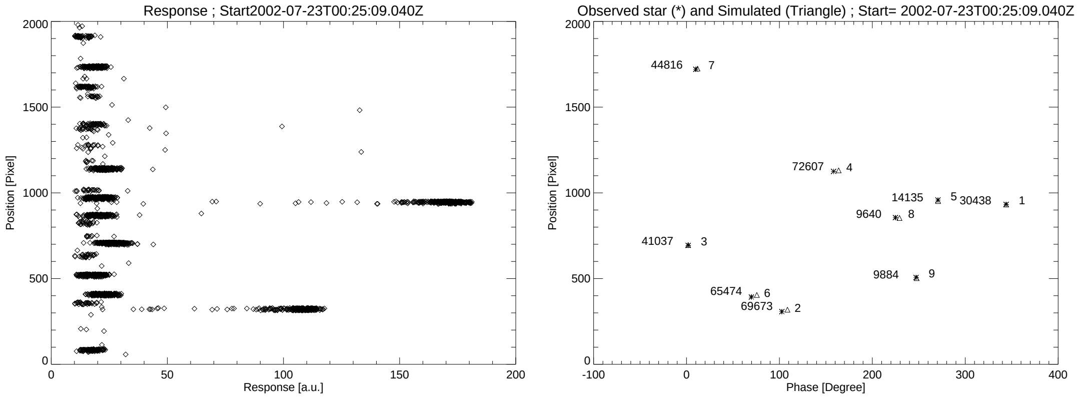

Figure 2.22: The left plot shows the response (x-axis) for every observed star event vs. the pixel position on the CCD. The right plot shows a map of observed events (asterisks) and predicted stars (triangles) in coordinates of pixel position and roll phase. To the left side on each mark the hipparcos run-number (identification of the cataloged stars) is printed.

Corrections and Smoothing

The agreement between the observation and the prediction is not perfect since the off-pointing from the sun center and some offsets in the alignment of the sensor is not anticipated at this point. After assigning every measured star event with a star from the catalog, the predicted position in polar angle (or pixel position) and roll angle can be corrected by using the pointing information measured by the SAS and by using the calibrated orientation of the CCD. The excellent agreement in polar angle has already been shown in Fig. 2.20.

In principle, every measured star event together with the assigned star and its location determines the instantaneous roll at that particular time. Considering the requirement of measuring the roll angle with an accuracy of 1 arcmin, the roll angle, measured as described above, shows a huge noise. In order to provide a smooth roll solution, the following smoothing algorithm has been implemented:

1. For the whole analysis time interval (typically 30 minutes, which corresponds to a half of the daytime portion of an orbit), a cubic polynomial is fitted to the roll angle as function of time.

2. For every star event, a straight line is fitted to the residuals of the cubic fit by considering all star events which are assigned to the same star within a

time interval of ± 60 seconds. The error of the pivoted star is then estimated to be the residual to the linear fit.

3. For the whole analysis time interval, a straight line is fitted to the roll angle of all star events weighing each star event by its estimated error.
4. The smoothed roll angle is calculated by fitting a straight line through the residuals of linear fit for all star events within a time interval of ± 60 seconds whereas each star event is weighted by its estimated error.

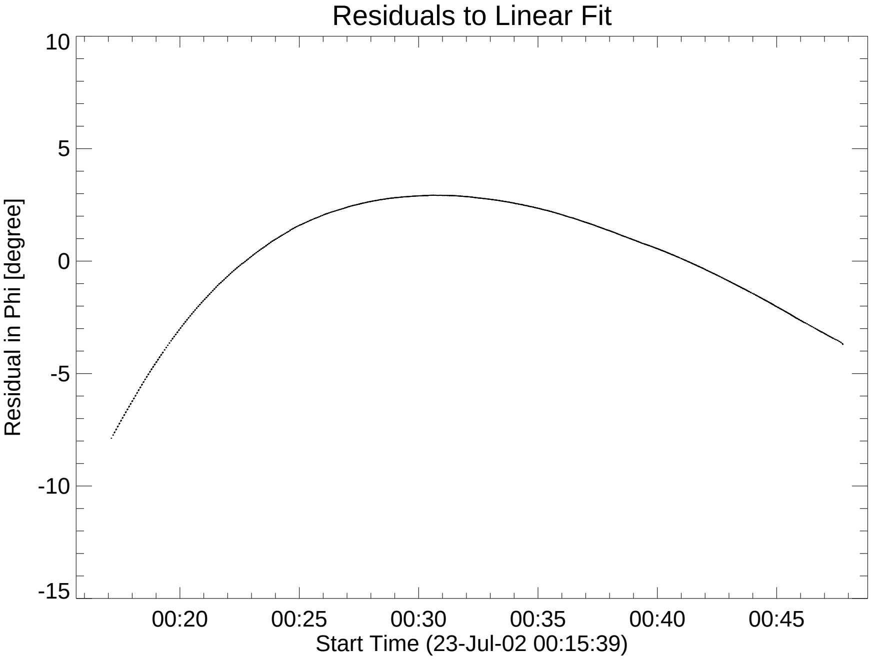

Figure 2.23: After correcting for geometrical effects and smoothing of the data, the residuals to a global linear fit demonstrate a smooth, unambiguous roll solution. These residuals as function of time demonstrate a continuous changes in spin period due to warm-up of the solar panel in sunlight.

The above algorithm takes care of big variations in the accuracy of faint and bright stars and the residuals to a final linear fit shown in Fig. 2.23 demonstrate a smooth and unambiguous roll solution. Furthermore, the statistics of the estimated error for every star event can be used to estimate the accuracy of the roll solution (see section 2.4.3).

2.3 Aspect Data Processor (ADP)

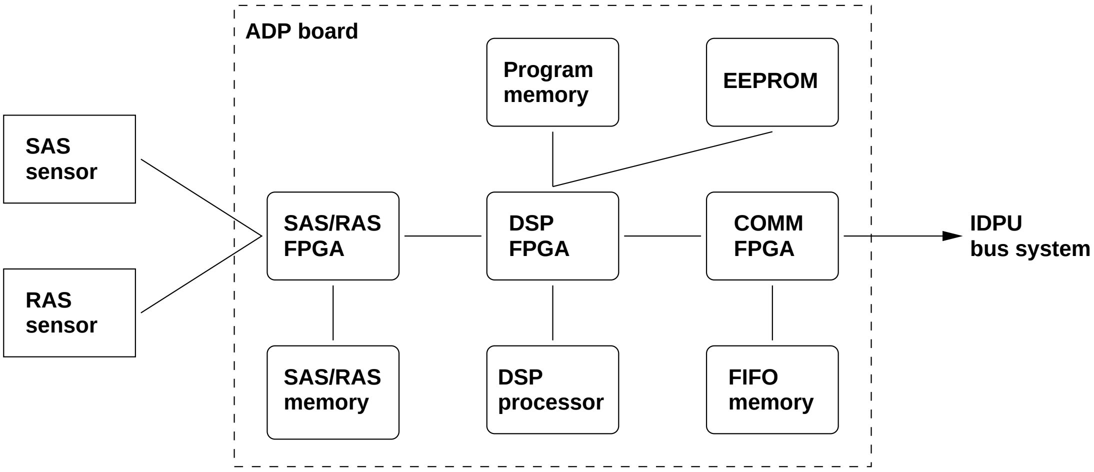

Figure 2.24: Simplified logical scheme of the Aspect Data Processor (ADP). For description and abbreviations see paragraph 2.3 in the text.

The Aspect Data Processor Board (ADP) is connected to the VME-like bus system in the Instrumental Data Processor Unit IDPU (see Curtis et al., 2002). It receives the signals from the aspect sensors, i.e. the three SAS sensors and the RAS sensor. On the ADP, the SAS/RAS signals reach the second-level SAS/RAS FPGA (Actel A14100) which stores all pixels in the SAS/RAS memory. Also, this FPGA processes the solar limbs and the star events and stores adequate information in the SAS/RAS memory. The DSP processor (Data Signal Processor, SMG320C50, 50MHz) of the ADP reads this data and after software processing and formatting telemetry packets are written to the FIFO (first-in-first-out) memory where the data is ready to be read by the IDPU data controller board through the VME bus system (see Fig. 2.24).

For the SAS, solar profiles (1d images) can be handled with either 10bit or 8bit (MSB) resolution. In the SAS/RAS FPGA the pixels of every image are compared to a programmable threshold value to detect the solar limbs. The limb addresses are read from the SAS/RAS memory by the DSP program and limb telemetry packets are written to the FIFO. In order to reduce the telemetry, the ADP can optionally divide the initial cadency of the sensor of 128 Hz by factors of 2 (128, 64, 32, 16 or 8 Hz).

For the RAS, every pixel of each image is compared with the corresponding value of the programmable threshold table by the SAS/RAS FPGA and the

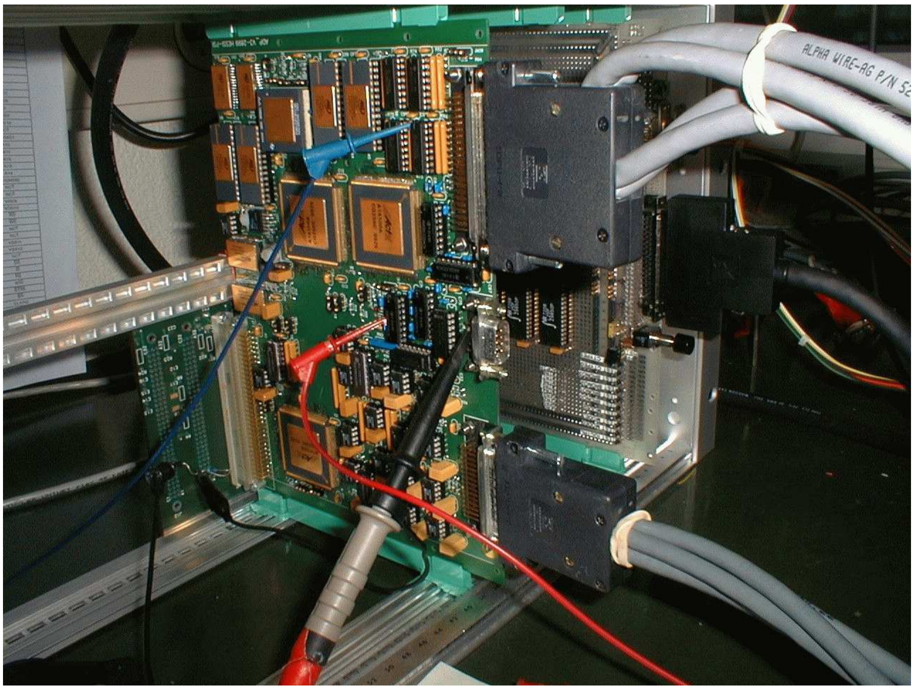

Figure 2.25: The picture shows the qualification model of the ADP connected to ground support equipment.

addresses for pixel values above threshold are written to the SAS/RAS memory. Since a star event can be spread over several pixels due to the point spread function of the lens system and to increase the signal to noise ratio, the pixel values for 2 to 4 adjacent pixels and two consecutive time bins can be added and then compared to the threshold value. The number of pixels to sum over can be programmed for five different regions of an image. The data in the SAS/RAS memory is then read by the DSP program and image and/or star event telemetry packets (always 10bit resolution) are written to the FIFO.

2.4 Reconstruction of the Aspect Solution

The telescope-fixed or spacecraft-fixed imaging coordinate system has been defined in such a way that any geometrical error has the least effect to the image reconstruction. Therefore, it has to be closely related to the features of the collimators and the SAS. The imaging z̃-axis or "Imaging Axis" is defined to be parallel to the line from the center of gravity of the CCD centers to the center of gravity of the optical centers of the lenses. The origin is the center of gravity of the CCD centers and the sense of the z̃-axis is positive toward the Sun. Furthermore, the x̃ and ỹ-axis are chosen to build a right-handed Cartesian coordinate system where the orientation of the ỹ-axis is basically arbitrary. However, the ỹ-axis is pointing approximately toward SAS10, the first SAS subsystem and is well defined with respect to the RAS defining the roll angle. Location and orientation of all features (the front and rear grids, the SAS, the RAS and the PMTRAS) have to be given in that coordinate system.

As indicated in section 1.2 and described in detail by Hurford et al. (2002), the pointing of the rotating spacecraft and the roll angle have to be known at any given time in order to reconstruct images. A set of a well-defined pointing and roll angles is defined as the aspect solution. Figure 2.26 shows an instantaneous relation between the solar limb with solar-fixed xy-coordinates and the projection of the imaging x̃ỹz̃-coordinate system onto the Sun. The direction of the imaging z̃-axis is marked as "Imaging Axis". The pointing P_{ASPECT} is defined to be the angle between the direction from the spacecraft toward the sun center and the imaging axis. Furthermore, the roll angle φ is defined as the angle between the solar fixed y-axis and the projection of the spacecraft fixed imaging ỹ-axis. The sign of the roll angle is defined to increase with time. Looking from the spacecraft toward the Sun, the spacecraft is rotating clockwise, and therefore, a positive roll angle is a rotation from the solar y-axis toward the rotating ỹ-axis as indicated in Figure 2.26.

Since the SAS is a part of the telescope mounted as close as possible to the grids, the solar pointing origins from the measurement of the position of the sun center in the body frame. This vector is the same as the vector P_{ASPECT} in Figure 2.26 with the opposite sign, but measured in the rotating x̃-ỹ imaging coordinate system. Let P_{SAS} be the direction of the sun center measured by the SAS and P_{ASPECT} the solar pointing of the telescope as defined earlier in this section, then the transformation is as follows:

$$\mathbf{P}_{ASPECT} = \begin{pmatrix} \cos\varphi & -\sin\varphi \\ -\sin\varphi & -\cos\varphi \end{pmatrix} \mathbf{P}_{SAS} \tag{2.2}$$

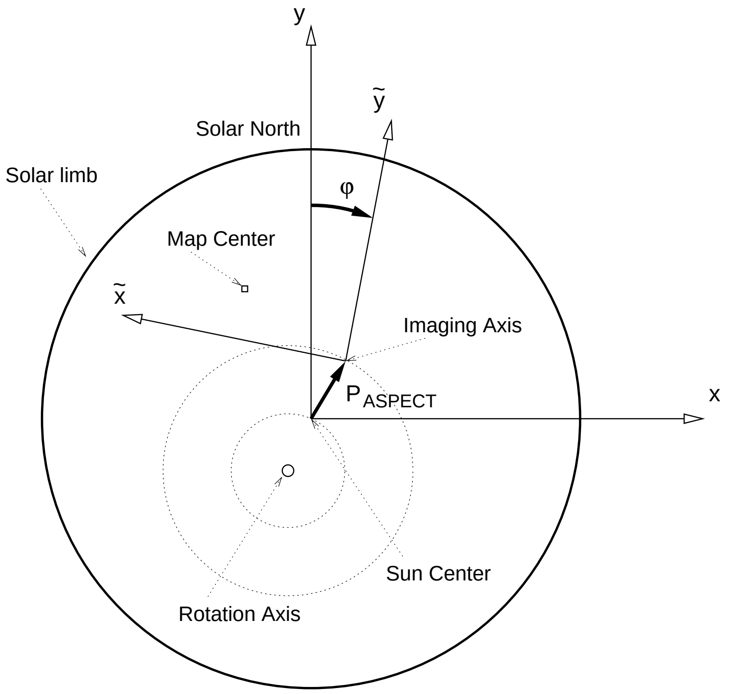

Figure 2.26: The solid circle represents the solar limb and the x-y coordinate system refers to solar coordinates with the y-axis pointing toward solar north. At a given time, the telescope axis may point at any point on this projection plane. That point is marked with "Imaging Axis" and the $\tilde{x}$-$\tilde{y}$ axis represents the spacecraft fixed coordinate system. The pointing of the spacecraft is defined as the angle between the sun center and the imaging axis and is represented by the vector $\mathbf{P}_{ASPECT}$. The roll angle φ is defined as the angle between the solar fixed y-axis and the projection of the spacecraft fixed $\tilde{y}$-axis.

where φ is the roll angle. The matrix of the inverse transformation is identical.

2.4.1 Solar Pointing

The transmitted data of each of the 6 solar limbs are processed off-line by the aspect reconstruction software which is integrated in the ground based RHESSI data analysis software (Schwartz et al., 2002). First the position on the CCDs for each limb is determined. For every given SAS cycle of transmitted solar limbs, the mid-perpendiculars to the straight lines between the two limb positions are constructed as shown schematically on the left part of Figure 2.27. In order to

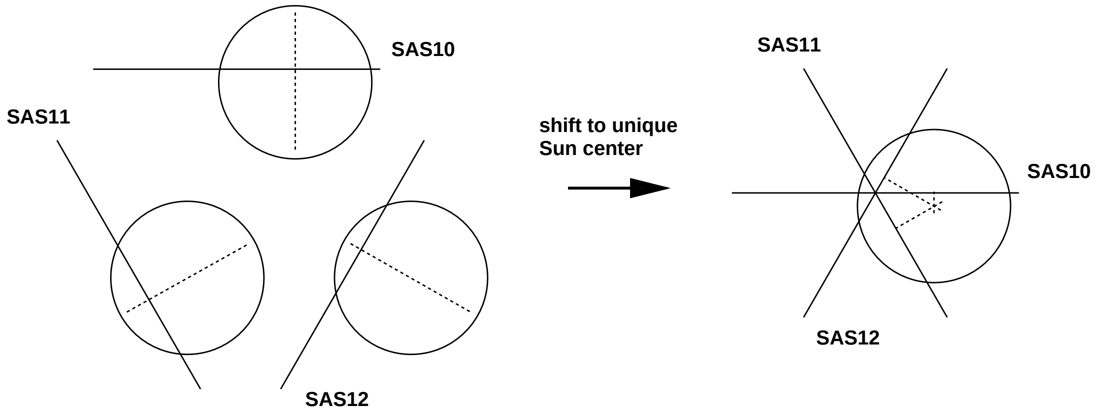

Figure 2.27: The CCD with the focused solar limb is shown for each subsystem on the left part of the schematic figure. Conceptually shifting the coordinates to share the point of the sun center leads to the reconstruction of the instantaneous sun center.

correlate the results from the three independent subsystems, conceptually the three systems are linearly shifted to share the point of the sun center as shown in the right side of Figure 2.27. For ideal circumstances the mid-perpendiculars would then intersect in one point; the instantaneous position of the sun center.

In general, the mid-perpendiculars form a residual triangle as indicated in Figure 2.7. The center of gravity of the triangle is the best estimate for the position of the sun center. Hence, the solar pointing for every SAS cycle is determined and a high cadence of measurements allows linear interpolation to determine the solar pointing for any given time. By using a quadratic interpolation, a nominal cadence of 16 Hz is sufficient (see section 2.4.3).

This reconstruction suffers from two main error sources. One is resulting from errors in the fit of the limb positions. If the fit of the limb positions had a systematic error, they would have the opposite sign for the positions of the two limbs on each of the CCD. However, by calculating the mid-point of the two limb positions, this error largely cancels. As pointed out later in this section, analysis of the flight data shows that a linear fit of the pixel values and a subsequent fixed thresholding is accurate enough (see also Fig. 2.28).

The second source of pointing errors is a consequence of dimensional uncertainties. Errors in the relative position and orientation of the three sub-systems induce errors in the reconstruction of the sun center. This can be well controlled by applying a self-calibration algorithm as described in detail in section 2.1.6 (see also Fivian et al., 2002). In Figure 2.7, the case with an error for only one subsystem is represented. For the general case with a remaining residual triangle,

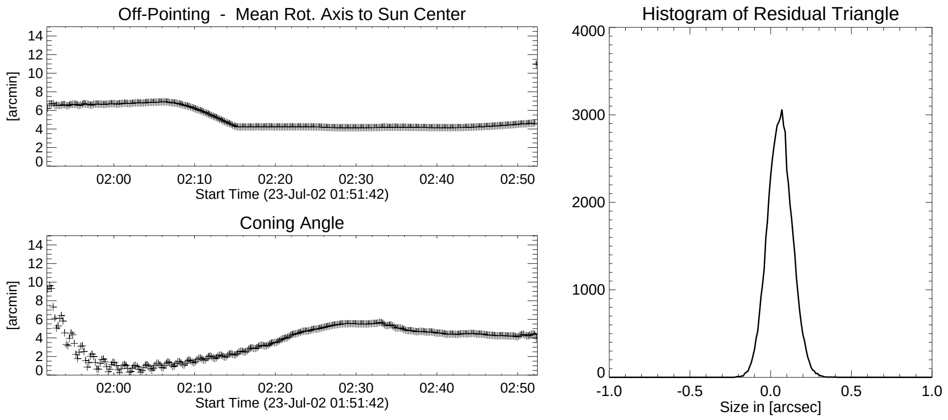

Figure 2.28: The plots show data for a typical orbit with the spacecraft being in direct sunlight. After sunrise, the spacecraft is pointed off the sun center by ≈ 7 arcmin and has a coning angle of ≈ 8 arcmin, i.e. the rotation axis differs from the imaging axis. The angular momentum applied by the torque rods induces a precession which can be seen as wiggles in the coning angle for about 20 minutes. The complicated dynamics of changing the off-pointing and coning angle by several arcmin is perfectly measured by the SAS, which is illustrated by plotting the histogram of the size of the residual triangle for the same time range. The mean of the characteristic size of the residual triangle is ≈ 0.06 arcsec and the width of the distribution corresponds to $\sigma \approx 0.08$ arcsec. An additional error induced by interpolating measured data points adds to the given value. (see Section 2.1.1)

the statistics of $1/\sqrt{3}$ of the length of the residual triangle or 2/3 of its height, can be taken as a measure for the accuracy and is defined as the relative pointing error.

Over the orbit, the spacecraft follows a relatively complex dynamics and Figure 2.28 shows the relevant pointing properties for a typical orbit. Here, the off-pointing is defined as the angle between the mean rotation axis and the sun center, and the coning angle is defined as the angle between the imaging axis (or SAS axis) and the instantaneous rotation axis. The spacecraft shows an off-pointing from the sun center of up to 7 arcmin and a coning angle of up to 8 arcmin. With the current calibration which is used for X-ray imaging, the systematic error of the relative pointing is ≈ 0.06 arcsec and the statistical error is in the order of $\sigma \approx 0.08$ arcsec.

The statistics of the size of the reduced triangle, as discussed above, confirms overall compliance with the requirement of measuring the pointing better than

0.4 arcsec. In section 2.4.3 an estimate of the pointing error for any given time is discussed.

2.4.2 Roll Angle

The basic RAS principle is to determine the momentary roll orientation of the spacecraft with respect to known stars. In the rotating plane the roll angle determination can be reduced to a time measurement. Every star event contains several pixel values from the same CCD readout. In a first step, a Gaussian with an additive constant is fitted to every star event. This determines the polar angle, the dark signal and the response of that particular event. The response depends on the brightness of the star, its spectral type and the fraction of the integration time the star illuminated the CCD. Since the integration time is about the half of the star passage time, a star event generates a response on more than one consecutive time frame as represented in Figure 2.29. Thus, the problem has been reduced to a precise determination of the timing of a star event and the identification of an event with a specific star.

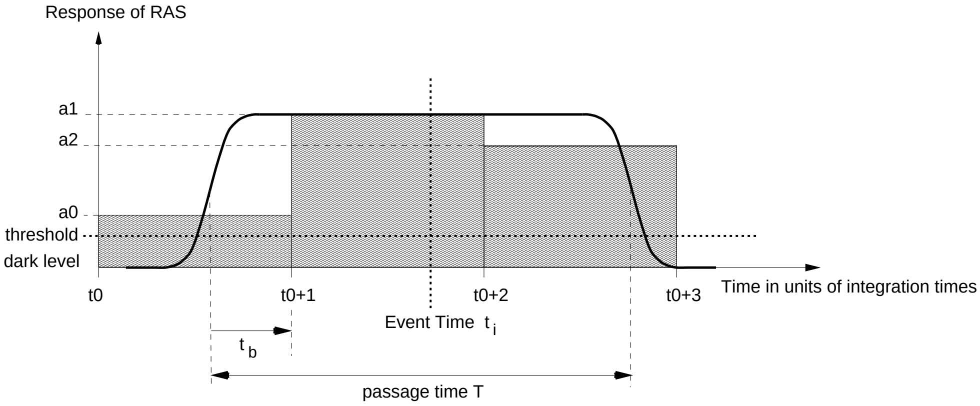

Figure 2.29: The solid line shows the response of the RAS CCD as a continuous function of time. Integration over a fixed time interval gives a histogram like function (shadowed rectangles) with values a_0, a_1 and a_2 for the integration cycles starting at t_0. After every integration time, the response level is compared to a threshold level for triggering the readout of the CCD pixels. The amplitudes a_i and the triggering time t_0 defines the temporal centroid t_i of the event.

Assume that the time dependency of the incident light for a star event can be treated as a function which is comparable to a rectangular shape. The width

(FWHM) of the point spread function of the RAS optics is ≈ 2 arcmin and at the rotational speed of 15 rpm this angle corresponds to ≈ 0.4 msec. Therefore, the convolution of the point spread parameterized in time with a rectangular function of the width of ≈ 15 msec passage time T gives a small enough rise time.

Hence, assuming the raise time of the signal on the CCD is small comparing to the integration time, the dark level is perfectly subtracted, and an event is triggering pixels for exactly three consecutive time frames, the timing of a star event can be described by the equation system

$$\begin{aligned} a_0 &= r \cdot t_b && (2.3)\\ a_1 &= r \cdot t_{int} && (2.4)\\ a_2 &= r \cdot (T - t_{int} - t_b)\,. && (2.5) \end{aligned}$$

This is made evident with Figure 2.29. For $i = 0, 1, 2$, a_i are the fitted responses for the particular time frames, r is the responsivity of the system, t_b is the time from the entry of the star into the field of view until the start of the next integration time, T is the passage time of a star event and t_{int} is the integration time. With a fully calibrated system and an identified star event, the equation system over-defines the only unknown t_b. The event time for that particular event is then $t_i = t_0 + t_{int} - t_b + T/2$.

The measured responses a_0, a_1 and a_2 have noise. Assuming that a_0 and a_2 have the same accuracy, t_b can be calculated in a symmetric way according to equation 2.6 and the responsivity r can be calibrated by the statistics from many stars using $\mathrm{r}=\mathrm{a}_1/\mathrm{t}_{int}$.

$$t_b = \frac{1}{2}\left(\frac{a_0 - a_2}{r} + T - t_{int}\right). \tag{2.6}$$

In order to achieve an accurate enough timing using equation 2.6, the responsivity r has to be well calibrated and the passage time T has to be known. Since the responsivity depends on the star, it is basically unknown until the star has been identified, but the sum of the equations 2.3 to 2.5 gives an initial estimate using $r = (a0 + a1 + a2)/T$ leading to a timing according to equation 2.7:

$$t_b = \frac{1}{2}\left(\left(\frac{a_0 - a_2}{a_0 + a_1 + a_2} + 1\right) T - t_{int}\right). \tag{2.7}$$

On the other hand, the passage time T is initially unknown and it has to be estimated using the statistics from a bigger number of star events. Once the responsivity and the passage time are estimated, the stars can be identified by comparing the timing, polar angle and the response with a star catalog. The RAS specific responsivity can be calibrated and stored in the star catalog too. Thus, after identifying the star events, the responsivity is known and the estimate of the passage time can be improved with

$$T = \frac{a_0 + a_1 + a_2}{r} \,. \tag{2.8}$$

Hence, the calculation of the timing has to be done twice; first to achieve good estimates in order to identify the star events, and second to result in an accurate timing.

For fainter stars, the response of the first and the last time frame might be too low to trigger RAS pixels. If only one of those is available, equation 2.6 can be used in an asymmetrical way with only a_0 or a_2. If a star event results in pixels for only one time frame starting at t_0, the best estimate for the timing is simply $t_i = t_0 + t_{int}/2$.

The data processing, in particular the identification of stars, is already discussed in section 2.2.6 and in section 2.4.3 an estimation of the error of the roll solution is given.

2.4.3 Estimated Error of Aspect Solution

Relative Pointing

It has been shown in section 2.4.1 that in general the measured pointing is better than 0.4 arcsec. Here, a model is presented which allows the estimation of the relative pointing error at any given time.

For any given time, the error can be expressed as a quadratic sum of errors of two independent sources,

$$\sigma^2 = \sigma^2_{data} + \sigma^2_{interpol} \,, \tag{2.9}$$

where σ_{data} is the estimated error of the measured data points and $\sigma_{interpol}$ is the estimated error of the interpolation between the data points. There is no direct measure of the error of a single data point. However, the statistics of the size of the reduced triangle can be used to estimate that error for any given time by averaging over a reasonably chosen time interval. It turns out that a box car average over five data points and a linear interpolation in time is a sensitive enough measure.

The pointing is nominally taken with a data rate of 16 Hz and quadratically interpolated in order to provide pointing information at any given time. This interpolation introduces an additional error which has been estimated by

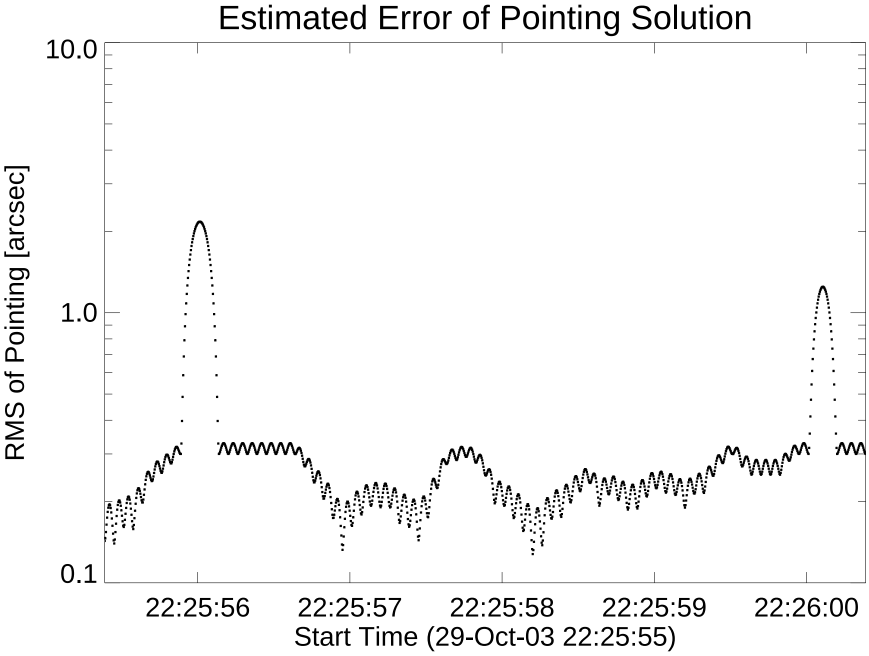

Figure 2.30: The plotted estimated error of the pointing solution for this specific time interval shows a typical error for the half-rotation between 22:25:57 and 22:25:59 UT, whereas the increase in error at 22:25:56 and 22:26:00 UT is due to data gaps and subsequent longer time range of interpolating of the data.

simulations. The maximum of this error occurs in the middle of a time interval between measured data points. The simulations show that it can be described by $\sigma_{max} = 34.4 \cdot \Delta t^2$. The interpolation error can then be quadratically interpolated for every interval of measured data points by

$$\sigma_{interpol} = 4 \left[\frac{t_{rel}}{\Delta t} - \left(\frac{t_{rel}}{\Delta t} \right)^2 \right] \cdot \sigma_{max} \ , \tag{2.10}$$

where Δt is the length of the interval and t_{rel} is the time relative to the beginning of that particular time interval.

Figure 2.30 shows the estimated error of the pointing solution for a particular time interval of 4 second on October 29, 2003. The local minima occurring at 16 Hz are at times of measured data points and the increase of the error in between are due to the interpolation of the data points. Two sub-intervals at 22:25:56 and 22:26:00 UT, both with a duration of ≈ 0.2 seconds, show errors of up to 1 arcsec and more. During those intervals with data gaps, the solution has to be interpolated over a longer time range resulting in a larger error. Whereas the data shown in Fig. 2.30 is a realistic example, the vast majority of time intervals show estimated errors as for the half-rotation between 22:25:57 and 22:25:59 UT.

Absolute Pointing

The SAS is measuring the center of the solar disk with respect to a spacecraft-fixed coordinate system which is defined by features of the system itself. The pointing is therefore always a relative measurement and no further calibration is required. However, the knowledge of the co-alignment of the SAS and the grids is essential for image reconstruction. The relative roll orientation can easily be derived from ground-based geometrical measurements. For the calibration of the relative phases of the grids, the following procedures are feasible:

1. Measurement of geometry on ground.
2. Self-calibration using flight data.
    (a) Maximize the contrast of the reconstructed map for an unresolved source.
    (b) The phases of the calibrated modulation must be the same for half-rotations.

In practice, method (2a) has been realized (Hurford et al., 2002).

Relative Roll Angle

In section 2.2.6 the error of every single star event has been estimated. The statistics of these errors is used to estimate the accuracy of the smoothed roll solution. For every star event, the roll solution at that particular time is calculated using a linear regression by weighing each event by its estimated error. The error $E(t_j)$ of the roll solution at the time t_j of the star event with time t_j can therefore be expressed by

$$E(t_j)^2 = \sum_{t_j - 60\,sec \leq t_i}^{t_j + 60\,sec \geq t_i} \frac{\sigma^2(t_i)}{n-1}, \tag{2.11}$$

where $\sigma(t_i)$ is the estimated error for the star event at the time t_i and n is the number of star events within this particular time interval of ± 60 seconds.

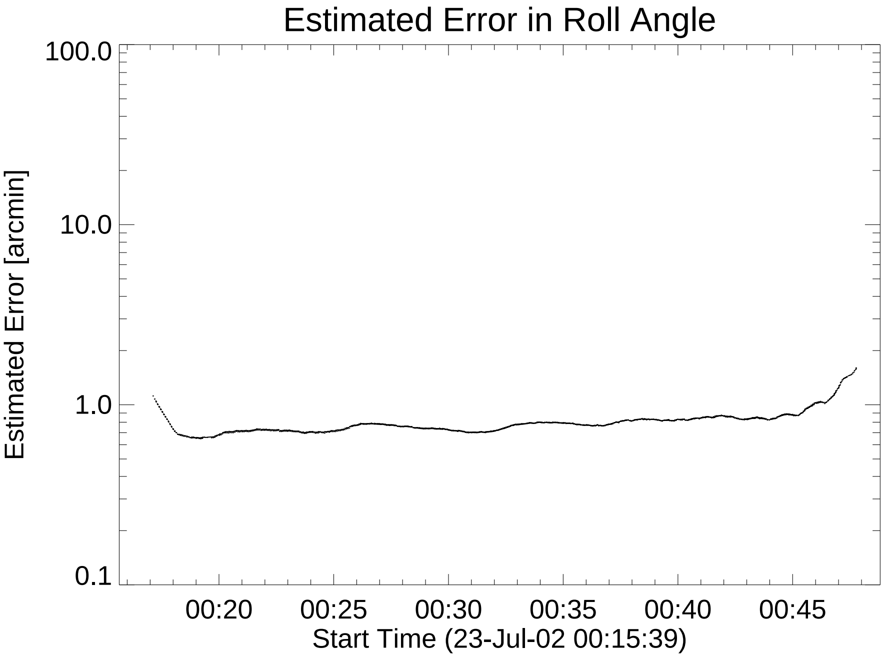

Figure 2.31: The estimated error (rms) of the roll solution is shown for a 30 minute time interval during the X-flare on July 23, 2002. It satisfies the requirement of an error to be smaller than 1 arcmin. The increase in error at the boundaries of the interval is due to a poorer statistics at the boundaries.

Figure 2.31 shows a graph of estimated errors for a time interval of 30 minutes during the X-flare on July 23, 2002. The roll solution satisfies the requirements of measuring the roll better than 1 arcmin (rms). The slight increase in error close to the boundaries of the analysis time interval is due to the poorer statistics of star events within the sub-intervals chosen for smoothing (see 2.2.6). This isn't a concern since the time interval for the roll solution can always be chosen to be bigger than the analysis time interval for imaging.

Absolute Roll Angle

For both systems, the CCD-RAS (section 2.2) and the PMT-RAS (described by Hurford and Curtis, 2002), the absolute roll angle has been calibrated on ground to the order of 1 arcmin. For this purpose, an LED has been moved in front of the integrated CCD-RAS flight model and the response at the a reference polar angle was measured. By mechanically measuring the momentary location of the

LED with respect to the imager, a reference roll angle is reconstructed.

In-flight data measure a difference in the absolute roll angle of approximately 1 arcmin. An error in calibration of the absolute roll angle has only an effect on the rotational placement of the reconstructed map with respect to solar north. Knowledge of the absolute roll angle is therefore only important for comparisons with images at other wavelengths. While 1 arcmin in roll angle corresponds to 0.3 arcsec displacement on the limb, localizations of images at other wavelength have bigger errors.

Chapter 3

Motions of HXR Footpoint Sources

3.1 Introduction

Solar HXR bremsstrahlung from energetic electrons accelerated in the impulsive phase of a flare is observed to be primarily from the footpoints of magnetic loops (but also see Veronig and Brown, 2004). The mechanism that accelerates these particles is still not understood. Standard magnetic reconnection models predict increasing separation of the footpoints during the flare (e.g. Priest and Forbes, 2002) as longer and larger loops are produced.

If the reconnection process accelerates electrons (Øieroset et al., 2002), the HXR footpoints should show this motion. The motion is only apparent; it is due to the HXR emission shifting to footpoints of neighboring newly reconnected field lines. Hence, the speed of footpoint separation together with the magnetic field strength reflects the rate of magnetic reconnection.

The inflow of magnetic energy into the reconnection region can be expressed by the inflow of Poynting flux through the area of the reconnection region by writing the energy release rate H as

$$S = 2\,\frac{B_{corona}^2}{4\pi}\,v_{in}\,A_r\ , \tag{3.1}$$

where A_r is the area and v_{in} is the inflow velocity through this area (e.g. Isobe et al., 2002). Note that the factor 2 results from assuming symmetric inflow from both sides into the reconnection region.

The magnetic field in the corona, B_{corona}, and the inflow velocity, v_{in}, are very difficult to observe. More easily observable are the motion of the footpoints of the reconnected loops seen in HXR and the magnetic field at the photosphere. Using conservation of magnetic flux

$$B_{corona}\, v_{in} \;=\; B_{fp}\, v_{fp} \ , \tag{3.2}$$

the energy release rate can be written as

$$S = 2\, \frac{B_{corona}}{4\pi}\, B_{fp} v_{fp}\, A_r \ , \tag{3.3}$$

where B_{fp} is the magnetic field at the footpoints and and v_{fp} is the velocity of the footpoints. This is an upper limit for the energy deposition rate at the footpoints.

Assuming $B_{corona} \propto B_{fp}$ the product $B_{fp}^2 v_{fp}$ should therefore be roughly proportional to the energy deposition rate in the footpoints. For a constant slope of the non-thermal HXR spectrum and a constant magnetic field at the footpoints, v should be proportional to the total HXR emission from the footpoints.

Sakao et al. (1998) analyzed footpoint motions in 14 flares observed by Yohkoh HXT, but did not find a clear correlation between the footpoint separation speed and the HXR flux. Recently, however, source motion seen in Hα was studied by Qiu et al. (2002). They found some correlation with HXR flux during the main peak, but not before or after.

The spectral and spatial high resolution data from the RHESSI satellite provide a new access to this problem. The thermal and the non-thermal HXR emissions can clearly be separated and thus, an optimal energy range can be chosen in order to image the HXR sources. Furthermore, the spatial resolution of down to 2.3 arcsec allows a more precise localization of the footpoints than earlier observations.

First RHESSI results from Fletcher and Hudson (2002) analyzing several GOES M-class flares show systematic, but more complex footpoint motions than a simple flare model would predict. Krucker et al. (2003) investigated the HXR footpoint motion in the large γ-ray flare of July 23, 2003 finding that the footpoint on one ribbon moves systematically and the motion roughly correlates with the time variation seen in the HXR flux. This is consistent with magnetic reconnection if a higher rate of reconnection of field lines (resulting in a higher footpoint speed) produces more energetic electrons per unit time and therefore more HXR emission. The HXR emission of the second ribbon, however, shows several sources that do not seem to move systematically for more than half a minute, with different sources dominating at different times. This is inconsistent with simple reconnection models. It can be explained if the magnetic configuration is more complex and consecutively reconnected field lines have occasionally footpoints that are not located near each other but are separated by a few arcsecs resulting that the HXR emission appears to jump by the same amount.

In short duration flares (like 30 sec) the motion of the footpoints is difficult to observe since a velocity of 50 km/sec results in a displacement of only 2 arcsec. Therefore, flares with long lasting HXR emissions (>10 minutes) need to be investigated. Fletcher and Hudson (2002); Krucker et al. (2003) used the CLEAN algorithm for image reconstruction which requires an additional fit in order to determine the centroid of the HXR source.

A more logical approach is determining the footpoint locations using forward fit (Aschwanden et al., 2002) as used in this work. In contrast to Krucker et al. (2003) where the HXR flux is compared with the footpoint velocity, in this work the deposited energy is correlated with the footpoint separation in order to account for spectral changes. Furthermore, deriving the footpoint velocity from its time series of locations requires a numerical differentiation introducing additional noise to the data. The correlation between the deposited energy and the footpoint separation is presented using an integration over time in order to overcome these problems.

3.2 Overview of X-class Flare on March 18, 2003

The investigated flare occurred on March 18, 2003 at S15W46 (680 arcsec West and -160 arcsec South on the solar disk). It has a GOES class of X1.5 with a duration of ≈ 1 hour and an SXR peak around 12:05 UT. The RHESSI observation coverage was almost optimum with the spacecraft coming out of eclipse at about 11:56 UT and moving into SAA (South Atlantic Anomaly) at about 12:20 UT (see Fig. 3.1).

Figure 3.2 and Fig. 3.3 show the images of the TRACE 171 Å channel with RHESSI contours of reconstructed HXR images using the energy band from 35 keV to 80 keV and an integration time of 40 sec. The time series of the EUV images (compare Fig. 3.2 and Fig. 3.3) show a two-ribbon flare with the two ribbons (brightenings in EUV) moving apart during the flare. As more and more magnetic field lines are reconnected during the decay phase, an arcade of loops is formed across the ribbons showing hot plasma in EUV trapped by the magnetic field (see Fig. 3.3). The emission in the Fe IX and X lines require a temperature between 0.8 and $2{\cdot}10^6$ K.

During a part of the impulsive phase of the flare (11:54 to 12:03 UT) the HXR emission above 30 keV is contaminated by magnetospheric particle events

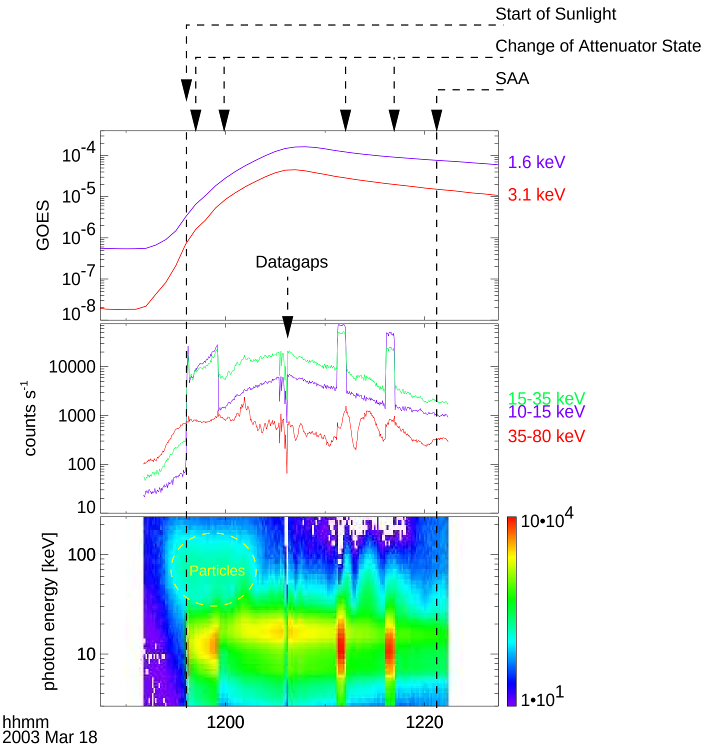

Figure 3.1: a) GOES SXR lightcurves. b) RHESSI count rates in three energy bands showing attenuator changes and datagaps. c) RHESSI spectrogram; note the magnetospheric particle events between 11:54 and 12:03 UT at 30-200 keV, and attenuator motions causing sharp flux changes.

as indicated in Fig.3.1c. This makes it difficult studying the impulsive and the early decay phase of the flare. However, using the PIXON algorithm and integrating over 40 sec allows imaging the HXR sources also during this time range showing the footpoints on the EUV ribbons (see Fig. 3.2).

Figure 3.1b shows the RHESSI lightcurves for three energy bands. After the first peak at about 12:02 UT, the long duration HXR emission in the highest energy band (35 keV to 80 keV) shows peaks later between 12:10 UT and 12:20 UT after the peak in SXR. The Neupert effect (see Neupert, 1968) doesn't hold in the later phase since at the times of those extreme variations in the HXR emission no increase is seen in the GOES SXR channels.

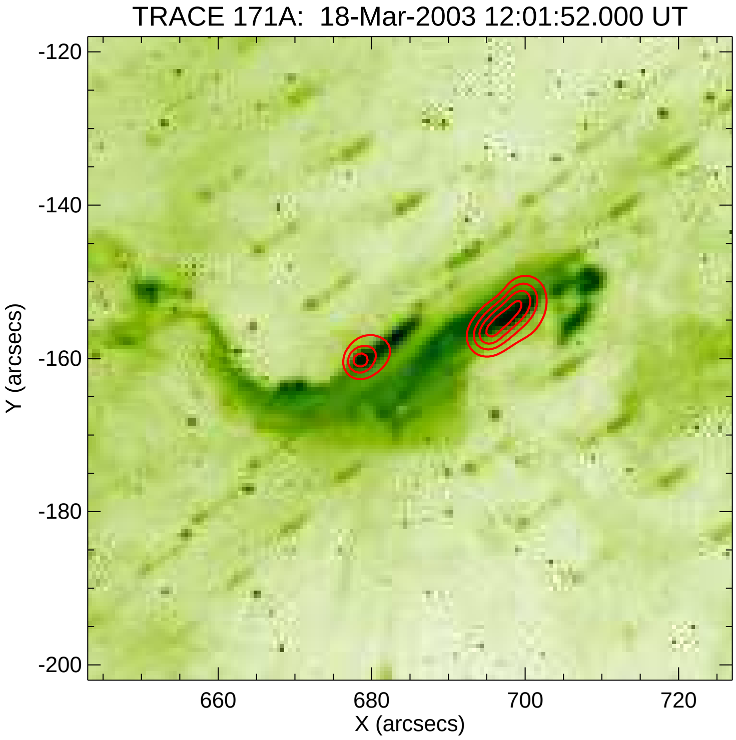

Figure 3.2: PIXON reconstructed contours of footpoint (35-80 keV) overlayed over a TRACE 171 Å image during the impulsive part of the flare. The two images are taken around the same time (12:01:52 UT) but with different integration times of 16.4 sec for the TRACE image and 57.2 sec (14 spin periods) for the RHESSI image. Contours shown are $30, 50, 70, 90\,\%$ of the maximum in the image. The RHESSI image is reconstructed using grid 1-7 given the maximum resolution of 2.3 arcsec (FWHM).

3.3 Data Analysis

In order to study the correlation discussed in 3.1 the data of the flare to be analyzed needs to meet some requirements. Even though the concept is of a more general nature, particular flares might show a far too complex geometry and the data might be too limiting.

Studying the location of the footpoints of a flare and their separation with time, the footpoints need to be well separated in space. Also, the energy range has to be chosen by which only the bremsstrahlung footpoints of the non-thermal electrons are imaged independent from thermal sources. There need to be exactly two footpoints which are spatially well separated and appear to be connected with

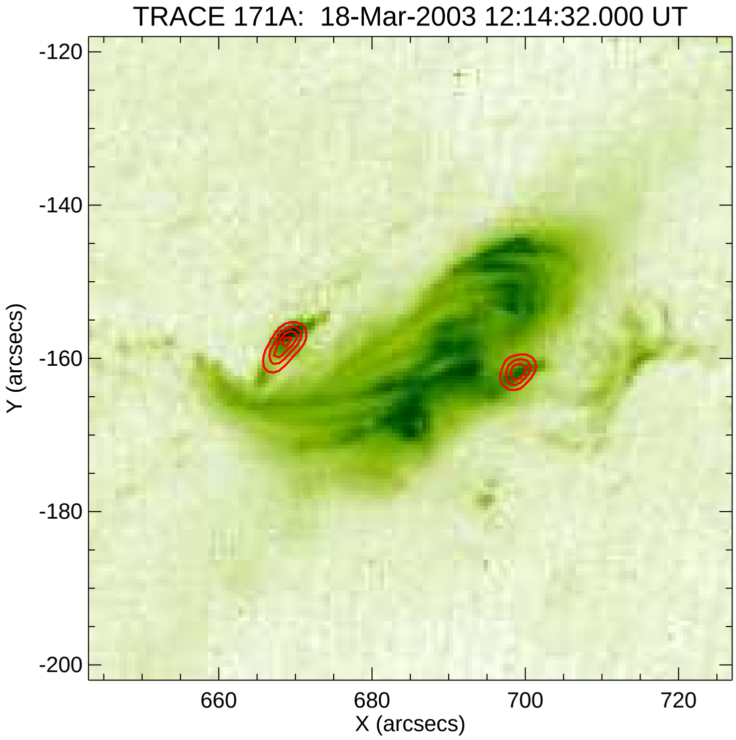

Figure 3.3: Same as Fig. 3.2 at 12:14:32 UT.

the same loop of magnetic field lines and thus correlate in time. Furthermore, the footpoints need to be prominent long enough to study time series, i.e. several minutes or longer.

For the full analysis time range, the spectrum needs to be fitted with a thermal and a non-thermal component. The deposited energy of the particles producing bremsstrahlung in the chromosphere at the location of the footpoints has to be determined. Therefore, the non-thermal component has to be fitted in the spectrum including a cutoff energy.

3.3.1 Deposited Energy (Spectroscopy)

Figure 3.4 shows a background subtracted photon spectrum of the analyzed flare around 12:09:04 UT. For the full analysis time range (12:06 to 12:22 UT), the photon spectrum can be reasonably well fitted with an isothermal component and a single power-law with a low-energy cutoff for the non-thermal component. There is no high-energy break in the power-law seen that would significantly

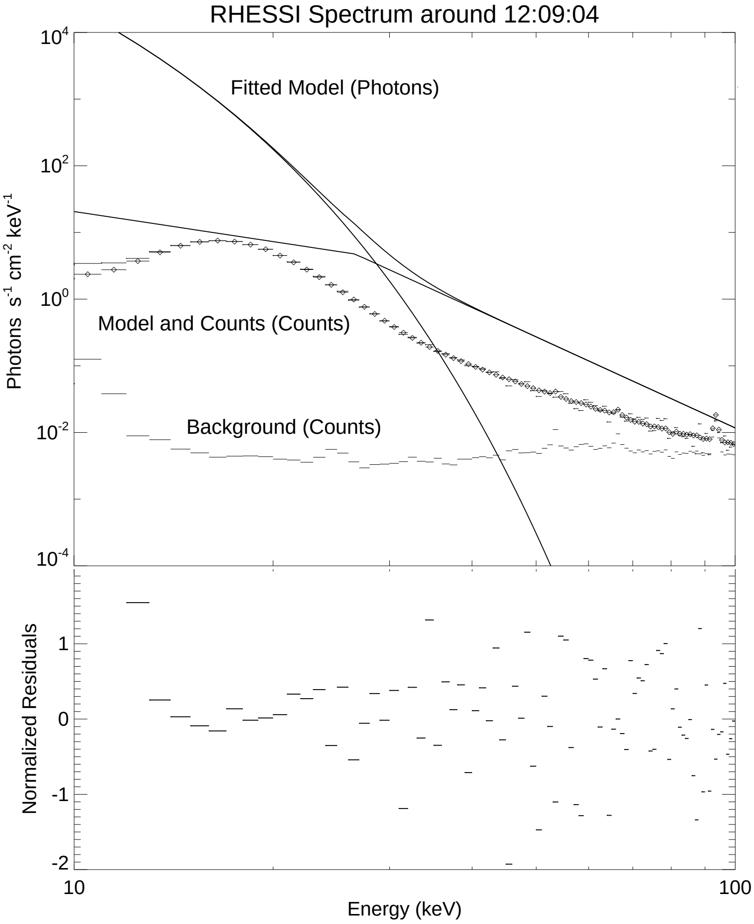

Figure 3.4: (Top) The fitted model in photon space, the background subtracted measured counts with the model in count space, and the background in count space. (Bottom) The normalized residuals of the fit between 15 and 80 keV are statistically well distributed.

change the total energy of the non-thermal source.

Except for two intervals (≈ 12:11 to 12:12 and 12:16 to 12:17 see Fig. 3.1) the spectrometer has been in attenuator state three with both attenuators in (see Smith et al., 2002a). While the total count rate is decreasing during the decay phase of the flare, the thick attenuator moved out for the two mentioned intervals and moved back in due to a still too high count rate. For those intervals, the count rate is very high (spin averaged livetime is down to ≈ 65 %) producing an amount of pileup which cannot be fully corrected by the present RHESSI analysis

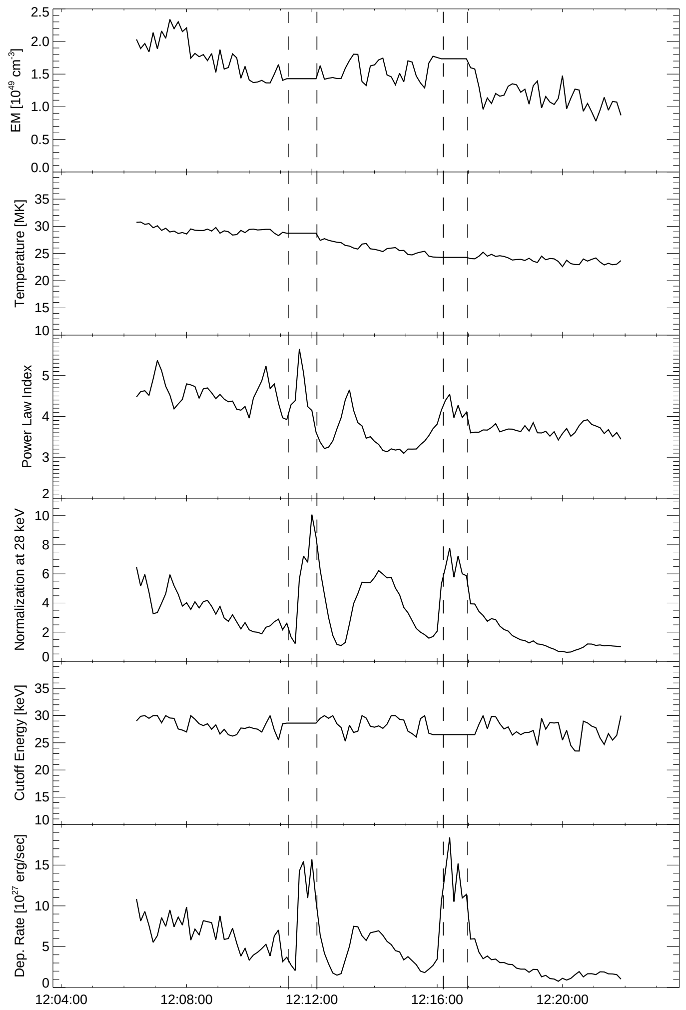

Figure 3.5: Time Series of the fitted parameters: a) Emission measure and b) temperature of the isothermal component, c) the power-law index, d) the normalization at 28 keV (the averaged cutoff energy) of the power-law, e) the cutoff energy in the photon spectrum, and f) calculated energy deposition rate of the non-thermal electrons in footpoints. The dashed lines indicate times of attenuator changes.

software. Nevertheless, the fit-parameters can be interpolated over these intervals (see below).

Figure 3.5 shows the time series of the fit-parameters together with the calculated energy deposition rate during the analysis time range. The vertical dashed lines mark the two intervals with attenuator state one, i.e. only thin attenuator in place. Over the analysis time range, the emission measure and the temperature of the thermal source seems to drop continuously with a decreasing temperature from ≈ 30 MK down to ≈ 23 MK. Thus, a linear interpolation for the two intervals with a high pileup is an evident approximation for the time series of these two parameters. Although those parameters are not needed for determining the energy deposition rate they need to be set appropriately in order to fit the power-law.

The fit of the cutoff energy in the photon spectrum is reasonably stable with values between 25 keV and 30 keV at about the energy of the cross-over of the thermal component and the non-thermal component. Therefore, interpolating the cutoff energy and fitting only the power-law index and the normalization during the two mentioned intervals with high pileup leads to smooth and self-consistent timeseries of the parameters for the non-thermal component of the spectrum.

Assuming that the non-thermal component of the photon spectrum is produced by electrons losing their energy primarily through Coulomb collisions on a thick target, the energy deposition rate can be estimated (see e.g. Lin et al., 2001; Saint-Hilaire and Benz, 2004). Time series of the calculated energy deposition rate is shown in the last panel in Fig. 3.5.

3.3.2 Footpoint Motion (Imaging)

The HXR emission at the footpoints appear rather as compact sources in contrast to expanded ribbons seen in EUV (see Fig. 3.3), although the HXR sources are still extended along the ribbons. As pointed out above, they are well separated. Therefore, forward-fitting an appropriate model seems to be the most effective method to determine the centroids of the two footpoints. Using the RHESSI analysis software (see Hurford et al., 2002; Aschwanden et al., 2002) two elliptical Gaussians have been fitted.

The spectrum above 35 keV is dominated by non-thermal sources as shown in Fig. 3.4. Thus, a time series of images has been fitted for the energy range from 35 keV to 100 keV using grids 3 to 8 (the resolution of grid 3 is 7 arcsec FWHM) and a pixel size of 1 arcsec To optimize time resolution and precision for the fitted footpoint locations, an integration time of 30 sec has been chosen.

Although the HXR flux peaks around 12:02 UT, no stable footpoint positions are found before 12:06 UT. This can be partly explained by a very high background flux above 30 keV produced locally around the spacecraft between 11:54 and 12:03 UT by magnetospheric particles making imaging more difficult. Using

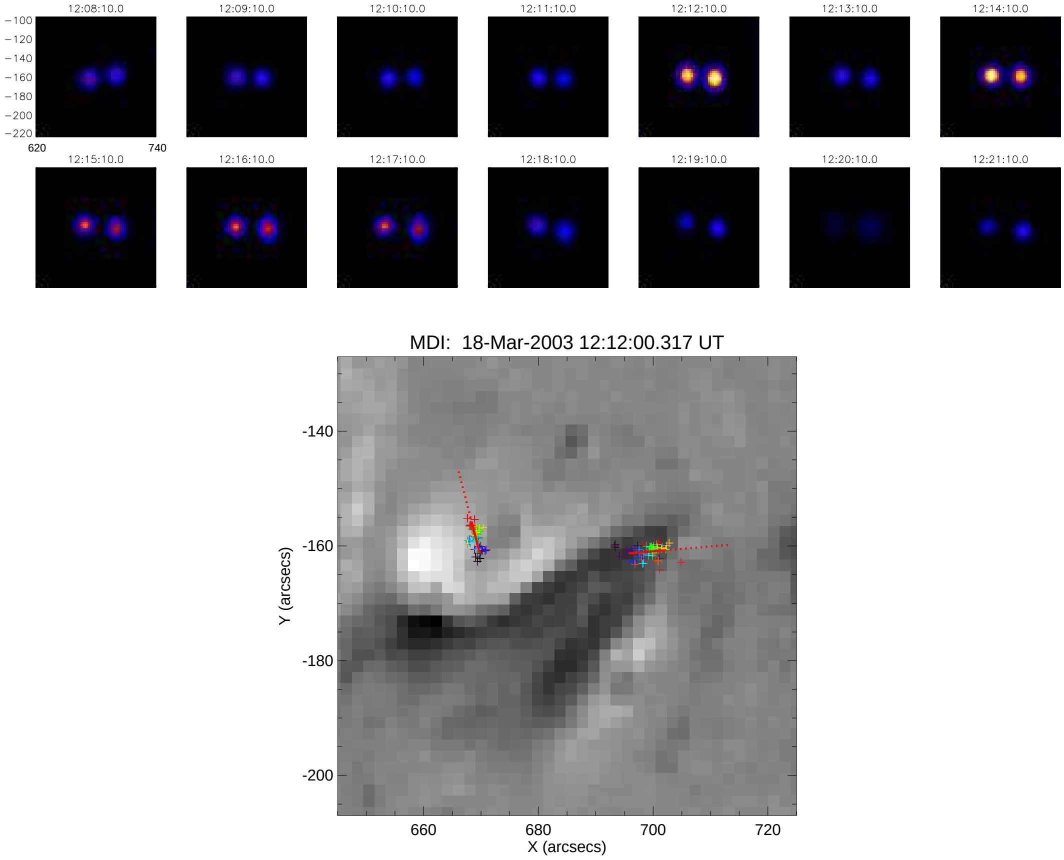

Figure 3.6: a) Time series of forward fitted images of footpoints (35-100 keV). Variations in intensity are partly artifacts from attenuator changes. b) Color coded footpoint positions overlayed over MDI magnetogram; blue is at 12:08 and red is at 12:20 UT.

the PIXON algorithm and integrating over the total duration if the first HXR peak, however, reveals the existence of HXR footpoint sources on the EUV ribbons also for this earlier times (see Fig. 3.2). As already mentioned in section 3.3.1, there are two intervals with a change of attenuator state and a subsequent increased pileup and detector dead time. No reliable locations could be fitted during these time ranges. In the lower part of Fig. 3.6 the footpoint locations are plotted over the MDI magnetogram where blue is assigned to earlier times in the color code. The footpoints seem to move away from apparent neutral line (line of sight measurement).

The fitted locations of the footpoints on the solar disk are projected onto the chromosphere applying a radius of 696,000 km and the distance between the

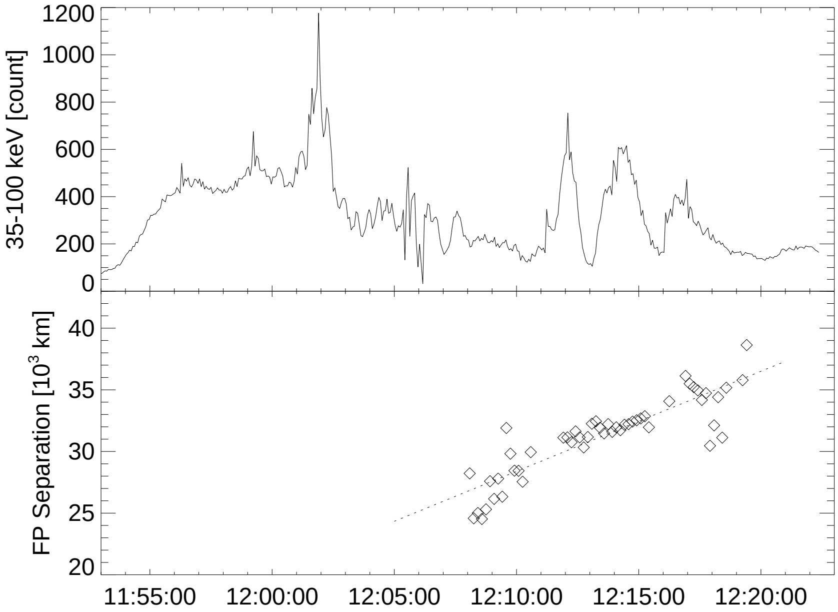

Figure 3.7: a) RHESSI count rate lightcurve for energy band 35 to 100 keV. b) Time series of fitted FP separation shows no obvious correlation with HXR flux.

footpoints can be calculated. The time series of the separation of the footpoints is shown in Fig. 3.7. No obvious modulation with the HXR flux is observed, but rather a more or less constant motion with an averaged separation speed of $\approx 15\,\mathrm{km/sec}$.

3.4 Correlation and Discussion

In a simple reconnection model the energy deposition rate is supposed to be proportional to the product of the magnetic field in the reconnection region, the magnetic field in the footpoints and the velocity of the footpoint separation, i.e.

$$H \propto B_{corona} B_{fp} v_{fp} \tag{3.4}$$

according to equation 3.3 as described in section 3.1. The numerical differentiation that is needed to derive the velocity v_{fp} introduces large uncertainties; especially in the case of the measured footpoint separation shown in Fig. 3.7b.

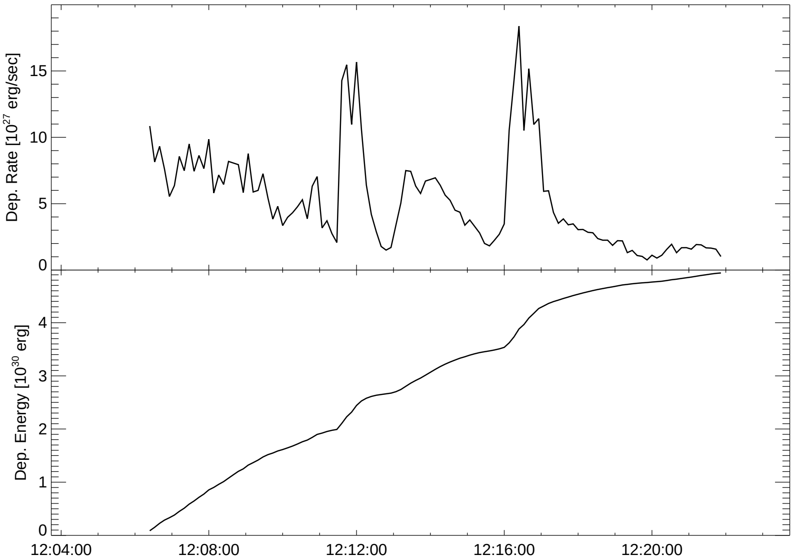

Figure 3.8: a) Energy deposition rate derived from power-law fit to photon spectrum. b) Accumulated deposited energy as function of time with arbitrary point of origin.

Integrating equation 3.3,

$$\int_{t_1}^{t_2} S\,\mathrm{dt} \;=\; \frac{1}{2\pi}\int_{t_1}^{t_2} B_{corona}B_{fp}v_{fp}A_r\,\mathrm{dt}\ , \tag{3.5}$$

leads to the difference equation

$$E(t_2)\,-\,E(t_1) \;=\; \frac{1}{4\pi}(s(t_2)-s(t_1))\cdot B_{corona}B_{fp}A_r\ , \tag{3.6}$$

where the total deposited energy $E = \int H\,dt$ and the footpoint separation $s = \int 2v_{fp}dt$, assuming that the magnetic field and the reconnection area are constant in time.

Figure 3.8 shows the time series of the energy deposition rate and its integral, i.e. the total deposited energy. It suggests a total deposited energy of $\approx 5\cdot 10^{30}$ erg, a reasonable value for an X-class flare (e.g. Holman et al., 2003; Saint-Hilaire and Benz, 2004). Since the fitted cutoff energy is only an upper limit (see Fig. 3.4) those values for the deposited energy are lower limits. Furthermore, it seems to be likely that only a certain fraction of the energy inflow into the reconnection region is used to accelerate particles and can therefore be

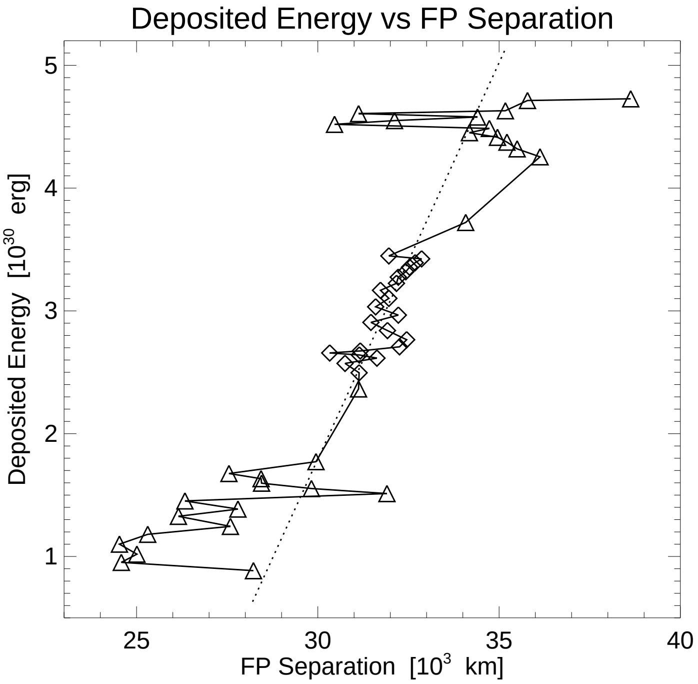

Figure 3.9: Correlation plot of footpoint separation and accumulated deposited energy. The data points between the attenuator changes (12:12 to 12:16 UT) are marked with diamonds and the linear fit shows $\Delta E/\Delta s \approx 5{\cdot}10^{30}$ erg / 7000 km. The triangles mark the data points before and after the attenuator change and the lines between the data points follow the timeline.

observed in the HXR footpoints. In the following, we assume that this fraction α is constant in time and therefore has no influence on the relation between footpoint separation and observed energy deposition.

Assuming all the energy inflow into the reconnection area is observed in the deposited energy shown in Fig.3.8,

$$\frac{\Delta E}{\Delta s} = \frac{1}{4\pi} B_{corona} B_{fp} A_r \, \alpha \tag{3.7}$$

according to equation 3.6.

Figure 3.9 shows a correlation plot of the footpoint separation and the deposited energy. The data points before 12:12 UT and after 12:16 UT (marked with triangles) have a low HXR flux and therefore, contain more noise. Due the change in attenuator state as mentioned in section 3.3.1 there are gaps in the measurement of the separation.

From the linear fit through the data points in the time interval from 12:12 UT to 12:16 UT (marked with diamonds in Fig. 3.9) $4\pi\Delta E/\Delta s \approx 9{\cdot}10^{22}\,\mathrm{G^2cm^2}$. Furthermore, reading an average magnetic field at the photosphere from the MDI magnetogram of $B_{fp} \approx 500\,\mathrm{G}$, assuming the magnetic field in the corona $B_{corona} \approx B_{fp}/5 \approx 100\,\mathrm{G}$ and putting $\alpha = 1$ an area for the reconnection region of $A_r \approx 360\,\mathrm{arcsec}^2$ can be estimated. It seems to be evident that the size of the reconnection area in horizontal direction must be in the order of the size of the footpoints, i.e. $l_h \approx 5 - 10\,\mathrm{arcsec}$, hence the vertical dimension of the reconnection area of $l_v \approx 36 - 72\,\mathrm{arcsec}$. That appears to be large, although not impossible. On the other hand, $B_{corona} \approx 100\,\mathrm{G}$ may be overestimated, α may be smaller than 1, and the measurement for the deposited energy is only a lower limit. The estimated lower limit of the vertical size $l_v \approx 50\,\mathrm{arcsec}$ could be larger by one order of magnitude, which is rather implausible.

3.5 Revisiting the July 23, 2002 Event

The intense solar flare of the GOES class X4.8 which occurred on July 23, 2002 at S13E72 has been extensively investigated (Lin et al., 2003). This two ribbon X-flare shows a HXR footpoint on the northern ribbon that moves systematically over 15 minutes and several sources on the other ribbon that move systematically only over 30 seconds or less. For the northern footpoint with a long duration systematic motion, Krucker et al. (2003) found a rough correlation between the HXR flux and the velocity of the motion, consistent with magnetic reconnection theory assuming a constant HXR spectrum (section 3.1). However, the spectrum is not constant in time (Holman et al., 2003) and shows even systematic spectral differences between the two footpoints (Emslie et al., 2003). Taking the spectral variations into account, the correlation found by Krucker et al. (2003) should even improve.

Here, the July 23 event is analyzed similar to the discussed event on March 18, 2003. Since only one footpoint shows a systematic motion, only this footpoint is considered. Instead of measuring the footpoint separation, the relative position of the footpoint is determined. This footpoint is moving almost on a straight line (see Krucker et al., 2003) and therefore, only the motion along this line is considered.

The power-law index of the non-thermal sources is between 2.5 and 3.5 during the main HXR peaks (Holman et al., 2003). The cutoff energy is difficult to determine because of strong thermal emission and therefore, it is set to 30 keV as an upper limit. Although the individual HXR footpoints show slightly different

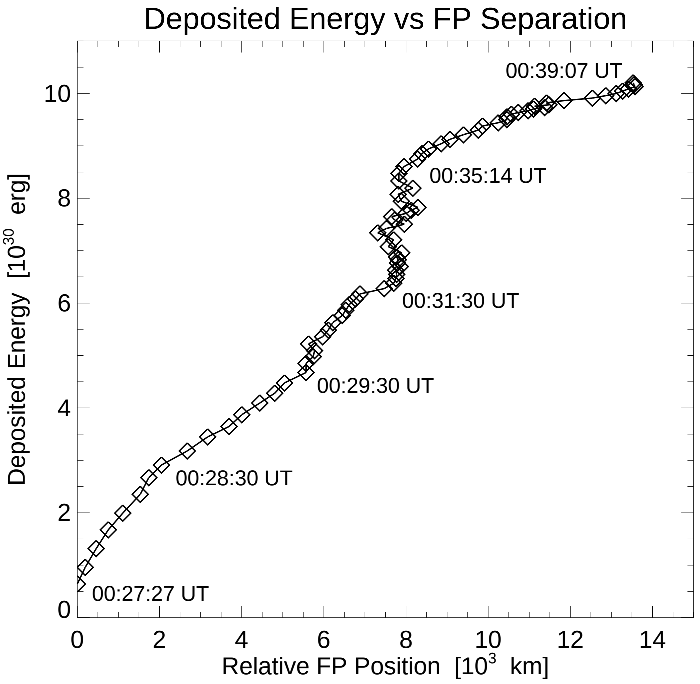

Figure 3.10: The correlation plot of accumulated deposited energy vs relative footpoint position for the July 23, 2002 event shows clearly linear correlations for four time intervals. However, the observed footpoint seems essentially not moving while still a substantial amount of energy is deposited for the interval between 00:31:30 and 00:35:05 UT.

spectra, their temporal variations are closely related (Emslie et al., 2003). To simplify the data analysis, it can therefore be assumed that half of the total deposited energy derived from the spatially integrated spectrum is seen in each footpoint, without introducing a time dependent error.

For the time intervals between 00:27:30 and 00:31:30 UT and between 00:35:15 and 00:39:00 UT, Fig. 3.10 shows at least four sub-intervals with clearly linear correlations between the deposited energy ΔE and the relative footpoint position Δs suggesting that $B = const$ is a good assumption for those sub-intervals. The MDI magnetogram shows a maximum of $B = 600\,\mathrm{G}$ along the line of sight. Therefore, $B_{fp} = 5 \cdot B_{corona} = 1000\,\mathrm{G}$ is assumed. Setting $l_h = 5\,\mathrm{arcsec}$, the diameter of the footpoint along the ribbon, and assuming $\alpha = 1$, gives a vertical length of the reconnection area $l_v \approx 20\,\mathrm{arcsec}$ for the earlier time interval (averaged over the three sub-intervals with separate linear correlations) and $l_v \approx 5\,\mathrm{arcsec}$ for the later time interval. During this time intervals, the HXR footpoint separation increases from ≈ 15 arcsec to ≈ 30 arcsec.

During the time interval between 00:31:30 and 00:35:00 UT, while still a lot of energy is deposited in the footpoint, its motion seems to be essentially absent, even though a small motion perpendicular to the main direction has been observed (Krucker et al., 2003). This results in $l_v \approx 500$ arcsec by making the same assumption as above. On the other hand, assuming a similar geometry as for the other time intervals, the magnetic field needed to be one order of magnitude stronger ($B_{corona} \approx 2000$ G). Both interpretations seem to be rather unlikely. Therefore, the simple reconnection scenario does not hold for this time interval.

3.6 Summary, Outlook and Conclusion

The analysis of the March 18, 2003 event suffers from several problems. First, the data of the analyzed X-flare is compromised by datagaps, changes in attenuator state and contamination with magnetospheric particle events. Additionally, the measured locations of sources, imaged with the forward fit algorithm currently implemented in the RHESSI software, show increased noise which possibly can be lowered with an improved algorithm. As the implemented forward-fit algorithm is not as well established, imaging with CLEAN and subsequently determining the centroid of the source, as it is used in the analysis of the July 23, 2002 event, leads to consistent results.

Using RHESSI spectroscopy and imaging, the dimensions of the reconnection region can be estimated using a simple reconnection model. Although the estimated dimensions are possible, there are indications that this simple model is not fully consistent with the observed data.

In the discussion of both events, the fraction α is set to 1, assuming the total energy flowing into the reconnection region is going into electron acceleration. Assuming that electrons are accelerated downwards and upwards and that only a part of the energy is used to accelerate electrons, the factor α needs to be smaller than 0.5. Setting $\alpha \approx 0.1$ would result in a calculated size of the reconnection region of an order of magnitude larger than presented in section 3.4 and 3.5. This means that the vertical size of the reconnection region would be $l_v \approx 500$ arcsec for the March 18, 2003 event, which is an implausible scale comparing to the footpoint separation (≈ 30 arcsec).

The correlation shown in Fig. 3.10 is among the best evidences that HXR source motions are correlated with the energy release in flares as predicted in magnetic reconnection models. Nevertheless, the deposited energy observed in the footpoints is generally to large comparing to the Poynting inflow into the reconnection region. Although these observations confirm some aspects of the simple reconnection model in a magnetic cusp, they highlight the flare energy problem.

Chapter 4

Conclusion and Outlook

4.1 Conclusion

The aspect system containing the Solar Aspect System (SAS) and the Roll Angle System (RAS) has been successfully built and integrated into the rotating spacecraft RHESSI, the Reuven Ramaty High Energy Spectroscopic Imager. It has been successfully calibrated in space. The SAS provides measurement of the pointing with an accuracy of better than 0.4 arcsec and measurement of the roll angle with an accuracy of better than 1 arcmin at all times. The off-line (ground-based) reconstruction of the aspect solution, together with the photon count rates of the nine bi-grid collimators combined with Ge-Detectors, provide image reconstruction of solar X-ray and gamma-ray sources with an accuracy of about 1 arcsec.

Hard X-ray footpoints of solar flares have been imaged. Their momentary location has been correlated with the total energy deposited in the chromosphere by accelerated particles. Assuming a simple reconnection scenario for a flare, this correlation allows an estimate of the dimensions of the reconnection region. While the model of the reconnection scenario is supported for particular time intervals, calculated dimensions of the reconnection region seem to be implausible for others.

4.2 Outlook

In the correlation of footpoint motions with the total deposited energy, serveral parameters are assumed to be constant. In particular, an averaged magnetic field has been assumed to be constant at the footpoints and also at the reconnection region. Futhermore, it's poorly understood why X-ray footpoints appear as rather compact sources comparing to the ribbons seen in EUV. The influence of the limited dynamic range of the RHESSI imaging needs to be investigated.

The SAS measures the solar radius with a high frequency and preliminary results were presented. A stable calibration of the SAS of one to two orders of magnitude better than required for imaging has to be achieved. This will allow integration of the data over the whole mission including approximately 6×10^9 single measurements.

It has been pointed out in section 2.2.5 that the RAS is measuring the polar angle of star events with a high accuracy. These measurements provide information about the pointing of the spacecraft. Reconstructing the pointing from the measured polar angle on the RAS allows imaging while the spacecraft isn't pointed at the Sun. The spacecraft has been pointed at the crab nebula during its closest approach to the Sun. A reconstruction of the aspect solution using the RAS data only will allow imaging of the crab nebula.

Appendix A

Aspect Solution User's Guide

Introduction

RHESSI has two subsystems (SAS and RAS) of sensors, which acquire data for off-line reconstruction of the aspect solution. The SAS (Solar Aspect System) consists of three lens/sensor pairs measuring the Solar limb at about 670 nm. The off-line data analysis reconstructs the Sun center with respect to the imaging axis (the reference telescope axis). The RAS (Roll Angle System) is a star tracker pointing radially outwards. With respect to the rotating spacecraft, the images of stars are traveling over a linear CCD and are triggering star events to be included in the telemetry data. By comparing with a star catalog, the off-line analysis software calculates the momentary roll angle. The integration of both information provides the aspect solution to be used for image reconstruction.

A.1 Software Flow Overview

The transmitted data consists of Solar limb data from the SAS, CCD pixels around the intersection of a Solar image with three linear CCDs, and Star event data from the RAS, CCD pixels induced by passages of Star images over a linear CCD. Fig. A.2 shows the flow diagram of the aspect solution software. The Solar limbs and the Star events are fitted independently. Knowing the geometry of all features of the SAS, the position of the Sun center, with respect to a spacecraft fixed coordinate system, can be calculated, and a list of position angle marks can be generated by fitting of the Star events and subsequent comparison with a Star catalog. Integrating these information allows a correction and interpolation of the roll angles. Finally, the coordinates are converted into the needed pointing and roll angle format with respect to a Solar fixed coordinate system.

A.2 The Aspect Coordinate System

Solar Aspect System SAS

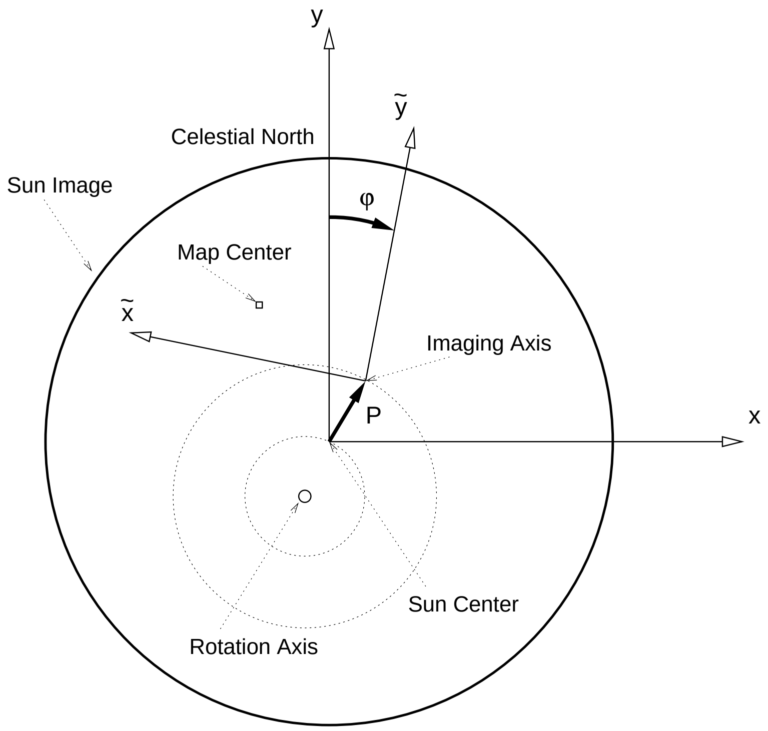

Figure A.1: The aspect coordinate system. The circle drawn with a solid line represents the Solar limb. (x,y) refers to an inertial coordinate system with y pointing towards the north celestial pole. (x̃,ỹ) refers to the imaging coordinate system, which is fixed to the S/C. P is the pointing vector in units of [arcsec] and φ is the rotation angle in [radian], which is increasing in time.

The SAS features define the reference coordinate system to be used for the image reconstruction. This coordinate system is called the imaging coordinate system (or SAS coordinate system) and has been chosen in order to optimize the SAS field of view in a symmetrical way. The z-axis is parallel to the line from the center of gravity of the three CCD mid-points to the center of gravity of the lens centers and its pointing towards the Sun. The x- and y-axis are chosen to form a right-handed Cartesian coordinate system with the y-axis being parallel to the xy-plane of the rear tray coordinate system, which had been used as the reference for building the imager. The origin of the imaging coordinate system is the center of gravity of the CCD mid-points.

In Fig. A.1 $\tilde{x}$ and $\tilde{y}$ refers to the SAS coordinate system. In spacecraft fixed coordinates, the pointing is given by the vector from the origin of the SAS coordinate system to the momentary Sun center and is measured as an angle in arcsec. Therefore, the pointing is the $\tilde{x}$- and $\tilde{y}$-component of the angle between the $\tilde{z}$-axis and the direction towards the Sun center. Internally of the aspect solution software, the limb positions are calculated in a pixel based coordinate system. Using the appropriate plate scale, the coordinates are converted to arcsec in order to provide a SAS solution.

Roll Angle System RAS

The roll angle system measures the momentary roll angle of the rotation spacecraft. From the spacecraft looking towards the Sun, the spacecraft is rotating clockwise. Therefore, the momentary rotation vector is pointing more or less in the direction of the z-axis of the imaging coordinate system. After correcting for the off-pointing (i.e. align the z-axis to point towards the Sun center), the roll angle is defined to be the angle between the Solar fixed y-axis, which is pointing from the Sun center towards the north celestial pole (see Fig. A.1), and the imaging $\tilde{y}$-axis. The angle is defined to be increasing in time and is measured in radians.

The Aspect Solution

For the imaging reconstruction, the momentary grid phase and roll angle is relevant. Nevertheless, in order to have a clean and easy to understand interface, the aspect solution is defined to be a discrete list of sets of a pointing vector in Solar fixed coordinates, a roll angle and a time mark. The pointing vector contains the x- and y-component of the angle from the direction towards the Sun center and the imaging $\tilde{z}$-axis as shown in Fig. A.1 and is measured in arcseconds. The roll angle is defined as described above.

A.3 The Aspect Reconstruction Software

For the most of the RHESSI data analysis, the aspect reconstruction suppose to be completely transparent. For documentation reason, especially for analysis software programmers, the command line interface is described here on the level of the aspect solution object.

Create an Object and Retrieve Data

The following commands show how to create an instance of the aspect solution object and how to retrieve data for a given time range. The definition of the 'aspect_time_range' is optional. If it's omitted, it's automatically set to 'obs_time_interval'. Setting the 'obs_time_interval' requires the RHESSI database files to be correctly installed and the RHESSI related environment variables to be set.

```
IDL> o=hsi_aspect_solution()
IDL> o->set,obs_time_interval='2002-03-13 '+['12:30','13:00']
IDL> o->set,aspect_time_range='2002-03-13 '+['12:40','12:45']
IDL> data=o->getdata()
```

Instead of defining an 'obs_time_interval', the 'filename' and 'file_type' can be set directly. This is especially useful to analyze smex-files, which are not included in the RHESSI database, yet. The following example it's assumed, that the given file resides in the current directory. Otherwise, the current directory has to be changed or the filename has to be given including the relative or absolute path. Once again, the definition of the 'aspect_time_range' is optional. By default, it's set to 'file_time_range'.

```
IDL> o=hsi_aspect_solution()
IDL> o->set,filename='vc3_20020314065802.0',file_type='smex'
IDL> o->set,aspect_time_range='2002-03-13 '+['12:40','12:45']
IDL> data=o->getdata()
```

Aspect Data Format

Assuming the variable 'o' is an instance of an aspect solution object, which is defined as shown above. The returned aspect solution data is then structured as shown by the following commands.

```
IDL> data=o->getdata()
IDL> help, data, /struct
** Structure <40491c08>, 4 tags, length=537488, refs=2:
   TIME            LONG      Array[26874]
   T0              STRUCT    -> HESSI_SCTIME_FULL Array[1]
   POINTING        FLOAT     Array[26874, 2]
   ROLL            DOUBLE    Array[26874]
```

The tag 'T0' of the variable 'data' holds the reference time in the sctime format. The tag 'time' is an array of relative times of the data points with respect to 'T0' and is given in units of 2^{-7} seconds. The components [*,0] of the tag 'pointing' are the x-components and the [*,1] are the y-components of the pointing vector in units of arcseconds as described in section A.2. Finally, the tag 'roll' holds the array of roll angles in radians as described in section A.2.

Aspect Data at Given Times

To calculate an aspect solution for an array of given times the three input parameter THIS_UT_REF, THIS_TIME and THIS_UNIT_TIME can be specified to the getdata() methode of the aspect solution object as shown below.

```
IDL> data=o->getdata(this_ut_ref='2002-03-13 12:41', $
                     this_time=findgen(40), this_unit=2L^18)
IDL> help,data
DATA            STRUCT    = -> HSI_ASPECT Array[40]
IDL> help,data,/str
** Structure HSI_ASPECT, 4 tags, length=16, data length=16:
   DX              FLOAT           579.793
   DY              FLOAT          -69.4515
   PHI             FLOAT           244.664
   DELTA            INT              0
```

The return value is an array of structures {hsi_aspect}. 'DX' and 'DY' are the two components of the pointing vector and 'PHI' is the roll angle, both as described above. The entry 'DELTA' describes the spacing of the measured SAS data points. If the corresponding time falls between two measured points then 'DELTA' is the length of that interval in units of 1/8 of a second rounded to the next lower integer value. If the corresponding time is before or after all returned (measured) data points then 'DELTA' is the negative time to or since the closest data point.

Retrieve Aspect Information from Existing Imaging Object

Let's assume the variable 'o' refers to an instance of an object class, which inherits an aspect solution object. For instance, let's assume 'o' refers to an instance of the 'hsi_image' object class. Using the following command line, the corresponding aspect solution data can be retrieved. The variable 'data' has the same format as described above.

```
IDL> data=o->getdata(class='hsi_aspect_solution',/this_class)
```

Control Parameters

In Table A.1 an overview of the control parameters of the aspect solution object is given. Reconstructing an image, the aspect solution control parameters suppose to have reasonable default value. Nevertheless, there are various circumstances where the aspect solution has to be controlled in more detail.

Parameter Name	Short Description	Units
ASPECT_CNTL_LEVEL	control levels between -2 and 10	-
ASPECT_TIME_RANGE	optional time range	anytim
RAS_TIME_EXTENSION	extension of time range for RAS	second
ASPECT_SIM	use simulated pointing	-
SASZERO	use pointing (0,0)	-
AS_SPIN_PERIOD	S/C spin period	second
AS_ROLL_OFFSET	roll angle at beginning of file	radian
AS_ROLL_SOLUTION	select mode of roll solution	-
AS_NO_EXTRAPOL	allow/deny extrapolation of data	-
PMTRAS_DIAGNOSTIC	levels of diagnostics for PMTRAS	-

Table A.1: The control parameters of the aspect solution object.

1. ASPECT_CNTL_LEVEL. At various places of the aspect solution software error messages or warnings are produced, quality control values are calculated and plots are generated. With the control parameter 'aspectcntl_level' level of controlling outputs can be selected. By default, aspect_cntl_level is set to zero, which print errors and some warnings to the IDL log window. The Table A.3 shows the valid settings and their results. In general, the

Parameter Name	Default Value
ASPECT_CNTL_LEVEL	0
ASPECT_TIME_RANGE	obs_time_int
RAS_TIME_EXTENSION	[-1400,+1400]
ASPECT_SIM	0
SASZERO	0
AS_SPIN_PERIOD	4.0
AS_ROLL_OFFSET	0.0
AS_ROLL_SOLUTION	'DBASE'
AS_NO_EXTRAPOL	1
PMTRAS_DIAGNOSTIC	0u

Table A.2: The table shows the default values of the control parameters.

higher the parameter is set, the more controlling messages, values and plots are generated.

-2	no Errors and no Warnings
-1	no Warnings
0	write Errors and Warnings
1	write some info to log window
2	write more info to log window
3	plot aspect solution
4	calculate quality (radii, triangle ...)
5	calculate quality, but no aspect plots
6	plot quality, but no aspect plots
7	aspect and quality plots
8	aspect and more quality plots

Table A.3: The valid values of the control parameter ASPECT_CNTL_LEVEL.

2. ASPECT_TIME_RANGE. With this control parameter, the time range can be specified, for which an aspect solution has to be calculated. In general, it's set automatically to a reasonable value. In particular, it can be useful to specify an aspect time range if an aspect solution object is defined by giving a filename. The 'aspect_time_range' has to be set to a valid 'anytim' format.

3. RAS_TIME_EXTENSION. A two element vector of delta times in seconds that specify the extension of the aspect time range to be used to calculate the roll solution. The first value is added to the beginning and the second is added the end to the time range. Therefore, the first value suppose to be a negative and the second a positive number. Currently, the aspect time range with the ras time extension can not exeed the observation time interval by more the 1400 seconds. The default value is [-1400,1400].

4. ASPECT_SIM. This control parameter is a flag, which is used to switch between the reconstructed aspect solution from the aspect packets and a simulated aspect behavior. The default value is zero, which means that the software reconstructs the aspect solution from the packets. Setting the value to 1 produces a simulated aspect behavior.

5. SASZERO. Setting the control parameter saszero to 1, forces the pointing vector to be constant at [0,0]. This does not affect the roll solution.

6. AS_SPIN_PERIOD. With this control parameter, spin period of the aspect solution can be controlled. It has to be given in seconds per revolution. This spin period is used for the simulated aspect behavior and for the case where as_roll_solution is set to 'FIX' (see below).

7. AS_ROLL_OFFSET. In the case where as_roll_solution is set to 'FIX', the roll angle is set to as_roll_offset at the beginning of the accessed file.

8. AS_ROLL_SOLUTION. By this parameter, the method of the roll angle solution can be chosen. Currently, the values given in Table A.4 are valid.

'DBASE'	read roll solution from the provided database
'FIX'	use fixed spin period
'PMT'	use the PMTRAS to generate the roll solution
'RAS'	use the CCD-RAS to generate the roll solution

Table A.4: The valid values of the control parameter AS_ROLL_SOLUTION. In the case the parameter is set to 'FIX' the control parameter AS_SPIN_PERIOD and AS_ROLL_OFFSET are used to specify the roll angle.

9. AS_NO_EXTRAPOL. By default, the user is prevented from using aspect data point, which had to be extrapolated from measured data points. By

setting this control parameter to 0 (zero), the software returns all measured data points within the aspect time range. If the keywords THIS_UT_REF, THIS_TIME and THIS_UNIT_TIME are used, the requested data points outside the aspect time range are extrapolated. In general, extrapolated data points can't be used for any data analysis.

10. PMTRAS_DIAGNOSTIC. By setting this parameter to a nonzero value, the PMTRAS software will print various information on the log window and produce various plot windows for diagnostic purposes. See the PMTRAS documentation for further information.

The Quality of the Aspect Solution

The aspect data are redundant in many ways. Therefore, the quality of the reconstructed aspect solution can be measured. However, at the current stage, many of the quality measurements are not in place yet. Describing only the quality measures which are calculated by the present software release, this section will evolve over time. Setting the control level to 4 or higher, the quality measures are calculated and stored in the info structure of the aspect solution object. The following command lines show how to access this information.

```
IDL> o->set,aspect_cntl_level=4
IDL> data=o->getdata()
IDL> info=o->get(/info)
IDL> help,info.as_quality,/struct
** Structure <40697188>, 3 tags, length=752476, refs=2:
   RADII           FLOAT     Array[26874, 6]
   TRIANGLE        FLOAT     Array[26874]
   RAS_RESIDUALS   POINTER   <NullPointer>
```

Reduced Triangle. For each SAS integration time, three pairs of Solar limbs are measured. Reconstructing the Sun center in the SAS coordinate system, the three mid-perpendiculars of the three pairs of limbs do not intersect in one point but form a triangle. The size of this reduced triangle is a measure for the quality of the SAS solution. Setting the control level to 6, the size is calculated, the moments of the size are displayed on the log window and the data versus time is plotted. Currently, a mean value < 0.5 arcsecond and a variance of ≈ 0.5 arcsecond^2 are reasonable values.

A.4 Simulated Aspect Data

There are two different ways to simulate an aspect solution instead of reconstructing it from the measured data. The simulation software is incorporated in the aspect solution object and can be controlled by the control parameters ASPECT_SIM and SASZERO. Setting ASPECT_SIM=1 produces an aspect solution with a simulated pointing behavior which is qualitatively similar to reality. The roll angle is calculated according to the control parameter AS_SPIN_PERIOD. Setting SASZERO=1 (preceding over ASPECT_SIM=1) produces an aspect solution assuming a perfect pointing to Sun center and calculating the roll angle according the control parameters AS_ROLL_SOLUTION and AS_SPIN_PERIOD.

A.5 Current Status and Restrictions

1. Although, the limbs are fitted to provide the pointing on a sub- arcsecond level, it's not checked whether the pointing accuracy complies with the 0.4 arcsecond requirements. Nevertheless, the estimated error is returned in the tag 'P_ERROR' if the aspect data is retrieved for given times.

2. Only SAS cycles with at least 2 limbs on two subsystems are taken as valid cycles. All other SAS cycles are currently ignored.

3. For the X-class flare on October 28, 2003, a customized pointing solution is read from the aspect database on SSW.

4. For the quality, only the triangle size and the solar radii from the SAS are calculated.

5. By default, the roll solution is read from the roll angle database on SSW. If no solution is available the software tries to reconstruct a PMTRAS solution. The control parameter AS_ROLL_SOLUTION can also be set to 'RAS' in order to reconstruct the roll angle from the CCD-RAS data. Although the latter isn't a robust software yet and the correct solution can depend critically from input parameters. Critical datagaps in the roll database will be filled with customized RAS solutions.

6. As default, the aspect time range has to be within the daytime portion of the orbit and the beginning and end must not fall within a big data gap of pointing measurements. By using the control parameter AS_NO_EXTRAPOL, the available data can be retrieved.

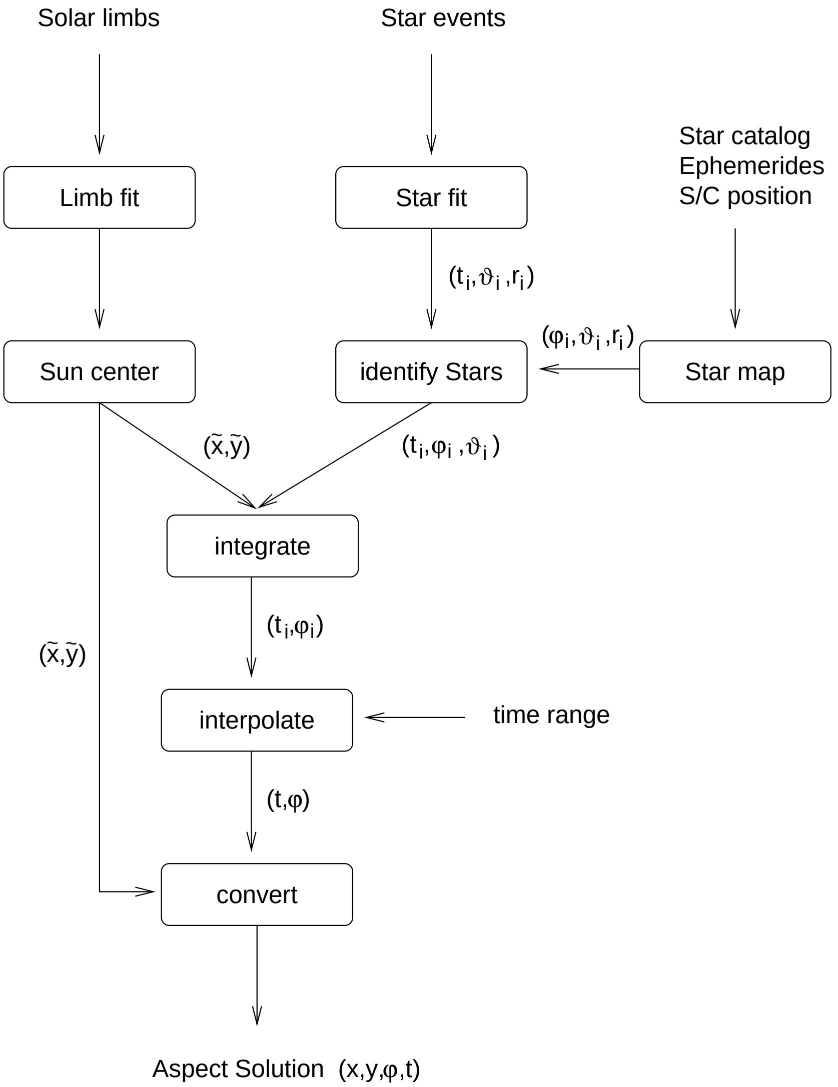

Figure A.2: Flow chart of the aspect solution software. The Solar limbs and the Star events are fitted independently. Using a Star catalog and the known geometry, the position of the Sun center in a spacecraft fixed coordinate system and a list of position angle marks can be calculated. Integration of these information, interpolation and coordinate transformation provides the needed pointing and roll angle information with respect to a inertial coordinate system.

Appendix B

ADP Parameter Table

B.1 Parameter Table

In this section, the Parameter Table (PT) is depicted. Table B.1 reflects the structure of the parameter table in the form it is sent to the ADP. The columns are as follows: *No* is the index number of the 2-byte word, *bits* is the bit number within the 2-byte word, *Wname* is the mnemonics for the 2-byte word, *Pname* is the mnemonics for the actual paramter, *L* stands for the level which is affected by the parameter (1: first-level FPGA, 2: second-level FPGA, S: ADP software), *Max* is the maximum value to be set, and *Description* is a short description (for a more verbose descripton see appendix B.2).

Table B.1: Structure of File of Parameter Table

No	bits	Wname	Pname	L	Max	Description
0		PTID	PTID	S	16383	identification of PT
1		OFFSET			255	address offset for PT
2		LENGTH			255	length of PT
3		SRCSR				
	3		RCCD	2	1	enable RAS
	2		SCCD2	2	1	enable SAS 12
	1		SCCD1	2	1	enable SAS 11
	0		SCCD0	2	1	enable SAS 10
4		CCD01				
	8-15		CCD1IT	2	255	SAS 11 integration time
	0-7		CCD0IT	2	255	SAS 10 integration time

continued on next page

Table B.1: *continued*

No	Bits	Wname	Pname	L	Max	Description
5		CCD2				
	15		SCADDIV	2	1	enable cadency divider
	14		LIMBLIM	2	1	enable 3FF suppression
	8-11		SFIRST	2	15	1st pixel
	0-7		CCD2IT	2	255	SAS 12 integration time
6	0-9	CCD0TL	CCD0TL	2	1023	SAS 10 limb trig level
7	0-9	CCD1TL	CCD1TL	2	1023	SAS 11 limb trig level
8	0-9	CCD2TL	CCD2TL	2	1023	SAS 12 limb trig level
9		SASCAD				
	12-15		SCAD	2	15	cadency
	8-11		RFIRST	2	15	1st pixel
	0-7		RCAD	2	255	cadency
10		FLAGS				
	15		RADJTHR	2	1	enbl RAS thr table
	14		RTSUM	2	1	enbl time summation
	13		RSSUM	2	1	enbl spatial summation
	12		RASTMEM	2	1	enbl time memory
	9-11		RASM	1	7	RAS 1st level mode
	6-8		SAS2M	1	7	SAS 12 1st level mode
	3-5		SAS1M	1	7	SAS 11 1st level mode
	0-2		SAS0M	1	7	SAS 10 1st level mode
11		RASTHR				
	14-15		RTHRMOD	S	3	trigger mode
	0-9		GLOBTHR	2	1023	global trigger level
12		RASSUM				
	11-15		ESTHR	1	31	earth shine threshold
	6-7		MID2SUM	2	3	# pxls for mid-2 sp.sum
	4-5		CENSUM	2	3	# pxls for central sp.sum
	2-3		MID1SUM	2	3	# pxls for mid-1 sp.sum
	0-1		OUTSUM	2	3	# pxls for outer sp.sum
13	0-7	SRD1DEL	SRD1DEL	2	255	pre-read delay
14		SRADPM				
	15		RASNTYP	S	1	n-pixel of RAS events
	14		IOWAIT	S	1	include I/O wait state
	11-12		reserved			used internally of ADP

continued on next page

Table B.1: *continued*

No	Bits	Wname	Pname	L	Max	Description
	10		SASSEC	S	1	SAS, every second pixel
	9		SASIM8	S	1	SAS 8bit images
	8		SASLI8	S	1	SAS 8bit limbs
	7		RASSIM	S	1	RAS spat. summed img
	5-6		ADPTEST	S	3	ADP test pattern
	4		RASETYP	S	1	enable RAS time events
	3		RASIM	S	1	RAS images
	2		RASEV	S	1	enable RAS events
	1		SASIM	S	1	SAS 10bit images
	0		SASLI	S	1	SAS 10bit limbs
15		SLNP				
	8-15		SLNPI	S	255	no. of pixels < trigger
	0-7		SLNPK	S	255	no. of pixels >= trigger
16	0-9	OUTTHR	OUTTHR	S	1023	outer area trigger level
17	0-9	MID1THR	MID1THR	S	1023	middle area 1 trigger level
18	0-9	CENTHR	CENTHR	S	1023	center area trigger level
19	0-9	MID2THR	MID2THR	S	1023	middle area 2 trigger level
20		MISEP				
	15		MISEPEN	S	1	enbl min. limb separation
	0-10		MISEPNO	S	2047	minimum limb separation
21		RRATIO				
	15		RERAENA	S	1	enable image ratio
	0-14		RERATIO	S	32767	image ratio
22		RTNLOF				
	15		TNLHWEN	S	1	enbl HW trig. # limit
	14		TNLSWEN	S	1	enbl SW trig. # limit
	13		ESTHREN	S	1	suppr. earthshine fastrd
	0-8		RTNL	S	255	trigger number limit
23		SLNLOF				
	15		LNLHWEN	S	1	enbl HW limb # limit
	14		LNLSWEN	S	1	enbl SW limb # limit
	0-8		SLNL	S	255	value of limb # limit
24		SRFD				
	8-15		SFD	S	255	# of ign. frames at start
	0-7		RFD	S	255	# of ign. frames at start

continued on next page

Table B.1: *continued*

No	Bits	Wname	Pname	L	Max	Description
25		SRATIO				
	15		SLRAENA	S	1	enable image ratio
	0-14		SLRATIO	S	32767	image ratio
26	0-7	RAFGDA	RAFGDA	S	255	del frames aft. earthshine
27		ACS10W				
	15		ACS12EN	S	1	enable SAS 12 for ACS
	14		ACS11EN	S	1	enable SAS 11 for ACS
	13		ACS10EN	S	1	enable SAS 10 for ACS
	0-10		ACS10	S	2047	SAS10 pixel shift, ACS
28	0-10	ACS11	ACS11	S	2047	SAS11 pixel shift, ACS
29	0-10	ACS12	ACS12	S	2047	SAS12 pixel shift, ACS
30	0-7	RBETHR	RBETHR	S	255	# of adj. pxls below thr

B.2 Describtion of Parameters

B.2.1 ADP Parameters

RCCD {word 3 bit 3}
1: enable RAS
0: disable RAS

SCCD0 {word 3 bit 0}
1: enable SAS 10

SCCD1 {word 3 bit 1}
1: enable SAS 11

SCCD2 {word 3 bit 2}
1: enable SAS 12

SASIM {word 14 bit 1}
1 enable SAS images (10bits/pixel)

SASLI {word 14 bit 0}
1 enable SAS limbs (10bits/pixel)

SASIM8 {word 14 bit 9}
1 enable SAS images (8bits/pixel)

SASLI8 {word 14 bit 8}
1 enable SAS limbs (8bits/pixel)

SASSEC {word 14 bit 10}
0 all pixels are taken
1 take every second pixel (by SW; odd or even?)

RASSIM {word 14 bit 7}
0 no RAS spatial summed images
1 write RAS spatial summed images (APP-ID=261)

RASIM {word 14 bit 3}
1 enable RAS images

RASEV {word 14 bit 2}
1 enable RAS events

RASETYP {word 14 bit 4}
0 simple RAS events
1 matrix RAS events, with previous an following pixel values
(needs RASEV to be enabled)

RASNTYP {word 14 bit 15}
0 'old' event type
1 n-pixel event type written to tele packets
(needs RASEV to be enabled, and RASETYP for matrix events)

ADPTEST {word 14 bits 6-5}
bit5: ADP ramp test mode
bit6: fixed pattern (AAAA-5555)

IOWAIT {word 14 bit 14}
include additional 50ns I/O wait state
0: fast I/O reading (50ns, 0 to 30 degreeC)
1: slow I/O reading (100ns, 10 to 60 degreeC)

PTID {word 0 bit 0-13}
identification number of ADP parameter table

B.2.2 SAS Parameters

SCAD {word 9 bits 12-15}
1: 8 Hz
9: 16 Hz
13: 32 Hz

15: 64 Hz
x: 128 Hz

SCADDIV {word 5 bit 15}
0: 8-64 Hz
1: 128 Hz

SFIRST {word 9 bits 8-11}
0: ignore first 15 pixels (or 16)
2: ingore 13 pixels (best value for FM)
7: ignore 8 pixels
15: ignore 0 pixel (or 1?), use for communication test

SRD1DEL {word 13 bits 0-7}
SAS pre-read delay
140: required value for FM
corresponding to 20.4 μs between end of pre-read and start

SAS0M {word 10 bit 0}
define SAS 10 first level mode
0 normal mode, 1mv/channel
1 high resolution mode, 0.5mV/channel
2 signal, 2mV/channel
3 offset, 2mV/channel
4 LED, 1mV/channel
5 LED 50%, 1mV/channel
6 communication test
7 normal mode, running average

SAS1M {word 10 bit 1}
define SAS 11 first level mode

SAS2M {word 10 bit 2}
define SAS 12 first level mode

LIMBLIM {word 5 bit 14}
1 enable 3ff-limb suppression

CCD0IT {word 4 bits 0-7}
SAS 10 integration time

CCD1IT {word 4 bits 8-15}
SAS 11 integration time

CCD2IT {word 5 bits 0-7}
SAS 12 integration time

CCD0TL {word 6 bits 0-9}
SAS 10 trigger level (not inverted)
(in channels of the according 10 bit resolution)

CCD1TL {word 7 bits 0-9}
SAS 11 trigger level

CCD2TL {word 8 bits 0-9}
SAS 12 trigger level

SLNPI {word15 bits 8-15}
no of limb pixels below threshold
(for 8bit limbs: SLNPI+SLNPK must be even)

SLNPK {word 15 bits 0-7}
no of limb pixels above or equal threshold
(for 8bit limbs: SLNPI+SLNPK must be even)

SLRAENA {word 25 bit 15}
1 enable SAS image taking by ratio

SLRATIO {word 25 bits 0-14}
SAS limb/image ratio
limbs are generated according to SCAD
images are generated with a frequency of
$SCAD/2/(SLRATIO \,\&\, 2^{15}-1)$
example: RATIO=2 means taking every 4th image

MISEPEN {word 20 bits 15}
enable SAS minimum limb separation

MISEPNO {word 20 bits 0-10}
no of SAS minimum limb separation

SFD {word 24 bits 8-15}
SFD*4 number of SAS frames to be disgarded after ADP run

LNLHWEN {word 23 bit 15}
0 all limbs are processed
(no more than HW limit, which is 480)
1 LNLSWEN is checked

LNLSWEN {word 23 bit 14}
This flag is only checked if LNLHWEN is enabled.
0 if less than SLNL triggers: all limbs are processed
else no limb is processed
1 if less than SLNL triggers: all limbs are processed
else the first SLNL triggers are processed

SLNL {word 23 bits 0-8}
max number of processed limbs
See LNLHWEN and LNLSWEN for use of this number.
((should be smaller than ???))

ACS10EN {word 27 bit 13}
1: enable SAS 10 for ACS code

ACS11EN {word 27 bit 14}
1: enable SAS 11 for ACS code

ACS12EN {word 27 bit 15}
1: enable SAS 12 for ACS code

ACS10 {word 27 bits 0-10}
shift of mid-limb position for SAS 10 in pixels

ACS11 {word 28 bits 0-10}
shift of mid-limb position for SAS 11 in pixels

ACS12 {word 29 bits 0-10}
shift of mid-limb position for SAS 12 in pixels

B.2.3 RAS-Parameters

RCAD {word 9 bit 0-7}
int.time=(256-RCAD)*256 bms (binary micro seconds)

RFIRST {word 9 bits 8-11}
RAS first pixel
15: no pixels from Sensor ignored, use for communication test
14: 1 pixel from Sensor ignored
11: 4 pixels ignored (best value for FM)
..
0: 15 pixels from Sensor ignored

RASM {word 10 bit 3}
define RAS first level mode:
0 98 lines binning, (?? default 1V ES threshold)
1 48 lines binning, (?? default 1V ES threshold)
2 increment ES threshold counter
3 8 lines binning (for fast reading)
4 LED
5 signal

6 offset
7 communication test, reset ES threshold counter

RTSUM {word 10 bit 14}
1: enable RAS time summation

RSSUM {word 10 bit 13}
1: enable RAS spatial summation

RASTMEM {word 10 bit 12}
1: enable RAS time memory

RADJTHR {word 10 bit 15}
1: enable RAS threshold table (instead of global thresholding)

RTHRMOD {word 11 bits 14-15}
15 14 (bit no)
0 0 global threshold
0 1 region thresholds
1 x threshold table

GLOBTHR {word 11 bits 0-9}
RAS global threshold (not inverted)

CENTHR {word 18 bits 0-9}
RAS center area threshold (not inverted)

MID1THR {word 17 bits 0-9}
RAS mid1 area threshold (not inverted)

MID2THR {word 19 bits 0-9}
RAS mid2 area threshold (not inverted)

OUTTHR {word 16 bits 0-9}
RAS outer area threshold (not inverted)

ESTHR {word 12 bits 11-15}
define threshold for earth shine signal (ES).
$(X + 1) * 128/2^{12} * 2V$ ($\approx (X + 1) * 64mV$)

CENSUM {word 12 bits 4-5}
number of pixels to sum over for center area
0 summation over 4 pixels
1 summation over 3 pixels
2 summation over 2 pixels
3 no summation

MID1SUM {word 12 bits 2-3}
number of pixels to sum over for mid1 area

MID2SUM {word 12 bits 6-7}
number of pixels to sum over for mid2 area

OUTSUM {word 12 bits 0-1}
number of pixels to sum over for outer area

RERAENA {word 21 bits 15}
1 enable RAS image taking by ratio

RERATIO {word 21 bits 0-14}
RAS event/image ratio
images are generated with a frequency of
$RCAD/2/(RERATIO\&2^{15} - 1)$
example: RATIO=2 means taking every 4th image

RFD {word 24 bits 0-7}
RFD*4 number of RAS frames to be discarded after ADP run

TNLHWEN {word 22 bit 15}
0 all events are processed
(no more than HW limit, which is 480)
1 TNLSWEN is checked

TNLSWEN {word 22 bit 14}
This flag is only checked if TNLHWEN is enabled.
0 if less than RTNL triggers: all events are processed
else no event is processed
1 if less than RTNL triggers: all events are processed
else the first RTNL triggers are processed

ESTHREN {word 22 bit 13}
0 enable earth shine fast read
1 disable earth shine fast read

RTNL {word 22 bits 0-8}
max number of processed events
See TNLHWEN and TNLSWEN for use of this number.
((should be smaller than $t_{int}/20\mu$sec))

RAFGDA {word 26 bits 0-7}
X*4 number of frames to discard after earth shine signal
goes down (using fast reading, RCAD=247)

RBETHR {word 30 bits 0-8}
number of adjacent pixels below threshold

B.3 Editor for Parameter Table

The IDL-program 'hsi_as_ptedit' provides an easy to use graphical user interface to generate and read ADP parameter tables.

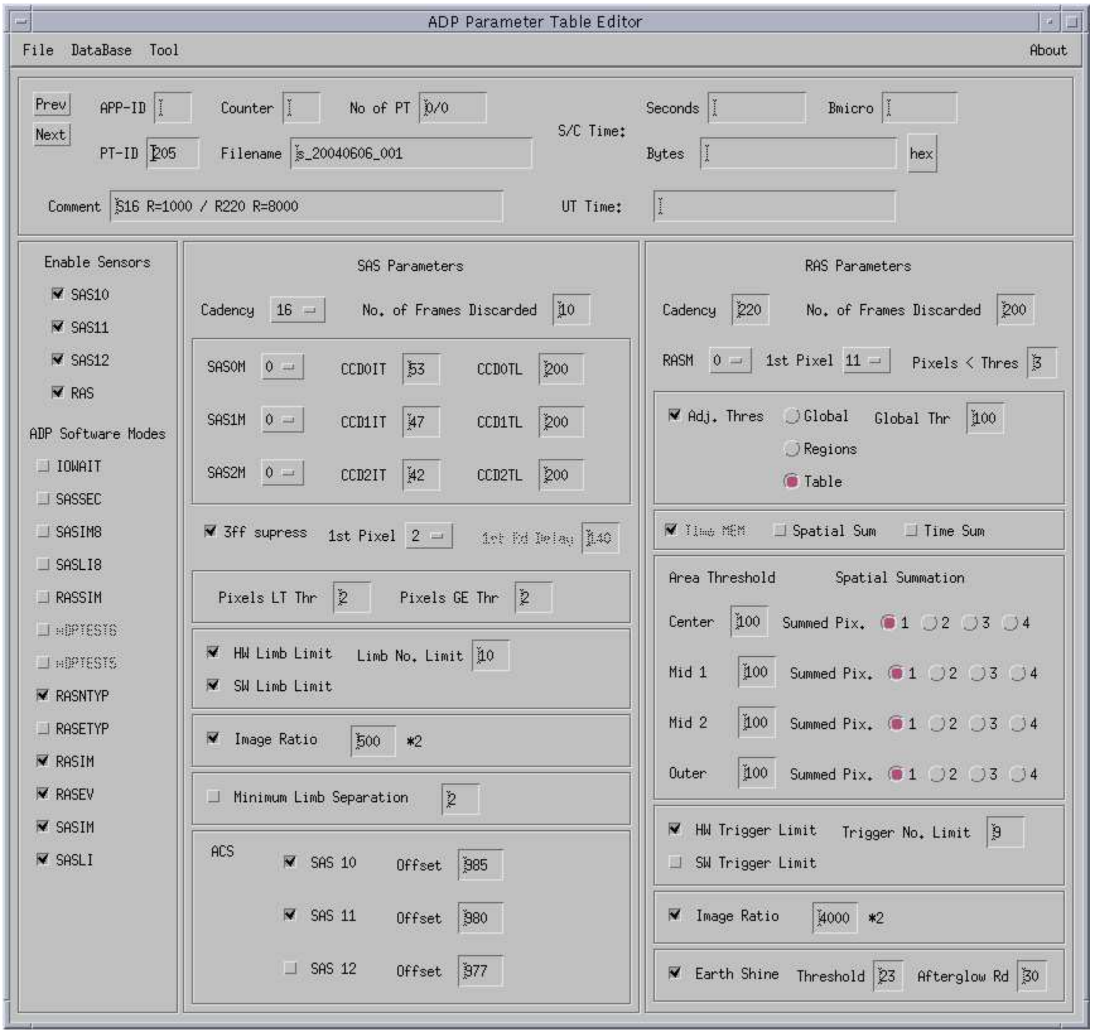

APP-ID
Counter
No of PT 0/0
PT-ID 205
Filename s_20040606_001
Comment S16 R=1000 / R220 R=8000
S/C Time: Seconds
Bmicro
Bytes
UT Time:

Enable Sensors
☑ SAS10
☑ SAS11
☑ SAS12
☑ RAS

ADP Software Modes
☐ IOWAIT
☐ SASSEC
☐ SASIM8
☐ SASLI8
☐ RASSIM
☐ ADPTEST6
☐ ADPTEST5
☑ RASNTYP
☐ RASETYP
☑ RASIM
☑ RASEV
☑ SASIM
☑ SASLI

SAS Parameters
Cadency 16
No. of Frames Discarded 10
SAS0M 0 CCD0IT 53 CCD0TL 200
SAS1M 0 CCD1IT 47 CCD1TL 200
SAS2M 0 CCD2IT 42 CCD2TL 200
☑ 3ff supress 1st Pixel 2 1st Fd Delay 140
Pixels LT Thr 2 Pixels GE Thr 2
☑ HW Limb Limit Limb No. Limit 10
☑ SW Limb Limit
☑ Image Ratio 500 *2
☐ Minimum Limb Separation 2
ACS
☑ SAS 10 Offset 985
☑ SAS 11 Offset 980
☐ SAS 12 Offset 977

RAS Parameters
Cadency 220
No. of Frames Discarded 200
RASM 0 1st Pixel 11 Pixels < Thres 3
☑ Adj. Thres ○ Global ○ Regions ● Table Global Thr 100
☑ Time MEM ☐ Spatial Sum ☐ Time Sum
Area Threshold Spatial Summation
Center 100 Summed Pix. ● 1 ○ 2 ○ 3 ○ 4
Mid 1 100 Summed Pix. ● 1 ○ 2 ○ 3 ○ 4
Mid 2 100 Summed Pix. ● 1 ○ 2 ○ 3 ○ 4
Outer 100 Summed Pix. ● 1 ○ 2 ○ 3 ○ 4
☑ HW Trigger Limit Trigger No. Limit 9
☐ SW Trigger Limit
☑ Image Ratio 4000 *2
☑ Earth Shine Threshold 23 Afterglow Rd 30

Figure B.1: Graphical user interface to edit the parameter table.

Curriculum Vitae

Personal Data

Name: Martin D. Fivian

Birth: Horgen, Switzerland, August 16, 1963

E-Mail: mfivian@ssl.berkeley.edu

Education

Doctoral Degree, ETH Zürich, Switzerland, (April 2005)

PhD student at Institute of Astronomy, ETH Zürich, (1998-2002)

Diploma in theoretical physics ETH Zürich, (1991)

Employment

University of California, Berkeley, (2002-present)

Paul Scherrer Institute, Villigen, Switzerland, (1998-2002)

Fiphys AG, Horgen, Switzerland, (1986-1998)

Institute for Histological and Cytological Diagnostics, Zürich, (1992-1998)

Brain Research Institute, University Zürich, Switzerland, (1991)

Awards

NASA Group Achievement Award to RHESSI Principal Investigator Team, July 19, 2003

NASA GSFC Group Achievement Award to RHESSI Data Analysis Team, August 24, 2004

List of Publications

M. Fivian, J. Bialkowski, W. Hajdas, R. Henneck, A. Mchedlishvili, P. Ming, K. Thomsen, A. Zehnder, G. J. Hurford, D. W. Curtis, D. Pankow, and B. R. Dennis. Calibrating the aspect systems of the high-energy solar spectroscopic imager (HESSI). In *Proc. SPIE Vol. 4012, p. 518-523, X-Ray Optics, Instruments, and Missions III, Joachim E. Truemper; Bernd Aschenbach; Eds.*, pages 518–523, July 2000.

M. Fivian, R. Henneck, A. Mchedlishvili, and A. Zehnder. RHESSI Aspect Reconstruction. *Solar Physics*, 210:87–99, Nov. 2002.

M. Fivian, R. Henneck, and A. Zehnder. RHESSI Aspect System and In-flight Calibration. In *Innovative Telescopes and Instrumentation for Solar Astrophysics. Edited by Stephen L. Keil, Sergey V. Avakyan . Proceedings of the SPIE, Volume 4853, pp. 60-70 (2003).*, pages 60–70, Feb. 2003a.

M. D. Fivian, H. S. Hudson, and R. P. Lin. Variations of Solar Radius: Observations with RHESSI. *American Astronomical Society Meeting*, 204:–+, May 2004.

M. D. Fivian, S. Krucker, and R. P. Lin. RHESSI Hard X-ray observations of the March 18, 2003 X-class Flare. *AAS/Solar Physics Division Meeting*, 34: –+, May 2003b.

R. Henneck, J. Bialkowski, F. Burri, M. Fivian, W. Hajdas, A. Mchedlishvili, P. Ming, K. Thomsen, J. Welte, A. Zehnder, B. R. Dennis, G. J. Hurford, D. W. Curtis, and D. Pankow. Solar Aspect System (SAS) for the High-Energy Solar Spectroscopic Imager (HESSI). In *Proc. SPIE Vol. 3765, p. 771-776, EUV, X-Ray, and Gamma-Ray Instrumentation for Astronomy X, Oswald H. Siegmund; Kathryn A. Flanagan; Eds.*, pages 771–776, Oct. 1999a.

R. Henneck, J. Bialkowski, F. Burri, M. Fivian, W. Hajdas, A. Mchedlishvili, P. Ming, K. Thomsen, J. Welte, A. Zehnder, M. Dettwyler, F. Buerki, G. J. Hurford, D. W. Curtis, and D. Pankow. Roll Angle System (RAS) for the

High-Energy Solar Spectroscopic Imager HESSI. In *Proc. SPIE Vol. 3765, p. 518-523, EUV, X-Ray, and Gamma-Ray Instrumentation for Astronomy X, Oswald H. Siegmund; Kathryn A. Flanagan; Eds.*, pages 518–523, Oct. 1999b.

R. P. Lin, B. R. Dennis, G. J. Hurford, D. M. Smith, A. Zehnder, P. R. Harvey, D. W. Curtis, D. Pankow, P. Turin, M. Bester, A. Csillaghy, M. Lewis, N. Madden, H. F. van Beek, M. Appleby, T. Raudorf, J. McTiernan, R. Ramaty, E. Schmahl, R. Schwartz, S. Krucker, R. Abiad, T. Quinn, P. Berg, M. Hashii, R. Sterling, R. Jackson, R. Pratt, R. D. Campbell, D. Malone, D. Landis, C. P. Barrington-Leigh, S. Slassi-Sennou, C. Cork, D. Clark, D. Amato, L. Orwig, R. Boyle, I. S. Banks, K. Shirey, A. K. Tolbert, D. Zarro, F. Snow, K. Thomsen, R. Henneck, A. Mchedlishvili, P. Ming, M. Fivian, J. Jordan, R. Wanner, J. Crubb, J. Preble, M. Matranga, A. Benz, H. Hudson, R. C. Canfield, G. D. Holman, C. Crannell, T. Kosugi, A. G. Emslie, N. Vilmer, J. C. Brown, C. Johns-Krull, M. Aschwanden, T. Metcalf, and A. Conway. The Reuven Ramaty High-Energy Solar Spectroscopic Imager (RHESSI). *Solar Physics*, 210:3–32, Nov. 2002.

K. Thomsen, J. Bialkowski, F. Burri, M. Fivian, W. Hajdas, A. Mchedlishvili, P. Ming, J. Welte, and A. Zehnder. Calibrating the imaging system of the high-energy solar spectroscopic imager (HESSI). In *Proc. SPIE Vol. 4012, p. 524-529, X-Ray Optics, Instruments, and Missions III, Joachim E. Truemper; Bernd Aschenbach; Eds.*, pages 524–529, July 2000.

A. Zehnder, J. Bialkowski, F. Burri, M. Fivian, R. Henneck, A. Mchedlishvili, P. Ming, J. Welte, K. Thomsen, D. Clark, B. R. Dennis, G. J. Hurford, D. W. Curtis, P. R. Harvey, and D. H. Pankow. RHESSI imager and aspect systems. In *Innovative Telescopes and Instrumentation for Solar Astrophysics. Edited by Stephen L. Keil, Sergey V. Avakyan . Proceedings of the SPIE, Volume 4853, pp. 41-59 (2003).*, pages 41–59, Feb. 2003.

Acknowledgments

I would like express my deepest gratitude and appreciation to a number of individuals who contributed to the outcome of this thesis and supported me in various ways.

First of all, I thank Arnold O. Benz. He introduced me to the RHESSI project and made it possible to do this work through all phases of a space mission, from design of the instrument to astrophysical results. I appreciate his encouragement for broadening horizons.

I thank Alex Zehnder for guiding me through an exciting process to get the instrument to actually to work. His creative way of leading the PSI-Team resulted in a beautiful RHESSI-Imager which has been up to this point, and for three years, in nearly flawless operation.

I thank Ralph Eichler for his engagement to be co-examiner. Together with Meinrad K. Eberle (former director) and Walter Fischer (former head of department), Ralph Eichler, as the director of PSI, made the “swiss contribution” to the RHESSI instrument a reality.

I am very grateful toward the highly motivated PSI RHESSI Team; their dedication was also inspiring. Very special thanks go to Reinhold Henneck, Aliko Mchedlishvili, Knud Thomsen, and Peter Ming; I enjoyed the collaboration, the creativity, and the opportunity to learn. Also, I keep warm memories of Claudia, Damian, Eugenie, Fritz, Gunnar, Jacek, John, Iwan, Kaspar, Laurent, Lukas, Manuel, Miha, Peter, Philippe, and Wojtek, who made my time at the Laboratory for Astrophysics at PSI an unforgettable experience.

I thank Robert P. Lin, director at Space Sciences Laboratory at UCB and Principal Investigator of RHESSI, for leading the RHESSI project to such a great success. To be in the influence of his vision and pursuit of challenging questions is invigorating.

I thank Gordon J. Hurford for having been such a wonderfully constructive mentor and for so many fruitful discussions; I thank Hugh S. Hudson for motivating me to get the best out of the SAS instrument; and I thank Säm Krucker

for supervising and supporting my work on footpoint motions.

I thank Brian R. Dennis, Peter R. Harvey, David W. Curtis, David Pankow, David M. Smith, Jim McTiernan, Richard Schwartz, Andre Csillaghy, and Kim Tolbert, and the entire RHESSI Team for their support, their dedication, and their collaboration.

There are no words to express my gratitude to my wife, Molly. Her love and patience, and her sunshine and colors pervade my soul.

Bibliography

C. W. Allen. *Astrophysical quantities.* London: University of London, Athlone Press, —c1973, 3rd ed., 1973.

M. J. Aschwanden, E. Schmahl, and t. R. Team. Reconstruction of RHESSI Solar Flare Images with a Forward Fitting Method. *Solar Physics*, 210:193–211, Nov. 2002.

D. W. Curtis, P. Berg, D. Gordon, P. R. Harvey, D. M. Smith, and A. Zehnder. The RHESSI Spacecraft Instrument Data Processing Unit. *Solar Physics*, 210: 115–124, Nov. 2002.

A. G. Emslie, E. P. Kontar, S. Krucker, and R. P. Lin. RHESSI Hard X-Ray Imaging Spectroscopy of the Large Gamma-Ray Flare of 2002 July 23. *The Astrophysical Journal Letters*, 595:L107–L110, Oct. 2003.

M. Fivian, J. Bialkowski, W. Hajdas, R. Henneck, A. Mchedlishvili, P. Ming, K. Thomsen, A. Zehnder, G. J. Hurford, D. W. Curtis, D. Pankow, and B. R. Dennis. Calibrating the aspect systems of the high-energy solar spectroscopic imager (HESSI). In *Proc. SPIE Vol. 4012, p. 518-523, X-Ray Optics, Instruments, and Missions III, Joachim E. Truemper; Bernd Aschenbach; Eds.*, pages 518–523, July 2000.

M. Fivian, R. Henneck, A. Mchedlishvili, and A. Zehnder. RHESSI Aspect Reconstruction. *Solar Physics*, 210:87–99, Nov. 2002.

M. Fivian, R. Henneck, and A. Zehnder. RHESSI Aspect System and In-flight Calibration. In *Innovative Telescopes and Instrumentation for Solar Astrophysics. Edited by Stephen L. Keil, Sergey V. Avakyan . Proceedings of the SPIE, Volume 4853, pp. 60-70 (2003).*, pages 60–70, Feb. 2003a.

M. D. Fivian, H. S. Hudson, and R. P. Lin. Variations of Solar Radius Observed with RHESSI. *AGU Fall Meeting Abstracts*, pages A1103+, Dec. 2003b.

M. D. Fivian, H. S. Hudson, and R. P. Lin. Variations of Solar Radius: Observations with RHESSI. *American Astronomical Society Meeting*, 204:–+, May 2004.

M. D. Fivian, S. Krucker, and R. P. Lin. RHESSI Hard X-ray observations of the March 18, 2003 X-class Flare. *AAS/Solar Physics Division Meeting*, 34: –+, May 2003c.

L. Fletcher and H. S. Hudson. Spectral and Spatial Variations of Flare Hard X-ray Footpoints. *Solar Physics*, 210:307–321, Nov. 2002.

R. Henneck, J. Bialkowski, F. Burri, M. Fivian, W. Hajdas, A. Mchedlishvili, P. Ming, K. Thomsen, J. Welte, A. Zehnder, B. R. Dennis, G. J. Hurford, D. W. Curtis, and D. Pankow. Solar Aspect System (SAS) for the High-Energy Solar Spectroscopic Imager (HESSI). In *Proc. SPIE Vol. 3765, p. 771-776, EUV, X-Ray, and Gamma-Ray Instrumentation for Astronomy X, Oswald H. Siegmund; Kathryn A. Flanagan; Eds.*, pages 771–776, Oct. 1999a.

R. Henneck, J. Bialkowski, F. Burri, M. Fivian, W. Hajdas, A. Mchedlishvili, P. Ming, K. Thomsen, J. Welte, A. Zehnder, M. Dettwyler, F. Buerki, G. J. Hurford, D. W. Curtis, and D. Pankow. Roll Angle System (RAS) for the High-Energy Solar Spectroscopic Imager HESSI. In *Proc. SPIE Vol. 3765, p. 518-523, EUV, X-Ray, and Gamma-Ray Instrumentation for Astronomy X, Oswald H. Siegmund; Kathryn A. Flanagan; Eds.*, pages 518–523, Oct. 1999b.

G. D. Holman, L. Sui, R. A. Schwartz, and A. G. Emslie. Electron Bremsstrahlung Hard X-Ray Spectra, Electron Distributions, and Energetics in the 2002 July 23 Solar Flare. *The Astrophysical Journal Letters*, 595: L97–L101, Oct. 2003.

G. J. Hurford and D. W. Curtis. The PMTRAS Roll Aspect System on RHESSI. *Solar Physics*, 210:101–113, Nov. 2002.

G. J. Hurford, E. J. Schmahl, R. A. Schwartz, A. J. Conway, M. J. Aschwanden, A. Csillaghy, B. R. Dennis, C. Johns-Krull, S. Krucker, R. P. Lin, J. McTiernan, T. R. Metcalf, J. Sato, and D. M. Smith. The RHESSI Imaging Concept. *Solar Physics*, 210:61–86, Nov. 2002.

H. Isobe, T. Yokoyama, M. Shimojo, T. Morimoto, H. Kozu, S. Eto, N. Narukage, and K. Shibata. Reconnection Rate in the Decay Phase of a Long Duration Event Flare on 1997 May 12. *The Astrophysical Journal*, 566:528–538, Feb. 2002.

E. Jakeman, G. Parry, E. R. Pike, and P. N. Pusey. The twinkling of stars. *Contemporary Physics*, 19:127–145, Mar. 1978.

S. Krucker, G. J. Hurford, and R. P. Lin. Hard X-Ray Source Motions in the 2002 July 23 Gamma-Ray Flare. *The Astrophysical Journal Letters*, 595:L103–L106, Oct. 2003.

R. P. Lin, B. R. Dennis, G. J. Hurford, D. M. Smith, A. Zehnder, P. R. Harvey, D. W. Curtis, D. Pankow, P. Turin, M. Bester, A. Csillaghy, M. Lewis, N. Madden, H. F. van Beek, M. Appleby, T. Raudorf, J. McTiernan, R. Ramaty, E. Schmahl, R. Schwartz, S. Krucker, R. Abiad, T. Quinn, P. Berg, M. Hashii, R. Sterling, R. Jackson, R. Pratt, R. D. Campbell, D. Malone, D. Landis, C. P. Barrington-Leigh, S. Slassi-Sennou, C. Cork, D. Clark, D. Amato, L. Orwig, R. Boyle, I. S. Banks, K. Shirey, A. K. Tolbert, D. Zarro, F. Snow, K. Thomsen, R. Henneck, A. Mchedlishvili, P. Ming, M. Fivian, J. Jordan, R. Wanner, J. Crubb, J. Preble, M. Matranga, A. Benz, H. Hudson, R. C. Canfield, G. D. Holman, C. Crannell, T. Kosugi, A. G. Emslie, N. Vilmer, J. C. Brown, C. Johns-Krull, M. Aschwanden, T. Metcalf, and A. Conway. The Reuven Ramaty High-Energy Solar Spectroscopic Imager (RHESSI). *Solar Physics*, 210:3–32, Nov. 2002.

R. P. Lin, P. T. Feffer, and R. A. Schwartz. Solar Hard X-Ray Bursts and Electron Acceleration Down to 8 keV. *The Astrophysical Journal Letters*, 557: L125–L128, Aug. 2001.

R. P. Lin, S. Krucker, G. J. Hurford, D. M. Smith, H. S. Hudson, G. D. Holman, R. A. Schwartz, B. R. Dennis, G. H. Share, R. J. Murphy, A. G. Emslie, C. Johns-Krull, and N. Vilmer. RHESSI Observations of Particle Acceleration and Energy Release in an Intense Solar Gamma-Ray Line Flare. *The Astrophysical Journal Letters*, 595:L69–L76, Oct. 2003.

M. L. McConnell, J. M. Ryan, D. M. Smith, A. G. Emslie, M. Fivian, G. J. Hurford, and R. P. Lin. RHESSI Studies of Solar Flare Hard X-Ray Polarization. *American Astronomical Society Meeting*, 204:–+, May 2004.

W. M. Neupert. Comparison of Solar X-Ray Line Emission with Microwave Emission during Flares. *The Astrophysical Journal Letters*, 153:L59+, July 1968.

M. Øieroset, R. P. Lin, T. D. Phan, D. E. Larson, and S. D. Bale. Evidence for Electron Acceleration up to ˜300 keV in the Magnetic Reconnection Diffusion Region of Earth's Magnetotail. *Physical Review Letters*, 89(19):195001–+, Oct. 2002.

E. R. Priest and T. G. Forbes. The magnetic nature of solar flares. *The Astronomy and Astrophysics Review*, 10:313–377, 2002.

J. Qiu, J. Lee, D. E. Gary, and H. Wang. Motion of Flare Footpoint Emission and Inferred Electric Field in Reconnecting Current Sheets. *The Astrophysical Journal*, 565:1335–1347, Feb. 2002.

P. Saint-Hilaire and A. O. Benz. Thermal and Non-Thermal Energies in Solar Flares. *Astronomy and Astrophysics*, to be published, 2004.

T. Sakao, T. Kosugi, and S. Masuda. Energy Release and Particle Acceleration in Solar Flares with Respect to Flaring Magnetic Loops. In *ASSL Vol. 229: Observational Plasma Astrophysics : Five Years of YOHKOH and Beyond*, pages 273–+, 1998.

R. A. Schwartz, A. Csillaghy, A. K. Tolbert, G. J. Hurford, J. McTiernan, and D. Zarro. RHESSI Data Analysis Software: Rationale and Methods. *Solar Physics*, 210:165–191, Nov. 2002.

P. Seige and G. Ress. Investigation of TI TC-104 linear CCD arrays with respect to applications in spaceborne camera systems. In *Solid state imagers and their applications; Proceedings of the Meeting, Cannes, France, November 26, 27, 1985 (A87-19702 07-33). Bellingham, WA, Society of Photo-Optical Instrumentation Engineers, 1986, p. 130-137.*, pages 130–137, 1986.

P. Seige and G. Ress. Application of Texas Instruments TC-104 linear CCD arrays in spaceborne camera systems. *Optical Engineering*, 26:1029–1034, Oct. 1987.

D. M. Smith, R. P. Lin, P. Turin, D. W. Curtis, J. H. Primbsch, R. D. Campbell, R. Abiad, P. Schroeder, C. P. Cork, E. L. Hull, D. A. Landis, N. W. Madden, D. Malone, R. H. Pehl, T. Raudorf, P. Sangsingkeow, R. Boyle, I. S. Banks, K. Shirey, and R. Schwartz. The RHESSI Spectrometer. *Solar Physics*, 210: 33–60, Nov. 2002a.

D. M. Smith, R. A. Schwartz, R. P. Lin, G. H. Share, R. J. Murphy, G. Hurford, S. Krucker, M. Fivian, L. Hyatt, B. R. Dennis, and N. Vilmer. RHESSI Gamma-Ray Line Spectroscopy of the X-class Flare of July 23, 2002. *AGU Fall Meeting Abstracts*, pages A461+, Dec. 2002b.

S. Sofia, W. Heaps, and L. W. Twigg. The solar diameter and oblateness measured by the solar disk sextant on the 1992 September 30 balloon flight. *The Astrophysical Journal*, 427:1048–1052, June 1994.

S. K. Solanki. Sunspots: An overview. *The Astronomy and Astrophysics Review*, 11:153–286, 2003.

K. Thomsen, J. Bialkowski, F. Burri, M. Fivian, W. Hajdas, A. Mchedlishvili, P. Ming, J. Welte, and A. Zehnder. Calibrating the imaging system of the high-energy solar spectroscopic imager (HESSI). In *Proc. SPIE Vol. 4012, p. 524-529, X-Ray Optics, Instruments, and Missions III, Joachim E. Truemper; Bernd Aschenbach; Eds.*, pages 524–529, July 2000.

A. M. Veronig and J. C. Brown. A Coronal Thick-Target Interpretation of Two Hard X-Ray Loop Events. *The Astrophysical Journal Letters*, 603:L117–L120, Mar. 2004.

G. J. Yates, L. B. Sprouse, D. R. Myers, and B. Turko. Characterization of electro-optic anomalies associated with transient response of fast readout charge-coupled devices. *Optical Engineering*, 26:747–756, Aug. 1987.

A. Zehnder, J. Bialkowski, F. Burri, M. Fivian, R. Henneck, A. Mchedlishvili, P. Ming, J. Welte, K. Thomsen, D. Clark, B. R. Dennis, G. J. Hurford, D. W. Curtis, P. R. Harvey, and D. H. Pankow. RHESSI imager and aspect systems. In *Innovative Telescopes and Instrumentation for Solar Astrophysics. Edited by Stephen L. Keil, Sergey V. Avakyan . Proceedings of the SPIE, Volume 4853, pp. 41-59 (2003).*, pages 41–59, Feb. 2003.